Title
TOTAL-REACTION CROSS-SECTION MEASUREMENTS FOR CHARGED PARTICLES

Author
Wilkins, Bruce D.

Publication Date
1963-05-09

UCRL-10783

University of California

Ernest O. Lawrence Radiation Laboratory

TOTAL-REACTION CROSS-SECTION MEASUREMENTS FOR CHARGED PARTICLES

Berkeley, California

DISCLAIMER

Research and Development

UCRL-10783
UC-34 Physics
TID-4500 (19th Ed.)

UNIVERSITY OF CALIFORNIA

Lawrence Radiation Laboratory
Berkeley, California

Contract No. W.7405-eng-48

TOTAL-REACTION CROSS-SECTION MEASUREMENTS FOR CHARGED PARTICLES

Bruce D. Wilkins

(Ph.D. Thesis)

May 9, 1963

Printed in USA. Price $2.75. Available from the
Office of Technical Services
U. S. Department of Commerce
Washington 25, D.C.

Contents

TOTAL-REACTION CROSS-SECTION MEASUREMENTS FOR CHARGED PARTICLES

Bruce D. Wilkins

Lawrence Radiation Laboratory and Department of Chemistry
University of California
Berkeley, California

May 9, 1963

ABSTRACT

Total reaction cross sections have been measured for 10-MeV protons, 22.4-MeV deuterons, and 40-MeV alpha particles on Be, C, Al, Ti, V, Fe, Ni, Cu, Zn, Zr, Nb, Mo, Rh, Ag, Sn, Ta, Au, Pb, Bi, and Th. A beam attentuation method that utilized millimicrosecond electronic techniques was used; these techniques made possible 3% counting statistics to be obtained in 20 minutes. The total reaction cross section σ_R shows structure as a function of A in the vicinity of Ni for proton and alpha-particle bombardments.

The results of an optical-model analysis for 10-MeV protons on Cu, Ni, Al, and Ag indicate that good fits to σ_R and the elastic-scattering angular distributions could only be obtained by using a Gaussian form factor, located on the nuclear surface, for the imaginary optical potential. Furthermore, an optical-model analysis of 48-MeV alpha particles on C^{12} indicates that the addition of total reaction cross-section data places a powerful constraint on the shape of the imaginary potential at the extreme surface of the nucleus.

The experimental techniques used in these measurements are discussed in detail. Improvements in technique for future measurement of σ_R are suggested.

I. INTRODUCTION

The measurement of charged-particle total reaction cross sections in the energy region where Coulomb barrier effects are appreciable and also the refinement of beam-attenuation techniques necessary for this energy region are discussed in this work.

By total reaction cross section, σ_R, one means the cross section for all interactions between the target nucleus and the incident beam of particles that leave the nucleus in a state different from the original ground state. This includes all direct-interaction events and all events that lead to the formation of the compound nucleus, including those events for which the compound nucleus de-excites back to the ground state, i.e., compound elastic scattering σ_{CE}. This quantity σ_R is to be distinguished from the total cross section σ_t, which includes not only all σ_R events but all the elastic-scattering events as well.

For the measurement of the quantity σ_R to be meaningful in terms of nuclear structure, it is necessary that a model of the nucleus exist that predicts this quantity and correlates it with other experimentally measurable quantities such that some insight into nuclear structure can be gleaned. The optical model fulfills this requirement.

One of the most interesting problems related to the optical model involves the mechanism of absorption. Does the absorption occur on the surface of the nucleus or throughout the nucleus? The optical model gives one a way to distinguish between these two possible modes of absorption. This model predicts the differential elastic scattering, the total reaction cross section σ_R, and the polarization induced by the scattering process. In the case of protons many excellent elastic-scattering data are available. These experimental results have been fitted equally well by using either volume absorption (Woods-Saxon shape)[12] or surface absorption (Gaussian shape) for the imaginary part of the potential. The important point is that at energies near the Coulomb barrier these two different shape potentials predict different

total reaction cross sections. Thus an accurate measurement of σ_R may determine the shape of the imaginary potential. Measurement of the total reaction cross section for charged particles in this low-energy region is a difficult task, and very few results are listed in the literature.

It was the intent of this work to measure the total reaction cross sections for various charged particles on several elements with the hope that the results would help us distinguish between absorption throughout the nucleus and absorption at the surface only. Furthermore, measurement of the reaction cross section provides a constraint on the choice of the potential parameters that future optical-model analysis may yield.

A short review of the optical model is given before a detailed description of the experimental method is reviewed. Finally, a section is devoted to the presentation and discussion of the results obtained.

II. REVIEW OF OPTICAL MODEL

The optical model has recently been tremendously successful in correlating the elastic scattering and polarization features of complex nuclei. This model is a direct descendant of the nuclear shell model.[1,2] The basic premise of these two models is that a single nucleon interacts with the entire system through an average potential due to all the other nucleons in the system. The models differ in the energy region they treat. The shell model works in the region of the ground state or low-lying excited state in which the energy levels are widely spaced, whereas the optical model is concerned with the continuum region in which the energy levels are very dense and overlap. Resonance features that are difficult to treat may be neglected by averaging over many energy levels. The optical model is also characterized by a complex potential, which accounts for inelastic processes that attenuate the incident beam.

Historically, the first attempt to explain nuclear reactions was made in the 1930's with a simple potential-well model.[3] With this model one can consider nuclear interactions as a two-body problem between the incident particle and the nucleus, described in terms of a central attractive potential.

In 1935, experiments by Fermi and others showed that low-energy neutrons exhibited extremely sharp and closely spaced resonances in their interaction with complex nuclei.[4] The potential-well model was in disagreement with this new experimental evidence, and was discarded in favor of Bohr's theory of the compound nucleus.[5]

The Bohr theory was based on the strong coupling between the incident particle and the many particles of the nucleus. Bohr's model of the nucleus gave rise to the idea that the nucleus was almost opaque to the incident nucleon, and thus the mean free path for absorption in nuclear matter was very short. This model was so successful in explaining the low-energy neutron experiments and other nuclear phenomena that for many years attention was diverted from the systematic features of nuclear properties encountered throughout the table of nuclides.

It was not until 1948, when Mayer[2] and Haxel, Jensen, and Suess[6] proposed the single-particle shell model, that these systematic features, such as the magic numbers, could be explained. The nucleons were considered to travel in particle orbits having a long mean free path for a nucleon-nucleon collision within the nucleus. This model indicated that the nucleus was actually quite transparent and not opaque as the Bohr model suggested. Serber, considering high-energy nuclear collisions, also pointed out that the nucleus may be partially transparent.[7]

In 1949 Feshbach and Weisskopf extended Bohr's strong-coupling theory to predict the energy variation of neutron total cross sections.[8] They predicted that these cross sections would decrease uniformly with increasing energy to the asymptotic value of $2\pi R^2$ ($R = r_o A^{1/3}$). It was not long until Barschall reported results on the scattering of fast neutrons (50 keV to 3 MeV) by nuclei.[9] His results showed that the total cross section decreased smoothly with increasing energy, but superimposed on the total neutron cross-section curves were broad maxima and minima, whose positions varied continously with atomic weight and energy. Feshback and Weisskopf could not by their approach explain the occurrence of these resonances.

The success of the independent-particle model and the inability of the Bohr theory to cope with the resonances observed in the scattering of fast neutrons led Feshbach, Porter, and Weisskopf to propose the "cloudy crystal ball" optical model as a means of explaining the neutron-scattering data.[10] This model pictured the target nucleus as being represented by a complex central potential of the form

$$V(r) = -[V_R + i W] \quad \text{for} \quad r < R ,$$

$$= 0 \qquad\qquad \text{for} \quad r > R ,$$

and

$$R = r_o A^{1/3} ,$$

where V_R is the strength of the real potential analogous to the independent-particle potential, and W is the strength of the imaginary potential, which allows for the possibility of the incident particle's being removed from the beam owing to absorption into a compound state. The quantity r_o is the radius constant and A the atomic weight of the target nucleus.

The results of using this model to explain the total neutron-scattering data are surprisingly good. The resonances are reproduced by the model and are understood in terms of size resonances of the potential well. As more experimental results became available, the optical model was used over a wide range of energy and target nuclei to correlate the neutron-scattering data in terms of optical-model parameters.

In 1954 Cohen and Neidigh reported extensive proton elastic-scattering angular distributions.[11] Their results showed maxima and minima in the angular-distribution characteristics of optical-model predictions. Woods and Saxon found that they could fit the proton elastic-scattering data of Cohen and Neidigh by adding a form factor to the central potential that introduced a diffuse nuclear surface to the optical potential and approximated the nuclear-density function.[12] The Woods-Saxon potential has the following form:

$$V(r) = -(V + iW)\left[1 + \exp\left(\frac{r-R}{a}\right)\right]^{-1} ,$$

where

V = strength of the real part of the potential,

W = strength of the imaginary part of the potential,

$R = r_o A^{1/3}$, the radius of the potential,

and

a = the surface diffuseness.

Cohen and Neidigh's work and the success of the Woods-Saxon potential generated a flurry of interest in the elastic scattering of protons. Soon, many groups had reported data in this field.[13-16] The Woods-Saxon potential was used by Glassgold et al.[17] and Melkanoff et al.[18] to analyze much of these data.

It was known that the nucleus exhibited strong spin-orbit coupling from shell-model work. Experimental verification of spin-orbit coupling in the optical-model region had to await the development of a polarized proton beam. In 1954, Oxley, Cartwright, and Rouvina at the University of Rochester obtained the first beam of high-energy polarized protons.[19] A double-scattering experiment showed that nuclei exhibited a left-right asymmetry when polarized protons were scattered. Results for many nuclei were soon available at both high and low energy.[20,21]

In terms of the optical model this effect was accounted for by adding a spin-orbit force to the optical potential of the form

$$V_{so} = (V_{sr} + i\, W_{si})\left(\frac{\hbar}{m_\pi c}\right)^2 \frac{1}{r}\frac{df(r)}{dr}\,(\vec{s}\cdot\vec{\ell}\,),$$

where V_{sr} and W_{si} are the strengths of the real and imaginary parts of the spin-orbit potential, $f(r)$ refers to the same form factor used in the central potential, and $(\hbar/m_\pi c)^2$ is a dimensional factor, so that V_{sr} and W_{si} can be expressed in MeV. The quantities $\vec{s}$ and $\vec{\ell}$ are the spin and orbital angular momenta in units of $\hbar$. The same form factor is usually used for the central and spin-orbit potentials to avoid introducing another parameter.

The optical potential was expected to be a function of the three observable quantities of the incident particle, i.e., its position, momentum, and spin. With the inclusion of the spin-orbit force there still remained a major assumption, the momentum dependence of the nuclear potential. To assume that the potential depends only upon the kinetic energy of the incident particles neglects the variation of the projectile's momentum as it passes through the nuclear surface. Velocity-dependent potentials are very difficult to treat, and it is only with the recent advent of ultrahigh-speed computers that progress is being made with nonlocal potentials.[22] Using a local or velocity-independent potential, one expected the parameters to show an energy dependence. This is indeed the case. The real part of the potential V_r joins smoothly, at zero energy, the shell-model value of Ross, Mark, and Lawson for both protons and neutrons.[23] It shows a steady decrease with increasing energy, reaching zero at a value of 300 to 400 MeV for the projectile.

W, on the other hand, seems to increase slowly with increasing energy of the projectile, leveling off in the vicinity of 200-MeV particles. The parameters V_{SR} behaves very similarly to V_R, and W_{si} is approximately zero at all energies. No systematic energy variation has been observed for the so-called "geometric parameters" r_o and a.

It was hoped, however, that at a given energy one could find a set of parameters that would give a reasonable fit for all values of A for the target nucleus. With the Woods-Saxon form factor the parameter W seemed to be smaller for larger values of A. Bjorklund and Fernbach reasoned that this indicated that the imaginary potential should be peaked on the surface of the nucleus. They carried out extensive optical-model analyses for neutron and proton scattering, using a Gaussian form factor centered on the surface for the imaginary potential.[24,25] They obtained excellent fits to the experimental results, and the value of W was no longer a function of A. This was, of course, at the expense of adding one more parameter--that is, b, the width of the gaussian.

There have been several theoretical attempts to explain why one might expect absorption to be peaked on the nuclear surface for low bombarding energies.[26,27] These efforts are usually based on the idea that at low bombarding energies the incident particle has very few low-lying channels in the interior of the nucleus open to it for absorption. The levels are already occupied, so that the exclusion principle inhibits absorption. In the surface region the levels are not all occupied, and inhibition of this sort is not so important. Absorption will also be proportional to nuclear density, which is a decreasing function in the surface region. These two effects couple together in such a way that it is not yet clear whether or not one should expect a surface peaking of the imaginary potential.

There have been many attempts at justification of the optical model in terms of basic theory.[28,29] In one approach Brueckner has attempted to proceed from knowledge of the two-body scattering amplitudes to the optical-model parameters and the structure of the nucleus as it scatters a low-energy particle.[30]

Althougb justification of the optical model remains an open question, it has been extremely successful as a phenomenological model. Besides neutron and proton scattering, it has been used successfully to fit the elastic scattering of deuterons,[31] alpha particles,[32] helium-3,[33] nitrogen-14,[34] and K-mesons[35] from complex nuclei. Lemmer and Green, using a nonlocal optical potential, were also able to extend the optical model to predict the proper ordering of all the energy levels of the nuclei, including the position of the magic numbers.[36] Optical-model wave functions, obtained in fitting elastic-scattering data, have been used for a distorted-wave Born-approximation calculation of the direct-interaction stripping reactions.[37] There has been considerable improvement in the fit to experimental data in this field since optical-model wave functions have replaced the plane-wave approximation.

The optical model itself has undergone many refinements since its inception a few years back. The original concept of the optical-model potential was based on the simple physical picture that each nucleus could be regarded as a piece of nuclear matter of a given shape and spatial extent. This simple concept loses much of its meaning if one tries to describe the optical potential more exactly in terms of a velocity-dependent nonlocal potential. Much of the current interest in the optical model lies in trying to find an equivalence between the nonlocal potential and the local optical potential. This model should produce many interesting results over the next few years.

III. EXPERIMENTAL METHOD

A. General

Total reaction cross sections σ_R can be measured by two principal methods. Historically, the first method used for the measurement of reaction cross sections on charged projectiles was based on summing the partial reaction cross sections determined from the chemical separation of the radioactive products. This method is practicable only at low bombarding energies for which the total number of partial reaction is low. Also the range of isotopes on which this method can be used is severely limited because many of the reaction products are stable nuclei.

Beam-attenuation techniques, long in use in work on neutron total cross sections,[38,39] have recently been adapted for the measurement of proton totoal reaction cross sections.[40,41] An attenuation experiment for charged particles is complicated by the energy loss due to ionization of the beam particle passing through the target. Thus the target thickness is restricted by whatever energy resolution is desired. The quantity σ_R can be obtained from the relationship

$$\frac{I}{I_o} = \exp(-nx\sigma_R) \qquad (1)$$

where

I_o is the incident beam intensity,

I is the attenuated beam intensity,

n the target density,

and

x the target thickness.

For an energy resolution of 10% for low-energy charged particles, the attenuation factor $nx\sigma$ is the vicinity of 10^{-3}, whereas in a typical neutron experiment it has a value near unity. It is therefore very difficult to obtain good statistics in the charged-particle attenuation experiments. When the quantity $nx\sigma$ is very small, we have

$$e^{-nx\sigma} \approx 1-nx\sigma$$

Substituting $1-nx\sigma$ into Eq. (1) and rearranging gives

$$\frac{I_o - I}{I_o} = nx\sigma. \qquad (2)$$

It should be noted at this point that σ_R in this experiment is only related to σ in Eq. (2). The exact relationship is shown later.

If one were to measure I_o and I separately for charged particles, as is done in the neutron experiments, the statistical problem of subtracting two nearly equal numbers would arise [See Eq. (2)]. Greenlees and Jarvis,[42] using this technique, have made a measurement of 9.3-MeV protons on Cu. Their method consisted of rotating an Au sample and a Cu sample of the same stopping power into a beam alternately, and measuring the variation of count rate in a stopping counter. The power of this method rests on the rapid alternation of the measurement of I_o (Au target in) and I (Cu target in), which thus averages out variations in beam intensity. The Au attenuation at 9.3 MeV is small, so that only a small correction need be made. Of course, in addition, a correction for elastic scattering of protons out of the stopping counter must be made for Au. However, since this is almost pure Coulomb scattering, the correction factor, although larger than that due to attenuation in the Cu target, is well known. To reduce their error to about 8%, 100 hours of machine time was required.

A more powerful method, however, can be used. If one were to measure directly the quantity $I_o - I$ [see Eq. (2)], then the statistical problem of subtracting two nearly equal numbers is overcome. This can be accomplished in the following manner. A thin passing counter is placed in front of the target, and a stopping counter is placed behind the target. The passing counter gives a measurement of I_o, for the unattenuated beam. Putting the stopping counter in anticoincidence with the passing counter, one obtains a direct measurement of the particles

removed from the beam by determining $I_o - I$. It is then necessary only to make a target-in— target-out measurement to obtain the reaction cross section. This is the method used here, and it is discussed in detail.

An experiment with 9-MeV protons was carried out at the University of Minnesota,[43] by a similar method but with slow electronics; consequently, a week of running time on a low-duty-cycle machine was required to reduce the error to 8%.

B. Experimental Parameters

The experiments performed here with the 60-inch cyclotron beam and using fast electronics require about 20 minutes to obtain the raw data for a measurement with 2 to 3% statistical accuracy.

The experimental parameters discussed are those for the proton-attenuation experiment. The necessary changes needed for other charged particles are mentioned later.

The 60-inch cyclotron produced a well-focused external beam of 24-MeV H_2^+ ions outside the cyclotron shielding. There were several difficulties that had to be overcome before the experiment could be started. Even with "fast electronics" the beam intensity needed in this experiment was very small, on the order of 10^5 protons/sec. When the cyclotron was run at this level, the beam was very unsteady because the ion source was unstable at such a low power level. If the beam increased suddenly by several orders of magnitude, the plastic scintillator counters could be damaged.

Another problem encountered at low beam levels was the bunching of the beam. This was due to a 360-cycle ripple in the radio-frequency power supply. This had the effect of greatly increasing the instantaneous counting rate during those bunched portions of the beam. Thus, the average beam rate had to be decreased so that the instantaneous count rate for any portion of the beam would not exceed 5×10^5 particles/sec.

The data-collecting time was correspondingly increased. Since two protons traveling simultaneously through the counter system could not be tolerated, it was necessary to separate the H_2^+ beam from the cyclotron into individual protons.

All the difficulties mentioned above were overcome by use of the following technique. A beam protons was produced by the elastic scattering of a small portion of the available external beam of H_2^+. The probability of scattering both protons from the H_2^+ into the same solid angle of acceptance is negligible. The beam had to be run at high levels to produce the necessary particles in the solid angle of acceptance. Under these conditions the beam was found to be quite stable.

The experimental arrangement is shown schematically in Fig. 1. The external beam from the 60-inch cyclotron was focused by a quadrupole magnet and then steered by a bending magnet. Residual gas pressure in the equipment was found to reduce drastically the available H_2^+ beam. Collisions with gas molecules in the long flight path from the cyclotron to the experimental area (20 ft) would disrupt the molecular bond of H_2^+ and scatter the particle out of the beam. Care was taken to reduce the gas pressure. It was then found possible to focus a 1-μA beam through an 1/8-in- collimator placed after the bending magnet. The apparatus was placed on the 30° port of the bending magnet to facilitate the removal of the H^+ component from gas scattering(which had a larger energy spread). The 1/8-in- collimator was made of tantalum slightly thicker than the range of the beam particle, followed by an antiscattering baffle. Tantalum was used because of its high density. This made possible the use of a thinner collimator, which reduced the surface area available for slit scattering. The baffle, placed 1.5-in. behind the collimator, was of such a diameter that the primary beam would just miss it.

The choice of a scattering foil was critical. The foil had to be sufficiently thin so as not to degrade the beam appreciably and yet be thick enough to provide an adequate number of protons at the solid angle of acceptance. For these reasons a foil of high-Z material had to be chosen. An acceptance angle of 15° was chosen because the

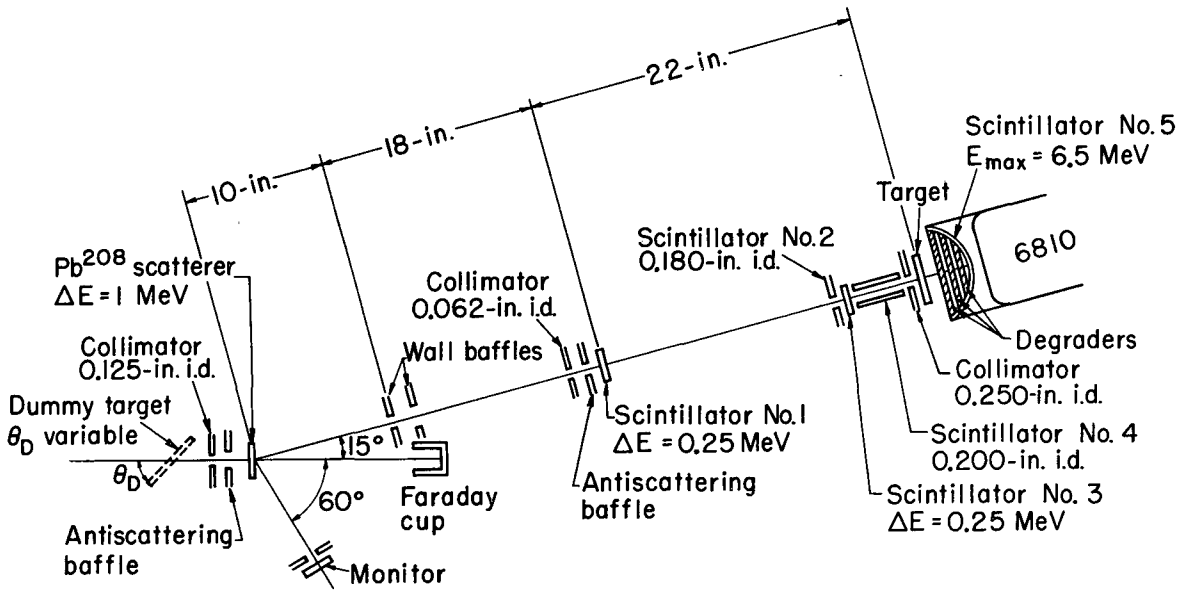

MU-27963-B

Fig. 1. Schematic diagram of the experimental area.

Rutherford scattering is large at this angle. A smaller angle could not be used because of physical space limitations in the experimental area. Not only should the cross section for elastic scattering be large at this angle, but the inelastic-scattering cross section must be very small. Inelastic events introduced low-energy components into the scattered beam that were very difficult to eliminate. The latter restriction severely limited the choice of scattering foils. A lead foil ($\Delta E \approx 0.75$ MeV for 12-MeV H^+ ions) enriched in Ph^{208} (95%) was used for most of the proton experiments. The isotope Pb^{208} was chosen because the first excited state in Pb^{208} is at an energy of 2.6 MeV, and therefore inelastic protons would be at least 2.6 MeV lower in energy than elastically scattered protons from Pb^{208}. Other lead isotopes abundant in small percentages led to (p,p') reactions that limit the energy resolution obtainable in this experiment. Th^{232} was also used. This choice was dictated by barrier considerations. A proton sees a barrier of approx 11 MeV when it encounters a Th^{232} nucleus. The reaction cross section is correspondingly low for 12-MeV protons. Even when the barrier is penetrated, it greatly hinders the reevaporation of a proton. Neutrons evaporated from the Th cause little difficulty because the counters are very sensitive to them.

Particles scattered at 15° passed through a collimating system consisting of a 0.062-in. collimator placed 10 in. from the scattering foil and followed by an antiscattering baffle. Again the collimator and baffle were just thick enough to stop the protons. The collimated beam produced by this system passes through two 3-mil plastic scintillators (counter 1 and counter 3 in Fig. 1) spaced 22 in. apart from each other.

Plastic scintillators were used throughout the experiment. Their pulses have a very fast rise time, 2 mμsec (necessary in fast coincidence work), and a short decay time, 20 mμsec, which permits a very high counting rate. Also, the handling and shaping of the various plastic scintillators is relatively easy. Unfortunately, at the low beam energies used in this experiment, the plastic scintillator gave poor energy resolution, about 10% for a stopping counter and 15% for thin passing counters. This

was due to the relatively few photons reaching the photosensitive surface of the photomultiplier. When there are few electrons produced, the statistical variation in this number begins to be important and thus leads to poor resolution.

The counter chamber consisted of a highly polished aluminum hemisphere. The plastic scintillator was placed near the center of the hemisphere in such a way that the light rays were reflected into the photomultiplier face, regardless of their initial direction. The orifices for incoming- and outgoing-beam were covered with thin reflecting foils. These foils were made of a plastic film, Zapon, which was about 20 $\mu g/cm^2$ thick. A thin coat of aluminum was evaporated on the surface of the Zapon foil to form the reflecting surface. The light-collection efficiency of the photomultiplier in this system was satisfactory. The signal-to-noise ratio for the passing counters was quite high (see Fig. 2). Counter 1 was subject to a heavy electron bombardment from the scattering foil in the absence of a magnetic clearing field. A magnet placed close to the scattering foil prevented the electrons from reaching counter 1. It was important that the electrons did not reach counter 1, for this counter determined the upper limit on the counting rate. At very high count rates in counter 1 the pulse-height response became unsteady. The response was unsteady because the later dynodes of the phototube received such a flux of electrons that excessive current was drawn from the divider string that supplied voltage to the various dynodes. This caused fluctuations in the voltage supplied to the dynodes and hence variations in the size of the output pulse.

The two passing counters 1 and 3 were placed in fast coincidence (τ = 2 mμsec) to determine the passage of a beam particle. A coincidence was used to prevent dark-current noise from a single phototube and random background in a single counter from triggering the total beam circuit. Counters 1 and 3 were placed 22 in. apart so that a time-of-flight criterion could be placed upon the particles. Inelastic events from the scattering foil and slit scattering from the collimators caused considerable concern. To eliminate these from the beam, advantage was taken of the difference between the velocities of the degraded particles and of the

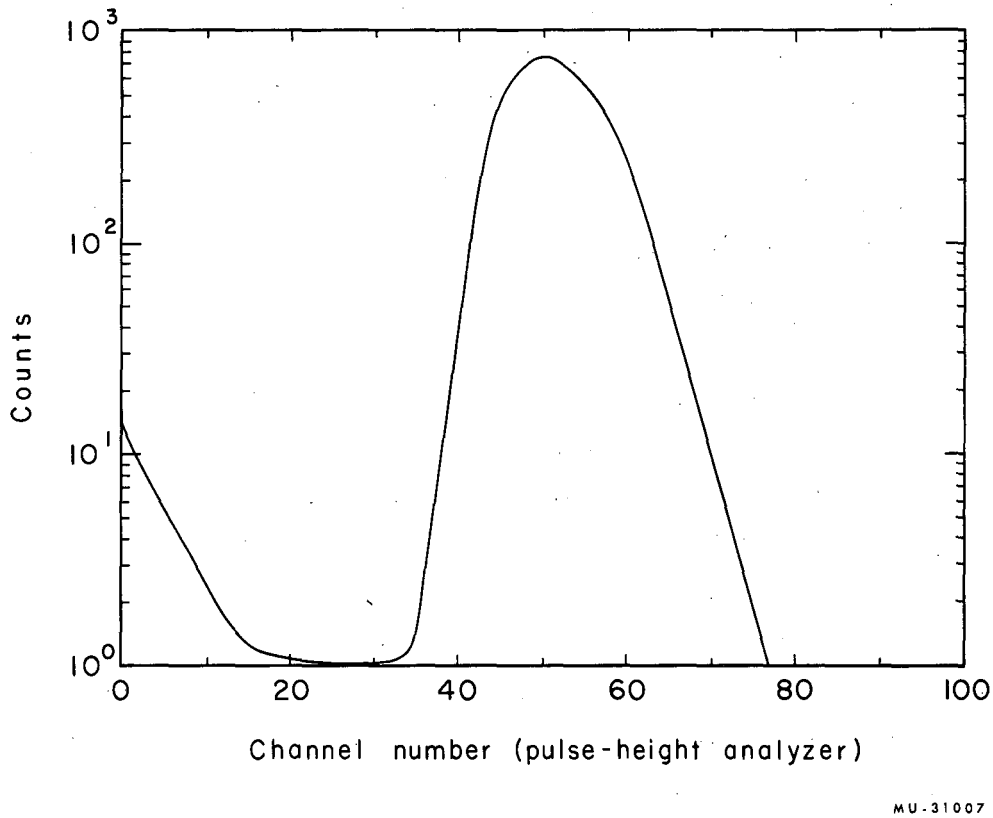

Fig. 2. Pulse-height spectrum of counter 1.

elastically scattered particles. With a resolving time of 2mμsec in the coincidence circuit and a 22-in. flight path, the 2.6-MeV excited state of Pb^{208} could be separated from the elastically scattered particles. Some inelastic events from the other Pb isotopes could not be removed because the first excited states are closer to the ground state. In addition, slit-scattered events passing through the collimating system could contribute particles that were not removed by the time-of-flight technique. It was not practicable to increase the distance between counters 1 and 3 because multiple Coulomb scattering from counter 1 removes more and more of the beam from the beam axis as the distance is increased. Even at 22 in., only 15% of the particles striking counter 1 reached counter 3. Further increase in the time-of-flight path would have reduced the number of coincidences, since the counting rate in counter 1 could not be increased, for reasons mentioned before.

For a precise experiment, a well-defined beam should impinge upon the target. Multiple Coulomb scattering from counter 1 and counter 3, however, produced a diverging beam which had to be collimated. A metal collimator between counter 1 and counter 3 was first tried but it was found to cause too much slit scattering. A satisfactory solution was the placing of plastic scintillator collimators (counters 2 and 4, see Fig. 1) in the counting system. These collimator counters were placed in anticoincidence with the passing counters. Counter 2, located just in front of counter 3, consisted of a plastic scintillator, which was thick enough to stop the beam particles and which had 0.180-in. hole in the center. Counter 4 was a 4-in.-long cylinder with a 0.25-in.-diam hole running the length of the cylinder. It extended as close to counter 3 and the target as was mechanically possible. Another very critical reason for using this counter is discussed later. A metal collimator of slightly larger inner diameter than counter 4 was placed between counter 4 and the target, to prevent backscattered particles (from the target and from the stopping counter) from entering counter 4 and cancelling out the event.

A beam particle is defined by an event of the type $1\ \bar{2}\ 3\ \bar{4}$ (where the upper bar indicates counters placed in anticoincidence) i.e., $I_o = 1\ \bar{2}\ 3\ \bar{4}$. The quantity $I_o - I$ was measured by placing a plastic-scintillator stopping counter, counter 5, after the target (see Fig. 1) in anticoincidence, i.e., $I_o - I = 1\ \bar{2}\ 3\ \bar{4}\ \bar{5}$.

As mentioned before, the maximum allowable rate for I_o was determined by the counting rate in counter 1. This rate was about 5×10^5 counts/sec and I_o was about 10% of this. However, this was very close to the maximum allowable rate from two other considerations. An I_o event occurred once in every 240 rf bursts (the 60-in- cyclotron had a frequency of 12 Mc). If an I_o event was received every 100 rf bursts with a perfectly uniform beam, then 1% of the time two protons would pass through the counters in one rf burst. Because these particles were all focused within about 2 mμ sec of one another in a given rf burst the electronics could not resolve the two particles, and a 1% error would occur. Since the beam showed some structure associated with rf voltage even under the best operating conditions, the maximum allowable rate was about the same as for the counter-1 criterion. Also, a 10-Mc fast scaler was used to record I_o. The instantaneous counting rate of I_o was of the order of 0.5 to 1×10^5 counts/sec, owing to the effective duty cycle of the cyclotron. This correspond to a 0.5 to 1% correction on I_o due to pile-up in the fast scaler. Thus one should be satisfied with an average counting rate for I_o of about 5×10^4 counts/sec. As an experimental check on the maximum allowable counting rate a graph of $I_o - I/I_o$ vs the counting rate was plotted (see Fig. 3). The point at which the $I_o - I/I_o$ curve begins to deviate from a straight line indicates when count-rate effects start to be important. In practice, the count rate was kept a little below the maximum rate to insure a safety factor.

The photomultiplier output from a monitor counter located at 60^o to the scattering foil (see Fig. 1) was displayed on an oscilloscope triggered by the 60-cycle main power, so that the cyclotron operators could view the gross beam structure introduced by the 360-cycle modulation on the rf voltage mentioned earlier. The operators could then optimize the machine parameters to obtain the best duty cycle.

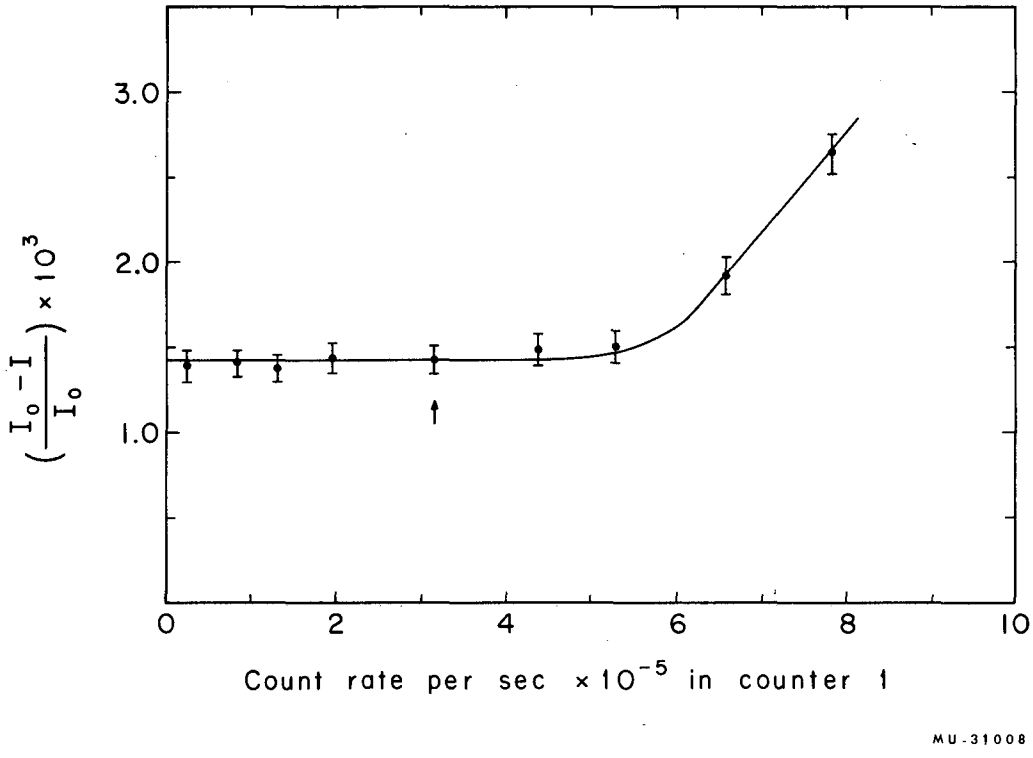

Fig. 3. Curve showing the ratio of $\frac{I_o - I}{I_o}$ vs the count rate in counter 1. The arrow indicates the average count rate at which the experiments were done.

All the counters following counter 2 were mechanically aligned with respect to counter 2. The 22-in. pipe connecting counter 1 and counter 2 was relatively flexible, so that the counter assembly could be aligned with respect to an axis drawn through the beam spot on the scattering foil and the 0.062-in. collimator preceding counter 1. This was easily done by the following method. I_o was recorded vs the integrated incident beam on the Faraday cup (see Fig. 1). If the apparatus was slightly out of line, so that a large proportion of the particles struck one of the collimator counters, then I_o was greatly reduced. This method gave a fast and accurate alignment.

At the beam levels used in this experiment, gain shifts of the order of 10% in counter 5 were expected. This, coupled with an energy resolution of about 10% in the plastic scintillator, made it essentially impossible to eliminate by pulse-height analysis inelastic events occurring in the target. A more reliable way was to place in front of counter 5 an energy-degrading foil sufficiently thick to stop protons that had been inelastically scattered in the target. Aluminum was chosen as the material for the degrader foil because it is readily attainable in thin foils. Another desirable feature of aluminum is the much lower density in atoms/cm^2 for aluminum than for a plastic scintillator of the same stopping power; it also contributed fewer reaction events than an equivalent amount of plastic scintillator. This had the effect of reducing the beam attenuation due to causes other than the target. A high-Z material such as gold, which has still fewer atoms/cm^2, cannot be used because it contributes too much back-angle elastic scattering for low-energy protons.

The energy spectrum in counter 5 had a low-energy "tail" about 2.5 MeV long, principally composed of slit-scattered particles that could not be eliminated from the beam by the time-of-flight technique. Other reactions that contributed to this low-energy tail were the (p,p') events from the minority isotopes of the Pb scattering foil, the (p,p') events occurring in both the energy degrader and the counter-5 plastic scintillator, and, of course, the (p,p') events from the target that get through the degrader. It was very important that the energy-degrader foil not be

thick enough to stop any of these slit-scattered particles that were not eliminated by the time-of-flight technique. If they stopped in the degrader foil, they appeared as reaction events in the target and masked the true events. In practice, the degrader was adjusted so that 6.5-MeV protons produced by inelastic events at the center of the target (ΔE = 1 MeV) could not reach the stopping counter. The pulse-height distribution in counter 5 was obtained to make sure that the particles in the low-energy tail were passing through the degrader, but the data were not in general usable to help with the separation of inelastic events.

C. Corrections

Low-energy protons undergo a considerable amount of large-angle elastic scattering. It was necessary that counter 5 subtend a large angle from the target; otherwise, these large-angle elastic events would miss the counter and look like a reaction event in the target. Counter 5 was designed to subtend any angle from 20° to 60°. For 10-MeV protons it was necessary to set it at 60°. In this geometry, a particle that undergoes a 60° scattering travels through appreciably more target and energy degrader. To compensate for this effect, counter 5 had a hemispherical shape with the degrader placed in such a way that large-angle scattering events passed through correspondingly less degrader (see Fig. 4).

Absorption of protons occurred more frequently in the Al degrader because it was several times as thick as the targets. This contribution had to be subtracted. The absorption in the degrader was, of course, energy-dependent. The appropriate subtraction was made by removing the target and placing a "dummy" target ahead of the scattering foil, of such thickness that the energy of the beam incident on the degrader remained the same. In this configuration the numbers $i_o = 1\ \bar{2}\ 3\ \bar{4}$ and and $i_o - i = 1\ \bar{2}\ 3\ \bar{4}\ \bar{5}$ were measured. In practice the "dummy" was an Al foil that could be placed at any angle so as to simulate all the various target thicknesses. Aluminum was chosen because it is easily

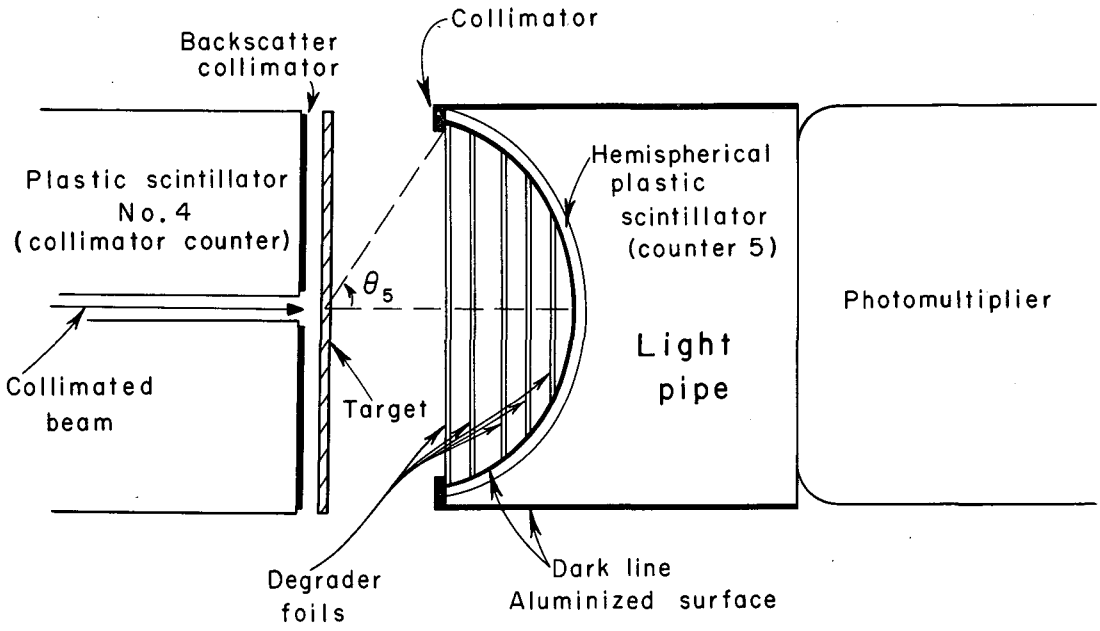

Fig. 4. Enlarged portion of Fig. 1 showing the hemispherical count 5 and the target area.

obtainable in a variety of thicknesses, and also because there are accurate range-energy tables for it.[44]

Throughtout a day's run, a graph of $(i_o - i/i_o)$ vs dummy angle was constructed (see Fig. 5). Interpolation to a given dummy angle for each target, according to its thickness, gave the appropriate target-out measurement.

The angle θ_5, the solid angle subtended by counter 5 on the target, had to be large enough to prevent the elastic scattering, whose cross section is

$$\int_{\theta_5}^{\pi} \sigma_{el}(\theta)\, d\Omega ,$$

outside the angle (θ_5 $\sigma_{el}(\theta)$ is the differential elastic-scattering cross section) from being so important that the uncertainty in this quantity limited the accuracy of the experiment. Yet, the angle θ_5 had to be as small as possible in order to reduce the inelastic contribution, whose cross section is

$$\sum_{i=0}^{N} \int_{o}^{\theta_5} \sigma_i\,(\theta)\, d\Omega ,$$

where $\sigma_i\,(\theta)$ is the differential inelastic cross section for the excitation of the ith level of the target nuclei, and where the sum extends from the ground state up to the Nth state; N is determined by the thickness of the energy-degrader foil. Here $\sigma_o\,(\theta)$ refers to the compound elastic differential cross section. Because these two corrections are opposite in sign, the angle θ_5 should be placed in such a way that the two corrections will be about equal in value. Unfortunately, the elastic-scattering correction for 10-MeV protons is much larger than the inelastic correction, especially the high-Z material, and θ_5 had to be set a large angle. In fact, it was impractical to increase this angle above 60° because at larger angles the scattered particles traveled through considerably more target and degrader foil, and it became impossible to make the appropriate corrections.

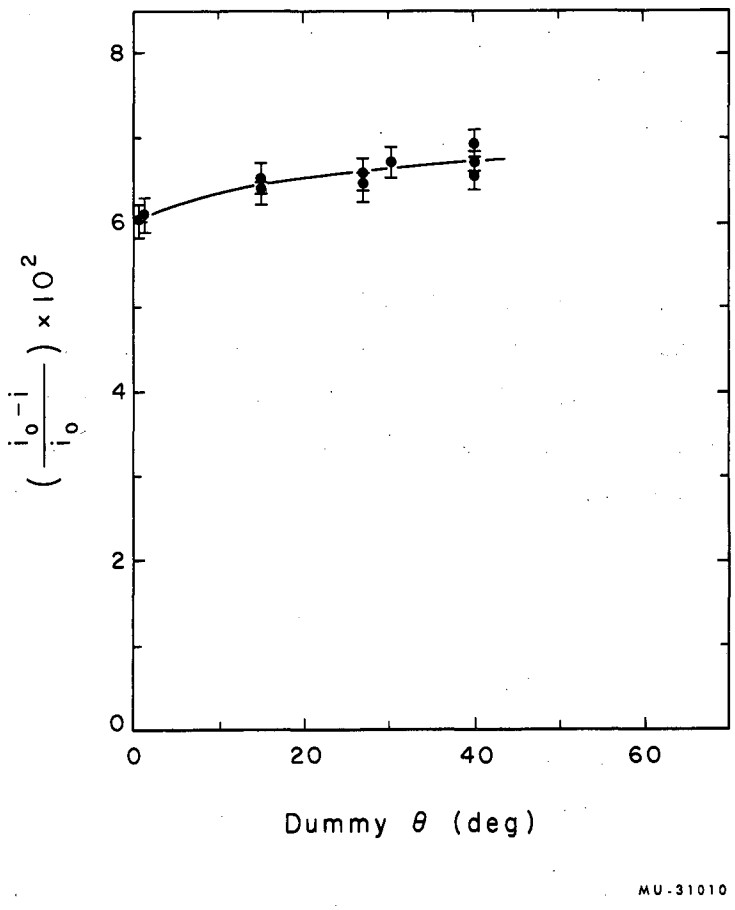

Fig. 5. A plot of $\frac{i_o - i}{i_o}$ vs the angle setting of the dummy foil.

A third principal correction was needed in the experiment. It may be remembered that a "dummy" foil was inserted ahead of the scattering foil when the target was removed. The absorptive effect of the energy degrader would then be exactly compensated for in the target-in and target-out measurements. However, this had the serious effect of changing the incident energy of the protons on counter 3 in the two configurations. In the proton experiment the energy incident on counter 3 was 11 MeV, and 10 MeV in the target-in and target-out configurations. The p + C elastic cross section[45] shows an extraordinarily large resonance in this energy region. The importance of counter 4 now becomes apparent. Counter 4, located as near as possible to counter 3 in anticoincidence, greatly reduced the scattering-out correction, since it was placed in anticoincidence with the passing counters. However, the number of protons scattered out at larger angles than θ_4, the angle subtended by counter 4 on counter 3, was still appreciable. The solid line in Fig. 6 shows the value of the quantity

$$\eta = \int_{\theta_4}^{\pi} \left[\sigma_{SE}(\theta) + \sum_{i=0}^{1} \sigma_i(\theta) \right] d\Omega \qquad (3)$$

averaged over the energy spread of the proton passing through counter 3. The quantity $\sigma_{SE}(\theta)$ is the differential cross section for shape elastic scattering, and $\sigma_i(\theta)$ refers to the differential cross section for compound elastic scattering and scattering to the first excited state. The angle θ_4 was large enough so that no correction term occurred for the elastic collision between the proton and the hydrogen in the plastic scintillator. Any proton scattered outside the critical angle θ_4 had its recoil partner hitting counter 4. If one of the protons did successfully traverse the cylindrical counter 4, then it imparted so little recoil energy to the other proton that the collision between them could be neglected.

These data were very comprehensive, so that the correction could be reliably made. As a check, however, the degrader was removed from

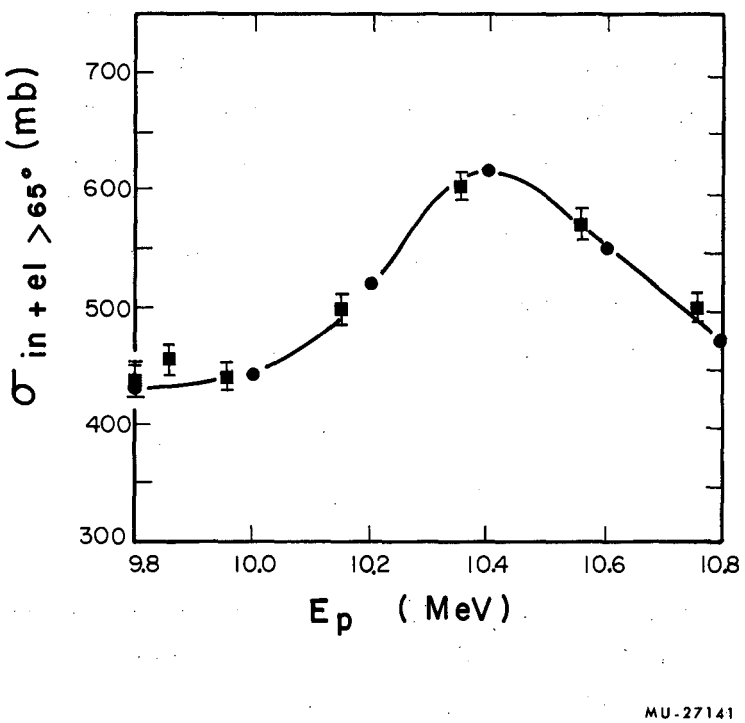

Fig. 6. Beam-energy calibration curve. The solid curve and the symbol ● represent the elastic-scattering data of Nagahara,[45] suitably integrated over the energy loss in counter 3. The symbol ⧳ represents the experimental points from this work.

counter 5 in the target-out position, and the quantity $(i_o - i)/i_o$ was measured as a function of beam energy. The beam energy was reduced by the addition of energy degraders ahead of the scattering foil. The squares in Fig. 6 show the result of this measurement. Anticoincidence events obtained in this configuration are due to nuclear reactions and elastic scattering in counter 3 scattered outside the angle θ_4. The position of the resonance in the cross section provided a quick and reliable method for measuring the beam energy. The quantity η_3, defined as $\eta_3 = \eta$ (11 MeV)$-\eta$(10 MeV) the scattering-out correction due to counter-3 events mentioned above, was obtained from data in Fig. 6 and applied to the measurement.

The experimental quantities I_o , $I_o - I$, i_o, $i_o - i$, and η_3 are related to the quantity of interest, σ_R , by

$$\frac{I_o - I}{I_o nx} - \frac{i_o - i}{i_o nx} - \eta_3 \frac{n'x'}{nx} =$$

$$\sigma_R + \int_{\theta_5}^{\pi} \sigma_{SE}(\theta)\, d\Omega - \int_0^{\theta_5} \sum_{i=o}^{N} \sigma_i(\theta)\, d\Omega , \qquad (4)$$

where n is the target density; x, the target thickness; n', the counter-3 density; and x', the counter-3 thickness. All other terms have been defined previously. One obtains from the literature the differential elastic-scattering data $\sigma_{el}(\theta)$, where

$$\sigma_{el}(\theta) = \sigma_{SE}(\theta) + \sigma_{CE}(\theta) .$$

Subtraction of $\sigma_{el}(\theta)$ gives

$$\left[\left(\frac{I_o - I}{I_o\, nx}\right) - \left(\frac{i_o - i}{i_o\, nx}\right) - \eta_3 \frac{n'x'}{nx}\right] - \int_{\theta_5}^{\pi} \left[\sigma_{SE}(\theta) + \sigma_o(\theta)\right] d\Omega =$$

$$\sigma_R - \int_0^{\pi} \sigma_o(\theta)\, d\Omega - \int_0^{\theta_5} \sum_{i=1}^{N} \sigma_i(\theta)\, d\Omega \,. \qquad (5)$$

But

$$\int_0^{\pi} \sigma_o(\theta)\, d\Omega = \sigma_{CE} \,;$$

thus, the left-hand side of Eq. (5) becomes equal to

$$\sigma_R - \sigma_{CE} - \int_0^{\theta_5} \sum_{i=1}^{N} \sigma_i(\theta)\, d\Omega \,. \qquad (6)$$

After corrections for the inelastic scattering, one is still left with σ_{CE}. It may be large compared with the value of σ_R at low energies--epecially for light targets--because there are so few channels open for de-excitation of the compound nucleus. At high energies, for which there are myriads of levels, σ_{CE} should be of negligible importance. Thus, this technique is capable of measuring only the nonelastic cross section $\sigma_R - \sigma_{CE}$, whereas the optical-model calculations give predictions of σ_R, the total reaction cross section.

IV. ELECTRONS

A. Description

Figure 7 shows a schematic diagram of the electronics. In the proton experiment the beam particle lost only 0.25 MeV in the passing counters, which produced a relatively small light output. A high-gain photomultiplier was needed to compensate for this effect. It was also especially important for counters 1 and 3 to have good time resolution so that the time-of-flight technique could be applied. With this in mind, a 14-stage RCA 7264 photomultiplier was used for counters 1 and 3. The tube has a curved photosensitive surface with a transit-time spread of only 1 mμsec. This is accomplished by reducing the spread in the length of the flight paths of the primary electrons from the photosensitive surface to the first dynode. The 14-stage RCA 6810A photomultiplier was used for the other counters. Pulse-height fluctuations occurring in the photomultipliers at high counting rates were reduced appreciably by providing voltage to the last five dynodes and the anode directly through cathode followers.

The pulses from counters 1 and 3 were amplified by Hewlett-Packard 460-A wideband amplifiers and fed into a Wenzel fast-coincidence unit.[46] It was found possible, through careful adjustment of the coincidence unit, to obtain a 2-mμsec resolving time. The following conditions were necessary for this resolution. The input pulses must have a rise time of the order of 2mμsec. The input pulses also need to be clipped to 2mμsec in length, which required short clipping lines on each pulse. Each pulse must be of sufficient amplitude so that the output pulse is not a function of the input-pulse size (see Fig. 8). If this condition is not fulfilled the output pulse-height spread due to a Δt between the pulses of different times of flight is masked. In practice a 3.5-V pulse was adequate to saturate the coincidence unit. Also the bias on a discriminator diode had to be adjusted to optimize the pulse-height ratio of the coincidence and noncoincidence pulses. To verify that a 2-mμsec resolution was obtained, delay curves were taken (see Fig. 9). For

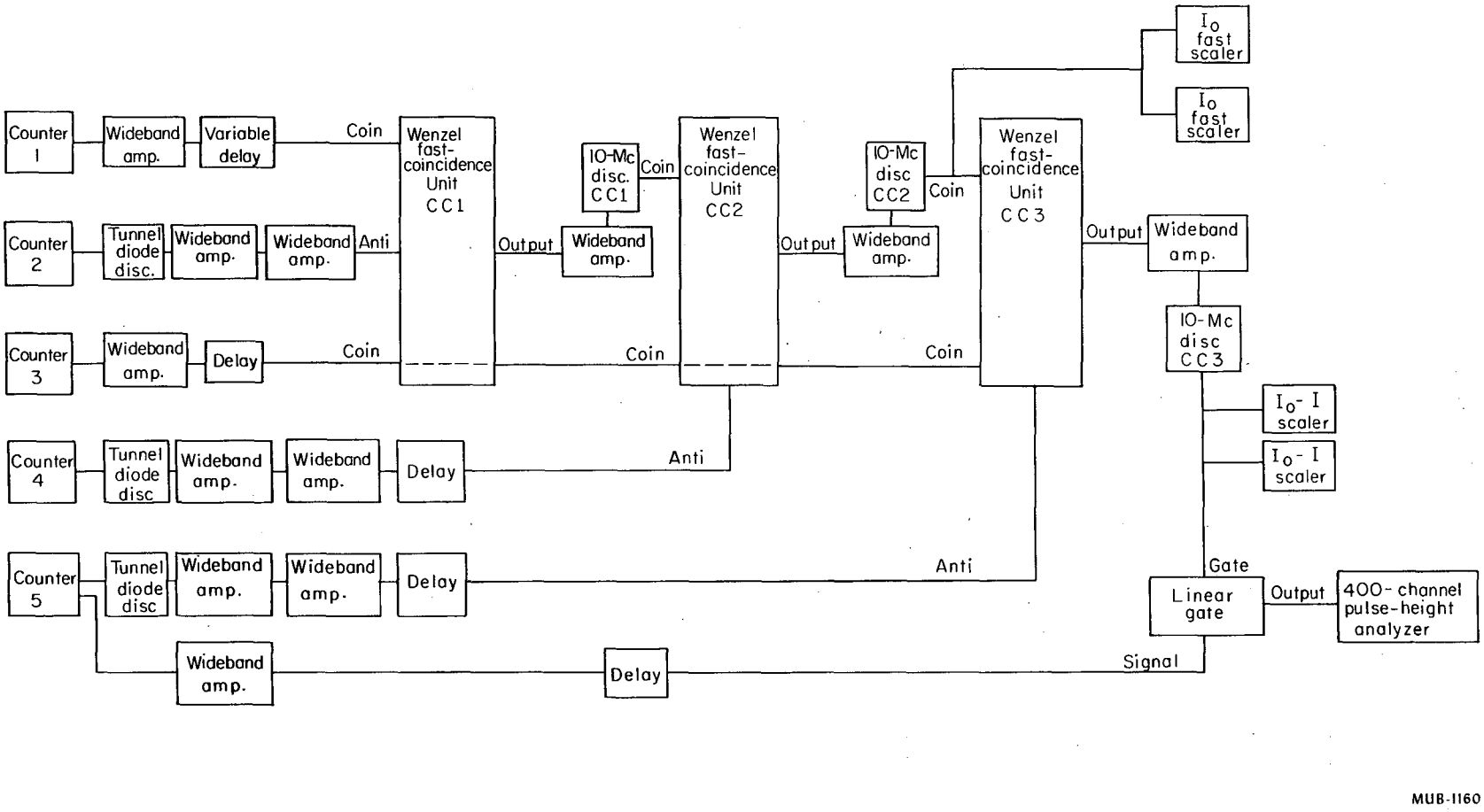

Fig. 7. Block diagram of the electronics.

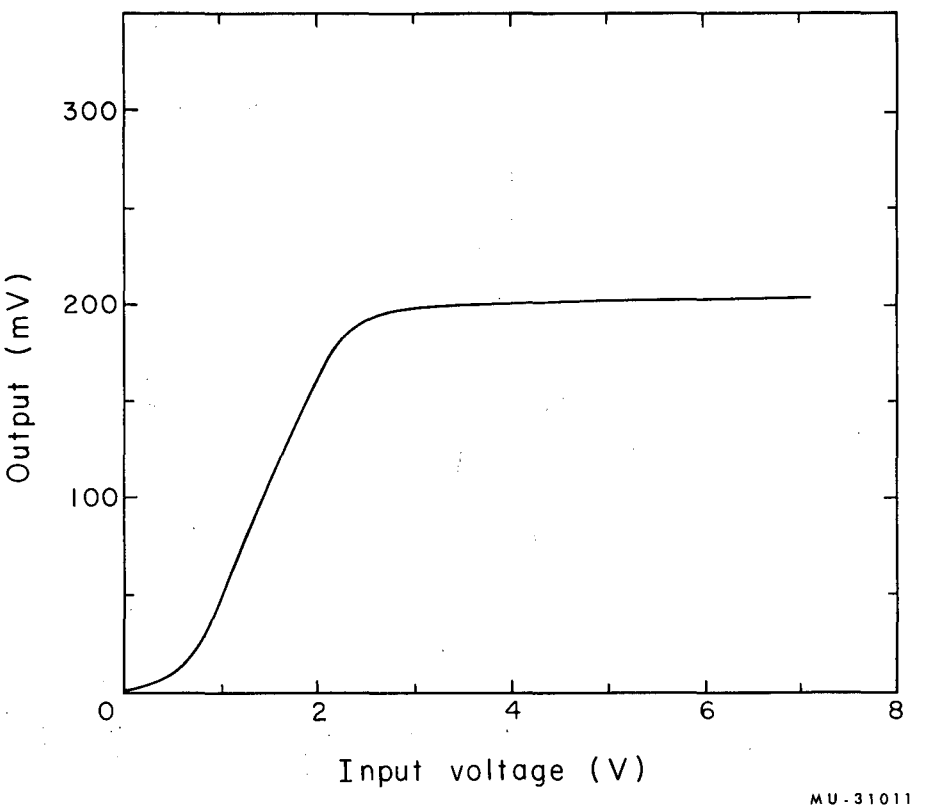

Fig. 8. Curve showing variation in the output pulse height of the Wenzel coincidence circuit vs the pulse height of coincidence input signals.

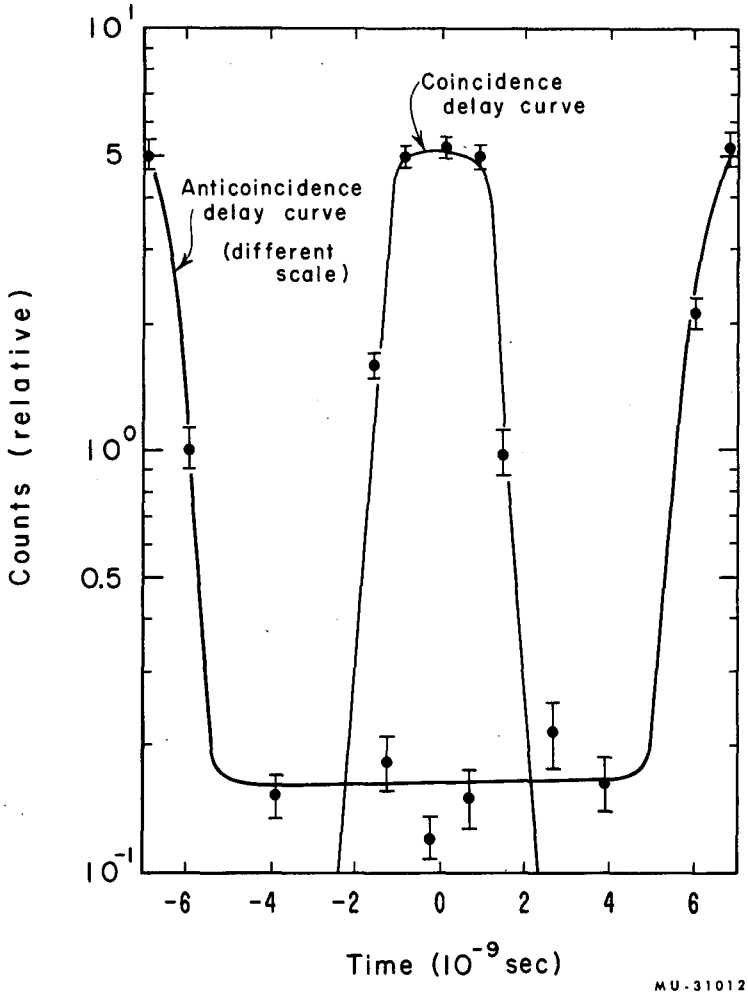

Fig. 9. Typical delay curves obtained from the Wenzel coincidence circuit by using 10-in. clip lines.

anticoincidence the Wenzel unit was found to work best with large constant-size pulses (6 V). To accomplish this, a tunnel-diode discriminator[47] producing a constant output pulse was used on all anticoincidence pulses. The tunnel-diode discriminator unit differentiated the photomultiplier pulse and fired on the zero crossover. This elminiated to a large extent the characteristic time jitter of the usual fast amplitude discriminator and preserved adequate time resolution (see curve, Fig. 9). The pulse from the tunnel-diode discriminator was amplified to the appropriate size by a cascade of wideband amplifiers and fed into the coincidence units. Three Wenzel units called CC1, CC2, and CCs (see Fig. 7) were needed to accommodate the"anticoincidence pulses". The output of CC1 was amplifed and fed into a 10-Mc amplitude discriminator (CC1 discriminator).[48] The purpose of this discriminator was to eliminate the smaller output pulses due to the time-of-flight criterion and other small output pulses from random singles events. The CC1 discriminator output was fed into the CC2 coincidence unit. Normally one would expect this procedure to cause difficulty because of the inherent time jitter in the CC1 discriminator. However, in this case very fast resolution was not needed in the CC2 unit because it was automatically carried in the CC1 pulse used as an input to CC2. By the proper adjustment of the clipping lines, the resoltuion of CC2 was set at 10 μsec. At this resolution the time jitter from CC1 discriminator became unimportant. The CC3 unit was set up in a similar way to CC2 with a 10-μsec time resolution and driven by the output of CC2. Counter 3 was carried through in the coincidence mode for all three units to eliminate the possibility that random electronic noise in a single channel would trigger the circuit. The anticoincidence pulses for CC1, CC2, and CC3 were from counter 2, counter 4, and counter 5, respectively. The scaling of CC2 output gave $1\ \bar{2}\ 3\ \bar{4} = I_o$. The output of the CC2 discriminator drove two Hewlett-Packard 520 fast scalers simultaneously, the average of which gave I_o. Agreement between these two scalers was always on the order of 0.5%. Two simultaneous scalers were also used to scale CC3, which records $1\ \bar{2}\ 3\ \bar{4}\ \bar{5}$. It is important to note that at very high count rates CC1 and CC2 discriminators may not have recovered from

their previous firings. With this electronic system, no I_o event would be recorded if either CC1 or CC2 discriminators failed to fire. Under these circumstances it was impossible to get an $I_o - I$ event.

To measure the counter-5 pulse-height spectrum, it was necessary to look at the fast pulses from the photomultipler. The counting rate was entirely too high to use the slow microsecond pulses normally employed in pulse-height analysis, and special techniques were needed to analyze the fast pulses. The output of CC3 was used as a gate pulse for a fast linear gate.[49] The gate pulse activated an integrating circuit that gave an output pulse proportional to the area of the signal to be analyzed. The gate pulse alone gave an output pulse indicated by Fig. 10. The area between 1 and 2 (see Fig. 10) was normally zero. Counter-5 signal was fed into the linear gate with an appropriate time delay so that it was centered between 1 and 2 on Fig. 10. It was also necessary to know the number of events for which there was no counter-5 signal in coincidence with the $I_o - I$ gate pulse. This number was easily obtained by adjusting the capacitance feed-through of the system; this caused a change in the height of the pedestal (see Fig. 10) so that the area between 1 and 2 was no longer zero when the gate pulse triggered the circuit. This nonzero area was integrated into an output pulse that gave rise to a peak called the "miss peak." The counter-5 signal was also incremented by the small pedestal area, but this caused no trouble so long as the signal area was large compared with the pedestal area. The signal from the integrating circuit was further amplified, stretched, and fed into a 400-channel pulse-height analyzer.

The counter-5 tunnel-diode discriminator was adjusted so that any pulse height below the full-energy peak height gave rise to a CC3 output pulse. A sample spectrum is shown in Fig. 11. The miss peak contains the (p,n) events, (p,p) events scattered outside of counter 5, and (p,p') events for which the inelastic proton failed to traverse the degrader. There are also some events in the miss peak from reactions in the degrader and scattering-out from counter 3. These were either corrected for, or averaged out in the target-out measurement. In Fig. 11, events in channels 15 through 24 are inelastic events ($6.5 \text{ MeV} < E_p < 7.4 \text{ MeV}$). The events

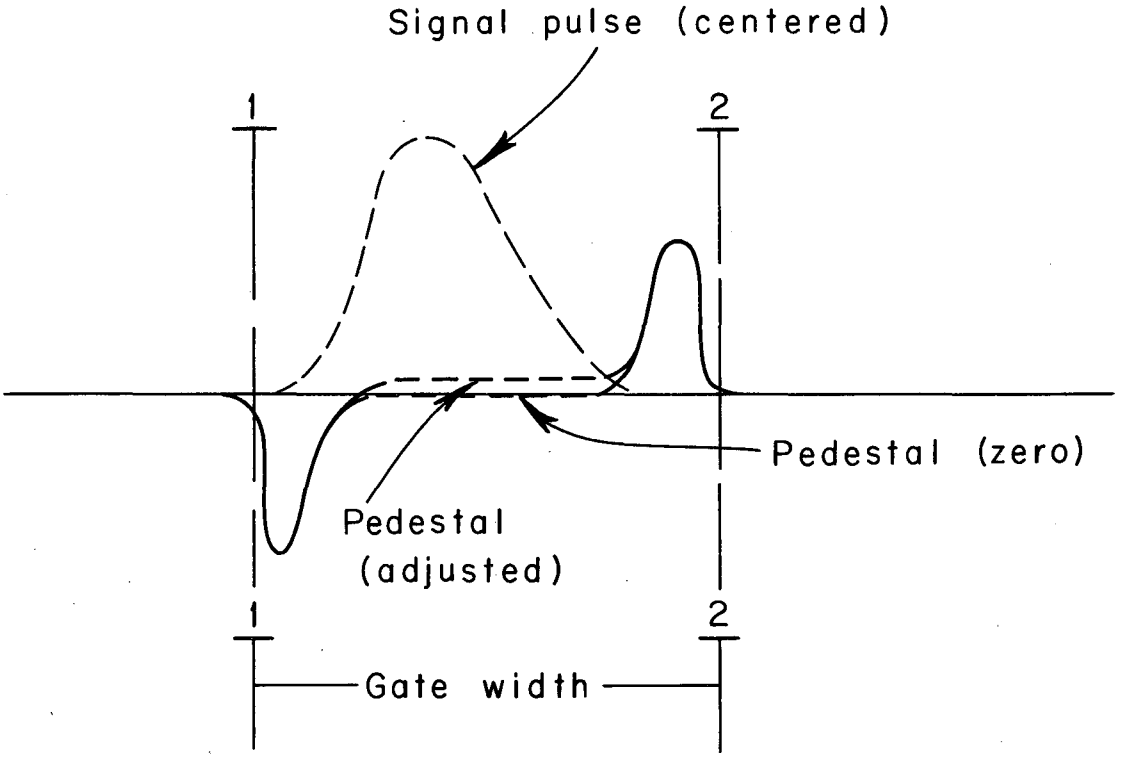

Fig. 10. Schematic of Lingo gate width (see text for explanation).

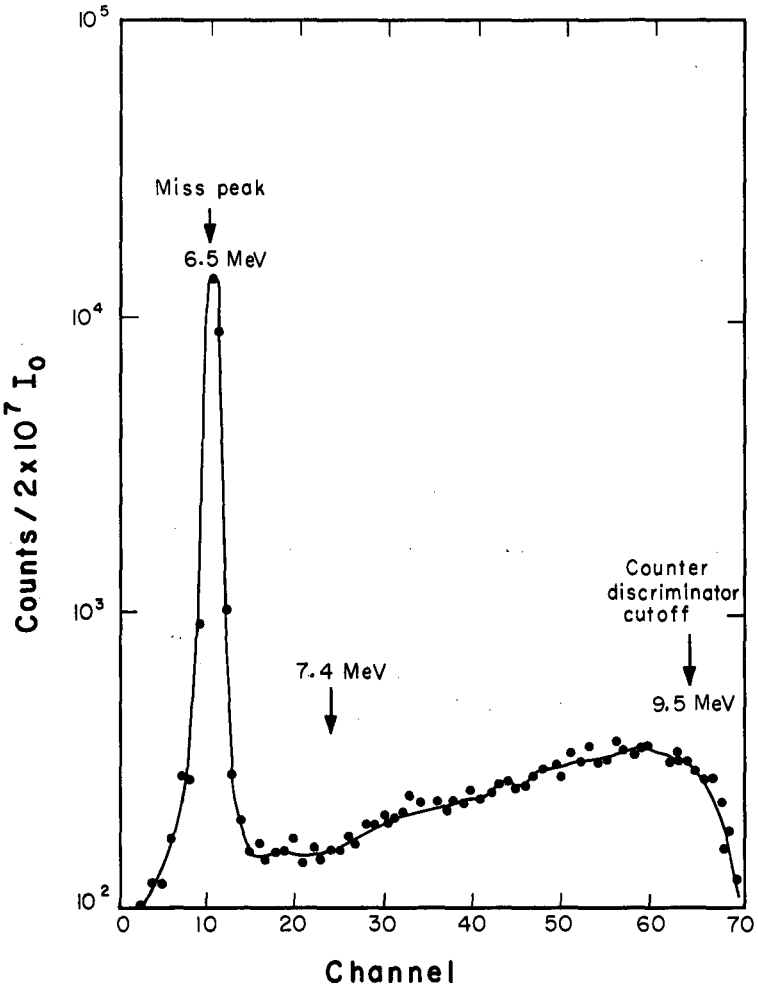

Fig. 11. Counter-5 pulse-height spectrum.

above channel 24 include inelastic events (for which the outgoing proton energy is greater than or equal to 7.4 MeV) and the low-energy tail of the incident beam. In this energy region no separation could be made between these two because the time-of-flight system could sort out only protons with energy less than or equal to 7.4 MeV (see discussion of time-of-flight method). The cutoff at about channel 64 (9.5 MeV) is at the lower side of the full-energy peak.

B. Test Procedure

An experimental procedure for setting up the electronics was followed before each day's run that minimized the check-out time and gave the most consistent results. First, the pulse heights and delays from the counters into the three coincidence units were all checked and set at optimum values. The thresholds on the three tunnel-diode discriminators from counters 2, 4, and 5 were set as low as possible. Anti-coincidence-discriminator curves were then taken (see Fig. 12) by recording the number of counts in the miss peak as a function of the CC1, CC2, and CC3 10-Mc discriminator settings. It was easy to obtain flat coincidence-discriminator curves, but very careful adjustment of the experimental parameters was necessary to obtain anticoincidence-discriminator plateaus. These curves were the best indication that the electronics was functioning properly, because a very small percentage of spurious events would affect a curve of $(I_o - I)/I_o$, since this ratio was of the order of 10^{-3}. The fast linear gate was used to check the efficiency of the anticoincidence circuits by feeding in linear pulses from the collimator counters. If the anticoincidence circuit was working properly, no pulses other than the "miss peak" would appear in the linear gate output. Adjustments were made until this requirement was fulfilled.

Another essential test concerned the time-of-flight separation. With the CC discriminators set at the values obtained from the discriminator curves, the number of counts in the miss peak for a fixed value of I_o

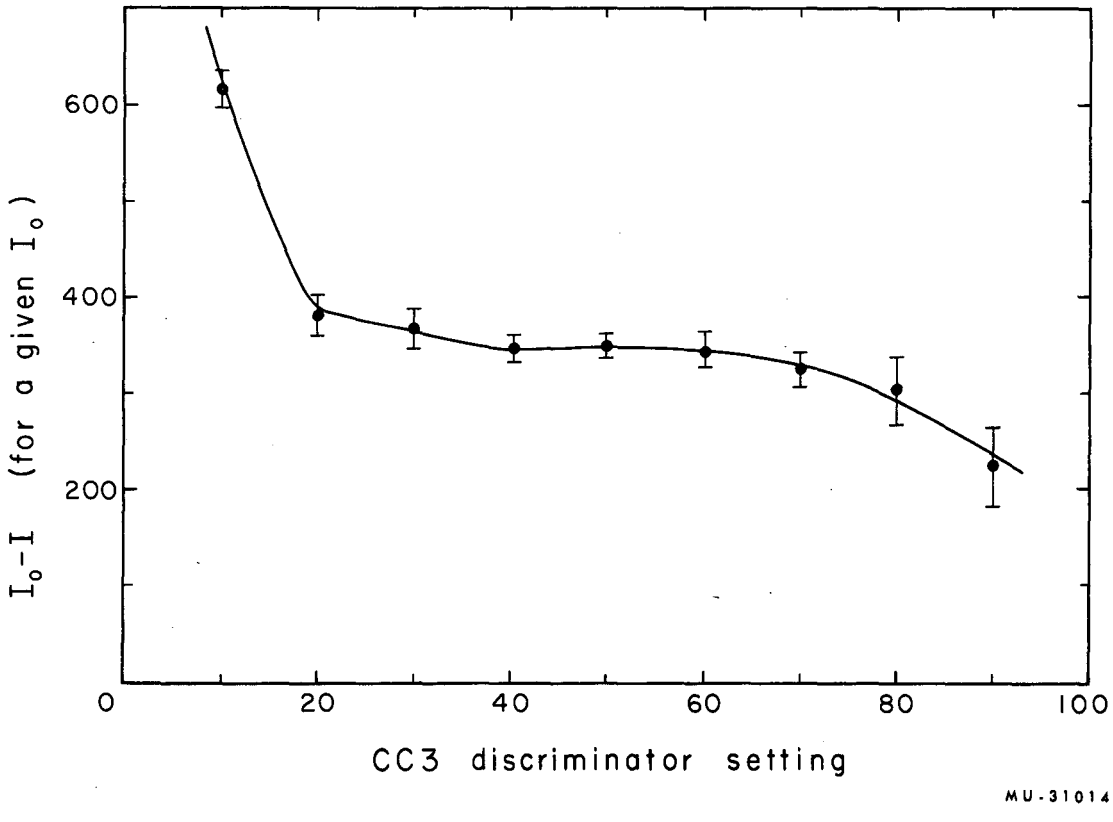

Fig. 12. The antidiscriminator curve showing the plateau obtained when the electronics are properly adjusted.

was measured as a function of the counter-1 delay time (see Fig. 13). The minimum occurred at a relative delay of approximately 1.8 μsec. If the delay was decreased, a rise in the number of counts in the miss peak for $I_o = 2 \times 10^6$ was observed. This effect was caused by two kinds of events. First, protons of energy less than or equal to 6.5 MeV yielded larger pulses in the passing counters than the full-energy particles, and thus gave rise to larger clipped pulses in the coincidence circuit (see Fig. 14, pulse B). These large clipped pulses had a wider delay-time spread (see Fig. 15, pulse B). At a shorter delay they became relatively more effective at firing the I_o circuit. Every low-energy pulse that fired the I_o circuit fell in the miss peak and caused the rise seen in Fig. 13. Secondly, elastic and inelastic events that occurred in counter 3 could contribute. Such an event would again give rise to a larger clipped pulse; only, now, it would arrive at counter 3 at the same time as the normal pulse. This had the effect of putting pulse B (Fig. 15) at the same delay as pulse A. Pulse B would again activate the I_o circuit more effectively than pulse A at reduced delays and increase the number of counts in the miss peak. The sharp rise in the number of counts in the miss peak for longer delays (see Fig. 13) occurred because protons in the low-energy tail are counted most efficiently at longer delay. The minimum in this curve (Fig. 13) is the point at which the coincidence time-of-flight technique is working best. The minimum in the time-of-flight curve had to be established for both target in and target out, because the velocity of the proton in traversing from counter 1 to counter 3 was not the same in both cases.

Another very simple test to verify that the coincidence units were working properly and that the CC2 and CC3 discriminator settings were adequate involves the removal of all anticoincidence pulses. The I_o-I and I_o scalers should then agree with each other. Removal of any of the coincident pulses from one of the coincidence units should render the I_o-I and I_o scalers inactive.

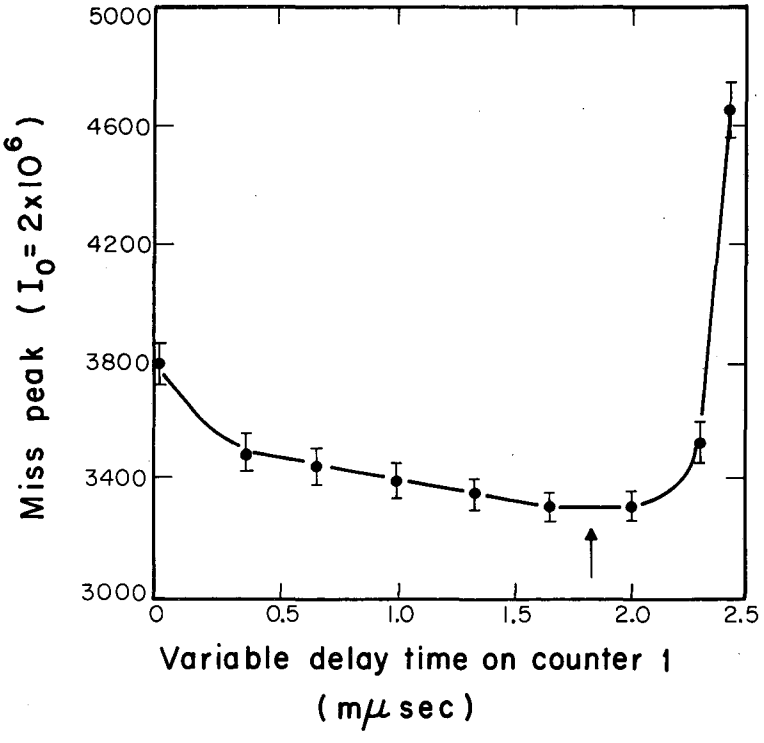

Fig. 13. The miss peak vs the variable delay on counter 1. The arrow indicates the position chosen for the runs.

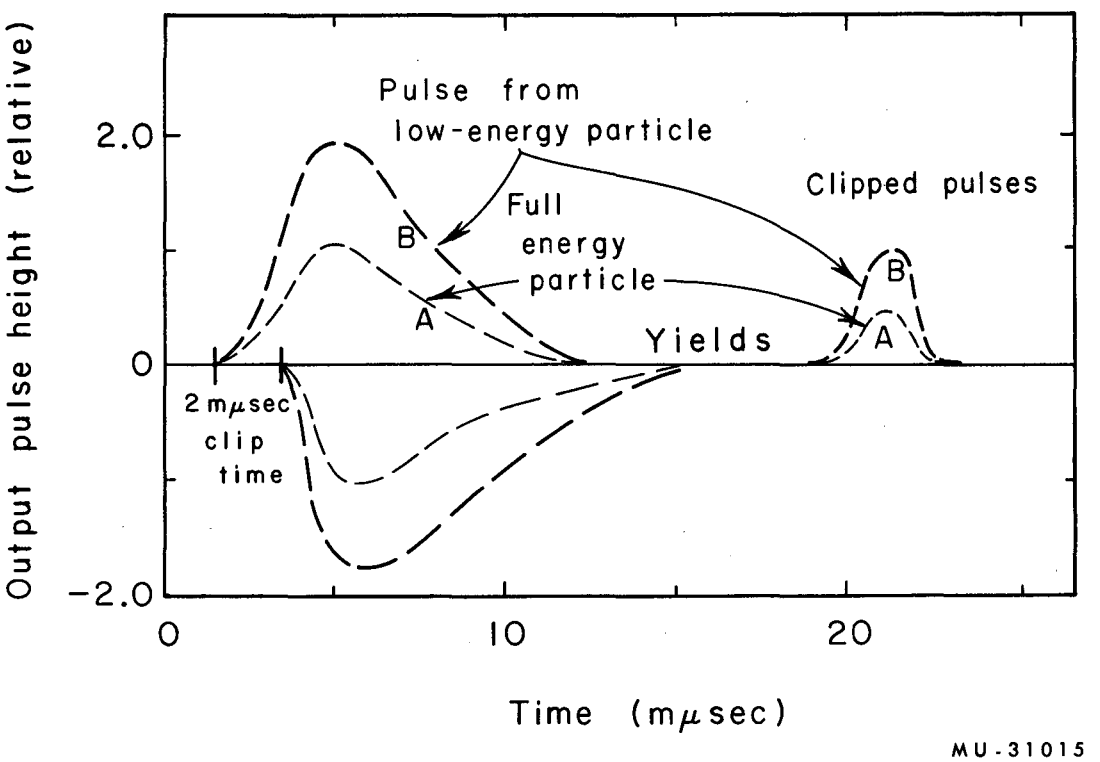

Fig. 14. Schematic showing how the clipped pulses in the Wenzel coincidence circuit can vary in size as a function of the input-pulse size. A refers to the pulse obtained in counter 3 from a full-energy particle, and B to the pulse from a lower-energy particle.

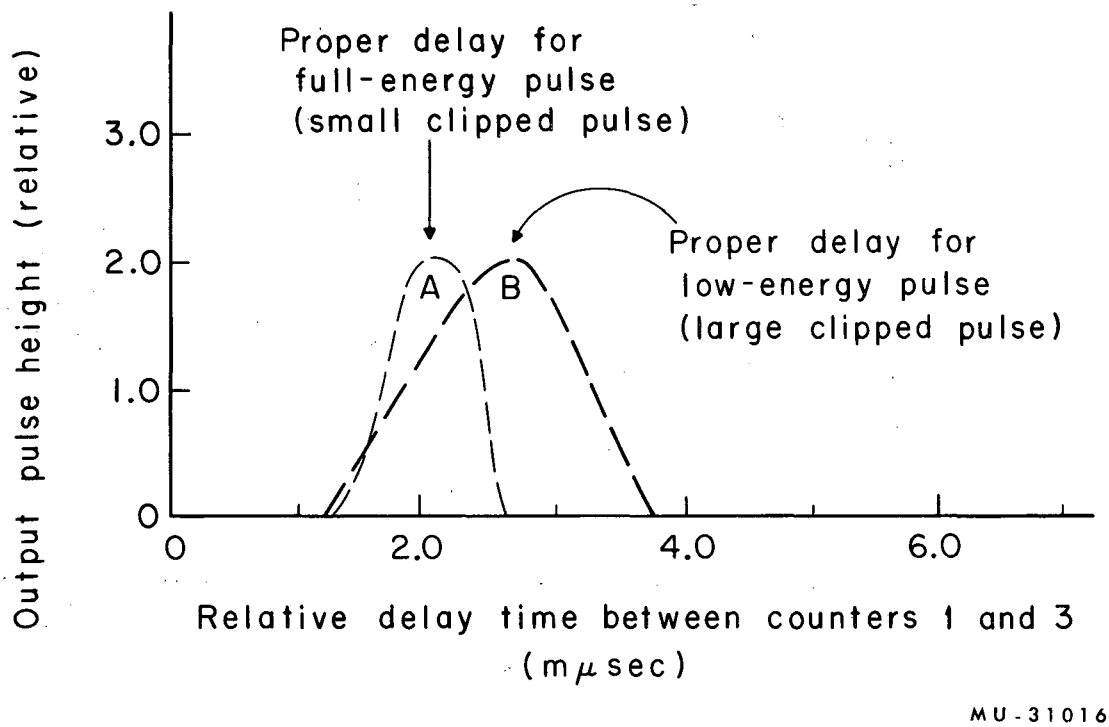

Fig. 15. Output pulse-height of the coincidence circuit vs the relative delay time between counters 1 and 3. A and B refer to the two different-sized clipped pulses shown in Fig. 14.

V. EXPERIMENTAL RESULTS

A. Protons

The raw data for the proton measurements are listed in Table I. Targets were chosen to give a systematic representation of elements throughout the periodic table. Special emphasis was placed on obtaining targets near magic numbers. The targets consist of thin foils accurately weighed on an analytical balance. A beam attenuation experiment becomes increasingly easier as the target thickness increases; however, a compromise must be made to preserve energy resolution. The target thicknesses were all chosen to represent as closely as possible a 10% energy degradation of the proton beam. Even with these "thick targets" the rejection ratio defined as $I_o/(I_o - I)$ was of the order of 1000 to 1. The energy degrader was about three times as thick as the target. Under these conditions, the target-in—target-out differences were in the ratio of four to three. In order that the uncertainties due to counting statistics be comparable to or smaller than other sources of error, it was necessary that I_o be 2×10^7 counts. At the counting rates used, a period of 10 min was required for a target-in measurement. For low-Z targets the statistical uncertainty is about 2% for the reaction cross-section measurement, whereas for higher-Z materials this quantity is nearer 4%. This is due to the smaller number of target atoms per square centimeter for the higher-Z targets.

The beam energy listed in Tables II and III is the lab energy at the center of the target. These energy values were calculated from the target and plastic scintillator-3 mass thicknesses. The energy at the center of plastic scintillator 3 was known from the position of scattering resonance (see Fig. 6). Range-energy tables allow extrapolation to the center of the target.[44]

The counter-3 correction η_3 varies in importance. For Be it may be as small as 0.2%, whereas for other targets (such as Ag the correction may run as high as 10%. Fortunately η_3 could be measured quite accurately by the method outlined earlier. The quantities I_o and i_o

Table I. The experimental quantities obtained in the measurement of $\sigma_R - \sigma_{CE}$. All column heads are defined in the text except σ, which is $\frac{I_o - I}{I_o\, nx} - \frac{i_o - i}{i_o\, nx} - \eta_3 \frac{n'x}{nx}$.

Element	Target thickness (mg/cm^2)	I_o ($\times 10^6$)	$I_o - I$	i_o ($\times 10^6$)	$i_o - i$[a]	$I_o \eta_3 n'x'$	σ
Be	23.57	20.115	34,996	20.000	14,466	+45	672
C	22.09	20.072	28,126	20.000	14,466	+40	618
Al	28.76	20.076	24,118	20.000	14,466	+40	797
Au	54.46	20.225	24,782	20.000	14,466	+40	3072
Cu	36.70	20.011	21,181	20.000	14,466	+40	1000
Zn	36.84	20.009	21,010	20.000	14,466	+40	994
Ag	43.05	20.516	21,239	20.000	14,466	+40	1312
Au	54.46	20.015	24,841	20.000	14,466	+40	3063
Ni	34.86	20.002	20,110	20.000	14,466	+40	834
Rh	40.67	20.003	20,622	20.000	14,466	+45	1303
Nb	36.96	20.000	19,933	20.000	14,466	+50	1172
Ti	27.45	21.206	21,504	20.000	14,466	+70	902
Fe	29.49	20.002	19,535	20.000	14,466	+65	853
Ta	44.52	20.108	22,021	20.000	14,466	+65	2508
Sn	37.12	20.001	20,046	20.000	14,466	+75	1522
Zr	30.09	20.401	19,509	20.000	14,466	+95	1233

[a]Average of nine runs.

Table II. The raw cross section σ, the elastic-scattering correction, inelastic-scattering correction, $\sigma_R - \sigma_{CE}$, and the energy (lab) at the center of the target. A lead scattering foil enriched to 94% Pb^{208} is used in these measurements.

Element	Energy (lab)	σ	$\int_{\theta_5}^{\pi} [\sigma_{SE}(\theta) + \sigma_o(\theta)]d\Omega$ $\theta_5 = 60.2^\circ$ (lab)	$\int_0^{\theta_5 = 60.2^\circ \text{ (lab)}} \sum_{i=1}^{N} \sigma_i(\theta)d\Omega$	$\sigma_R - \sigma_{CE}$
	(MeV)	(mb)	(mb)	(mb)	(mb)
Be	10.15 ± 0.47	672 ± 10	89 ± 5[a]	80 ± 8[g]	663 ± 14
C	10.16 ± 0.46	618 ± 13	286 ± 14[b]	0 [h]	332 ± 19
Al	10.12 ± 0.50	797 ± 24	190 ± 10[a]	97 ± 10[f]	704 ± 28
Ti	10.22 ± 0.40	902 ± 43	116 ± 9[c]	44 ± 4[f]	830 ± 44
Fe	10.20 ± 0.42	853 ± 45	148 ± 11[c,e]	54 ± 5[f]	759 ± 47
Ni	10.14 ± 0.48	834 ± 40	223 ± 11[a]	89 ± 9[f]	700 ± 42
Cu	10.12 ± 0.50	1000 ± 41	215 ± 11[a]	31 ± 3[f]	816 ± 43
Zn	10.12 ± 0.50	994 ± 41	193 ± 10[c,d]	49 ± 5[f]	850 ± 43
Zr	10.25 ± 0.37	1233 ± 72	453 ± 45[h]	20 ± 5[h]	800 ± 85
Nb	10.17 ± 0.45	1172 ± 57	483 ± 37[d]	15 ± 5[h]	703 ± 68
Rh	10.14 ± 0.48	1303 ± 57	562 ± 42[e]	10 ± 5[h]	751 ± 71
Ag	10.12 ± 0.50	1312 ± 57	630 ± 32[a]	7 ± 1[f]	689 ± 65
Sn	10.21 ± 0.41	1522 ± 72	803 ± 40[a]	4 ± 1[f]	723 ± 82
Ta	10.20 ± 0.42	2508 ±119	2179 ±164[e]	2 ± 1[h]	331 ±203
Au	10.12 ± 0.50	3068 ± 59	2895 ± 89[a]	0 ± [h]	173 ±107

[a] Reference 50.
[b] Reference 45.
[c] Reference 51.
[d] Reference 15.
[e] Reference 52.
[f] Reference 53.
[g] Reference 54.
[h] Estimates from interpolation of other data.

Table III. The raw cross section σ, the elastic-scattering correction, $\sigma_R - \sigma_{CE}$, and the energy (lab) at the center of the target. A thorium scattering foil was used in these measurements.

Element	Energy (lab)	σ	$\int_{\theta_5}^{\pi} [\sigma_{SE}(\theta) + \sigma_o(\theta)]d\Omega$ $\theta_5 = 62.1^\circ$(lab)	$\int_0^{\theta_5 = 62.1^\circ} \sum_{\ell=1}^{N} \sigma_i(\theta)d\Omega$	$\sigma_R - \sigma_{CE}$
	(MeV)	(mb)	(mb)	(mb)	(mb)
Be	9.93 ± 0.47	644 ± 10	92 ± 5[a]	80 ± 8[f,g]	632 ± 14
C	9.94 ± 0.46	504 ± 13	274 ± 14[b]	0	229 ± 19
Al	9.90 ± 0.50	744 ± 24	185 ± 10[a]	97 ± 10[f]	656 ± 28
Ti	9.99 ± 0.41	887 ± 43	114 ± 9[c]	44 ± 4[f]	817 ± 44
Fe	9.97 ± 0.42	839 ± 45	146 ± 11[c,e]	54 ± 5[f]	747 ± 47
Ni	9.92 ± 0.48	797 ± 40	220 ± 11[a]	89 ± 9[f]	666 ± 42
Cu	9.90 ± 0.50	990 ± 41	216 ± 11[a]	31 ± 3[f]	805 ± 43
Zn	9.90 ± 0.50	966 ± 41	203 ± 10[d]	49 ± 5[f]	812 ± 43
Zr	10.03 ± 0.37	1197 ± 72	424 ± 42[h]	20 ± 5[h]	793 ± 83
Nb	9.95 ± 0.45	1161 ± 57	453 ± 36[d]	15 ± 5[h]	723 ± 68
Mo	10.03 ± 0.37	1168 ± 72	467 ± 47[h]	20 ± 5[h]	721 ± 86
Rh	9.92 ± 0.48	1282 ± 57	534 ± 41[e]	10 ± 5[h]	758 ± 71
Ag	9.90 ± 0.50	1354 ± 57	603 ± 30[a]	7 ± 1[f]	718 ± 64
Sn	9.99 ± 0.41	1374 ± 72	768 ± 38[a]	4 ± 1[f]	633 ± 82
Ta	9.98 ± 0.42	2496 ±119	2110 ±160[e]	2 ± 1[h]	388 ±195
Au	9.90 ± 0.50	2952 ± 58	2790 ± 86[a]	0 [h]	162 ±104
Pb	9.92 ± 0.48	3634 ±108	3615 ±108[h]	0 [h]	49 ±153
V	9.96 ± 0.44	1082 ± 40	320 ± 48[h,i]	20 ± 3[f,i]	782 ± 62

[a] Reference 50.
[b] Reference 45.
[c] Reference 51.
[d] Reference 15.
[e] Reference 52.
[f] Reference 53.
[g] Reference 54.
[h] Estimates from interpolation of other data.
[i] $\theta_5 = 48.6^\circ$.

were obtained from the I_o scalers for the target-in and target-out cases, respectively. Events in the miss peak and up to channel 24 (see Fig. 11) gave $I_o - I$ and $i_o - i$ in the two configurations. Values of σ, the raw cross section (presented in the last column of Table I), must be corrected for elastic and inelastic scattering. These corrections are listed in Tables II and III. Table II shows the results obtained by using a Pb^{208} scattering foil, and Table III the results from the use of a Th^{232} scattering foil of slightly greater stopping power. The raw cross sections σ are listed in the second columns of Tables II and III. The third columns of these two tables contain the elastic-scattering corrections that must be substracted from σ. Reference numbers to the data used to make the corrections are given in the table. Whenever experimental data on elastic scattering were available, they were graphically integrated between the proper limits and reported in the tables. In some instances elastic-scattering data were available at nearby energies. By using the $1/E^2$ dependence of Rutherford scattering, extrapolation to the proper energy was carried out. Optical-model calculations were kindly made available by Dr. E. Schwarcz in order to check those cases for which the $1/E^2$ correction was severe.[52] Dr. Schwarcz used the results of Fernbach-Bjorklund optical-model analysis[25] for these calculations. In some cases for which elastic-scattering data were unavailable for a given target, the correction was made by interpolation from values of nearby elements. It was found by inspection of known data that the integrated correction term for elastic scattering varies quite smoothly from one element to another except in the low-Z region; therefore, use of this interpolation method whenever necessary may not be quite as uncertain as one might first guess. However, the elastic correction term in these cases limits the accuracy of the σ_R measurement. The value of σ_R listed in the tables can be corrected when a more accurate determination of some of these correction terms becomes available later.

A correction (included in column 3) due to the finite beam size has been applied to the elastic-scattering correction. This quantity, obtained by geometrical means, was found to be about +1% of the total

elastic correction. This is quite negligible compared with σ_R in all but the highest Z elements. Column 4 contains the inelastic-scattering corrections that must be added to σ, and indicates appropriate references. Again, it was sometimes necessary to make interpolations and extrapolations from existing data. Most of the data for the inelastic corrections were kindly provided by Dr. N. M. Hintz of the University of Minnesota. His angular distribution of (p,p') events for many elements showed isotropic distributions to all the levels with the exception of the first excited state, which usually had a slight forward peaking. The final result $\sigma_R - \sigma_{CE}$ is listed in the last column.

Because of the impracticality of increasing the solid angle subtended by counter 5 beyond 60°, the elastic-scattering correction for the high-Z targets Ta, Au, Pb, and Th is very large. Even though σ is measured within a statistical accuracy of 3 to 4%, the uncertainty of $\sigma_R - \sigma_{CE}$ about 40% for these targets. For this reason it is very difficult to measure $\sigma_R - \sigma_{CE}$ with any accuracy for 10-MeV protons on high-Z targets. The result for heavy elements, however, may be used as a check on the reliability of the measurements. Elastic-scattering data exist for Au, which shows very little deviation from what one would obtain from Coulomb scattering from a point charge. The sum of the elastic-scattering correction and the optical-model value for σ_R from the results of Fernbach and Bjorklund should be quite close to the correct value for this quantity σ, because deviation in σ_R from the optical-model value causes only small errors in the sum of these two quantities. The measured value of σ for Au agrees, within the statistical uncertainty of 3%, with the theoretical value.

B. Deuterons

The total reaction cross section for deuterons was measured by using the same experimental setup. Only the experimental parameters that were not the same as in the proton experiment are discussed in this

section. First, it should be pointed out that the deuteron measurements need not be done by the scattering-foil technique. The 60-in. cyclotron accelerated 24-MeV D^+ ions. Thus it was no longer necessary to separate two simultaneous particles via the scattering foil. However, the expense of redesigning the whole experiment, plus the criterion of beam stability at low power levels (mentioned earlier), led to the use of the same technique again. With 24-MeV deuterons the choice of a scattering foil was based on somewhat different criteria. The Coulomb barrier was no longer of any importance for deuterons of this energy. Consequently, σ_R will be large regardless of the element chosen for the scattering foil. Also, the time-of-flight separation could eliminate only particles of energy below 19.5 MeV. The Pb^{208} has quite a number of levels up to 4.5 MeV that could introduce inelastic components in the beam. Fortunately, however, almost the entire cross section of 24-MeV deuterons on Th^{232} is accounted for by fission. The fission fragment may strike counter 1, but it has such a short range in matter that it could not possibly reach counter 3 to give a 1, 3 coincidence and therefore could not cause contamination. A certain amount of contamination occurred from (d,d') and (d,p) events in Th^{232}.

The time-of-flight separation again determined the maximum thickness of the energy degrader, as in the proton experiment. An Al foil thick enough to stop 15-MeV deuterons and 11-MeV protons was chosen. The use of such a thick degrader prevented essentially all the evaporated particles from the target from reaching counter 5. Unfortunately, the degrader foil was many times as thick as the target. This relatively small difference between the target-in—target-out measurement made adequate statistics harder to obtain. Although no resonance similar to the proton scattering was found, a small energy dependence in the quantity η_3 (defined previously in text) for deuterons was observed and the appropriate corrections made. As no resonance occurred in the η_3 measurement, another method had to be used to measure the energy of the deuteron beam. Al degrader foils of known thickness were placed in the beam ahead of the scattering foil, and a plot of pulse height in counter 5 vs absorber

thickness was obtained. After extrapolation to zero pulse height a range-energy curve was used to determine the beam energy of the deuterons at the center of the Al target. The value obtained was 22.4 ± 0.1 MeV.

The 22.4-MeV deuterons undergo considerably less elastic scattering than the 10-MeV protons. Thus counter 5 was set to subtend a much smaller angle. Under these conditions it was no longer necessary to make the large corrections for the path length traveled in the target for large-angle scattering. The hemispherical counter 5 used for protons (see Fig. 4) was replaced with a flat-surfaced counter. The degrader was so constructed as to make small corrections for slight differences in path length through the target at the largest scattering angles. For $Z > 50$, for which scattering is more important, θ_5 was set at 43.0°, and for $Z \leq 50$, θ_5 was set at 28.7°.

Table IV lists the results for the deuteron experiment and the reference numbers to the elastic and inelastic corrections. Corrections not available in the literature were obtained from extrapolation and interpolation from nearby elements in a manner similar to that for protons. The inelastic correction is composed principally of (d,d'), (d,p), and (d,pn) events. These reactions are quite strongly peaked in the forward direction for deuterons, and could lead to quite a large correction event though θ_5 is fairly small. These corrections may have been underestimated because the angular distributions seldom were carried below 15° to 20°, which is just where $(d\sigma)/(d\Omega)$ was increasing rapidly. Also, the angular distributions were invariably done at an energy different from 22.4 MeV, and some sort of severe energy extrapolation was usually needed. The (d, t) correction was generally negligible, and the (d,α) and (d,He^3) events did not pass through the degrader foil.

C. Alpha Particles

The alpha experiment was very similar to that with the deuterons. The beam-energy method mentioned in the preceding section gave an energy

Table IV. The total beam I_o, $I_o - I$, $i_o - i$, the raw cross section σ, the counter-3 scattering-out correction η_3, the inelastic-scattering correction σ_{in}, the elastic-scattering correction σ_{el}, and the non-elastic cross section $\sigma_R - \sigma_{CE}$.

Element	I_o ($\times 10^6$)	$I_o - I$	$i_o - i$ for $1 \times 10^7 = i_o$	σ (mb)	η_3 (mb)	σ_{inel} [a] (mb)	σ_{el} [a] (mb)	$\sigma_R - \sigma_{CE}$ (mb)
Be	37.001	180,057	35,170	858 ± 10	-2 ± 4	60 ± 18	51 ± 3	865 ± 21
C	20.001	89,894	35,165	885 ± 18	-4 ± 7	65 ± 18	50 ± 8	896 ± 28
Al	22.005	92,965	35,185	1098 ± 31	+2 ± 9	75 ± 13	41 ± 2	1134 ± 35
Ti	21.002	83,465	35,125	1381 ± 57	-61 ± 20	85 ± 24	58 ± 9	1347 ± 66
V	20.002	80,141	35,150	1412 ± 56	-24 ± 19	85 ± 24	63 ± 9	1410 ± 64
Fe	21.003	83,037	35,140	1406 ± 61	-39 ± 21	90 ± 25	87 ± 14	1370 ± 70
Ni	20.004	81,072	35,190	1486 ± 55	+7 ± 17	92 ± 25	94 ± 5	1491 ± 63
Cu	20.000	81,116	35,190	1537 ± 56	+7 ± 17	99 ± 16	104 ± 5	1539 ± 61
Zn	20.000	81,247	35,190	1595 ± 58	+7 ± 17	100 ± 25	108 ± 5	1594 ± 65
Zr	20.000	76,772	35,080	1937 ± 96	-328 ± 34	94 ± 15	182 ± 27	1521 ±106
Nb	21.002	82,787	35,160	1789 ± 80	-23 ± 27	90 ± 23	190 ± 22	1666 ± 90
Rh	21.004	83,384	35,175	1899 ± 82	-4 ± 27	82 ± 21	230 ± 11	1747 ± 89
Ag	20.002	79,072	35,185	1801 ± 81	+6 ± 27	78 ± 12	250 ± 12	1635 ± 87
Sn	20.002	77,044	35,130	1863 ±101	-95 ± 36	79 ± 17	284 ± 33	1563 ±117
Ta	20.000	75,569	35,140	1843 ±128	-91 ± 46	95 ± 20	210 ± 31	1637 ±140
Au	22.001	83,946	35,185	1773 ±117	+9 ± 40	96 ± 22	246 ± 12	1632 ±126
Pb	20.003	74,970	34,560	1891 ±122	-6 ± 40	95 ± 24	266 ± 40	1714 ±136
Bi	20.000	76,490	35,180	1952 ±121	0 ± 40	93 ± 23	272 ± 41	1773 ±136
Th	20.000	74,708	35,140	1772 ±147	-97 ± 53	95 ± 24	319 ± 48	1451 ±165

[a] References for σ_{inel} and σ_{el} are 54,55,56,57,58,59,60.

of 40.0 ± 0.2 MeV for the alpha particles at the center of the Al target. A measurement of the η_3 correction was again found to have a small energy dependence. For $Z > 50$, θ_5 was set at 43.0° and $Z \leq 50$, $\theta_5 = 28.7^\circ$. The degrader foil was sufficiently thick to stop 26-MeV alpha particles from reaching counter 5. Table V lists the results and the references for the corrections. The (α,α') and (α,p) reactions are the main components of the inelastic correction. The $(\alpha.d)$ and (α,t) contributions were negligible, and the (α,He^3) generally did not pass through the degrader. Current literature supplies an ample amount of (α,α') angular distributions on which to base this correction, but a dearth of (α,p) angular distributions required the following method for this correction.

The statistical model by Dostrovsky, Fraenkel, and Friedlander[61] for particle evaporation at low energies was used. (A computer program using the Monte Carlo technique was applied.) This model is based on Weisskopf's equation[62]

$$P_j(\epsilon)d\epsilon = \gamma_j \sigma \epsilon [W(f)/W(i)]d\epsilon , \qquad (7)$$

where $P_j(\epsilon)d\epsilon$ is the probability per unit time for the emission of a particle j with a kinetic energy between ϵ and $\epsilon + d\epsilon$. The constant γ_j equals $\frac{g_j m_j}{\pi^2 \hbar^3}$; g_j and m_j are the number of spin states and the mass of particle j, respectively; σ refers to the cross section for the inverse reaction; and $W(f)$ and $W(i)$ are the level densities of the final and initial nuclei at their respective excitation energies. For the level density the equation

$$W(E) = C \exp \{2[\underline{a}(E - \delta)]^{1/2}\} \qquad (8)$$

is used; here, C and $\underline{a}$ are constants, E is the energy of excitation, and δ is a correction due to pairing and shell effects.

Table V. The total beam I_o, $I_o - I$, $i_o - i$, the raw cross section σ, the counter-3 scattering-out correction η_3, the inelastic-scattering correction σ_{inel}, the elastic-scattering correction σ_{el}, and the nonelastic cross section $\sigma_R - \sigma_{CE}$.

Element	I_o ($\times 10^6$)	$I_o - I$	$i_o - i$ for $10^7 = i_o$	σ (mb)	η_3 (mb)	σ_{inel}[a] (mb)	σ_{el}[a] (mb)	$\sigma_R - \sigma_{CE}$ (mb)
Be	36.037	92,519	13,250	789 ± 7	9 ± 4	36 ± 7	51 ± 3	783 ± 11
C	20.018	46,308	13,230	894 ± 12	12 ± 6	60 ± 9	65 ± 3	901 ± 16
Al	29.023	59,314	13,345	1105 ± 17	23 ± 10	54 ± 8	41 ± 2	1141 ± 21
Ti	30.041	52,495	12,570	1422 ± 30	32 ± 18	77 ± 12	31 ± 5	1500 ± 37
V	25.027	44,089	12,710	1397 ± 32	43 ± 18	80 ± 12	31 ± 5	1480 ± 39
Fe	26.028	44,168	12,640	1363 ± 34	36 ± 20	68 ± 12	31 ± 5	1436 ± 42
Ni	32.065	57,407	13,360	1271 ± 28	40 ± 18	79 ± 15	36 ± 2	1354 ± 37
Cu	20.020	37,363	13,360	1526 ± 36	42 ± 19	128 ± 26	50 ± 3	1646 ± 48
Zn	20.021	37,004	13,360	1511 ± 37	42 ± 19	129 ± 26	48 ± 3	1639 ± 49
Zr	34.059	57,156	13,300	1753 ± 48	45 ± 32	97 ± 23	124 ± 7	1771 ± 63
Nb	20.025	35,608	13,700	1704 ± 52	53 ± 27	105 ± 24	134 ± 7	1728 ± 64
Mo	20.027	33,431	13,300	1792 ± 65	47 ± 34	103 ± 24	160 ± 10	1782 ± 78
Ag	20.018	35,788	13,360	1881 ± 52	61 ± 27	99 ± 25	195 ± 10	1846 ± 64
Sn	20.015	33,231	13,110	1858 ± 65	59 ± 34	97 ± 25	246 ± 13	1768 ± 78
Ta	20.027	32,016	13,250	1846 ± 83	79 ± 44	97 ± 25	136 ± 7	1886 ± 97
Au	28.038	46,574	13,400	1931 ± 63	88 ± 39	100 ± 25	200 ± 10	1919 ± 79
Pb	31,013	50.855	13,370	1953 ± 62	89 ± 42	100 ± 30	250 ± 13	1892 ± 82
Bi	20.005	32.839	13,390	1923 ± 87	100 ± 46	100 ± 30	270 ± 20	1853 ±105
Th	25.007	39,509	13,250	1973 ± 84	92 ± 51	100 ± 30	404 ± 20	1761 ±105

[a] References for σ_{inel} correction are 66,67,68,69,54; see also text for statistical-model correction to σ_{inel}.

[b] References for σ_{el} correction are 54,68,70,71,72.

The model as formulated by Dostrovsky et al. has three parameters, $\underline{a}$, δ, and r_o, which are varied to fit excitation function data; (r_o occurs in the equation for the inverse cross section). They also replaced the parameter δ with Cameron's pairing δ's,[63] plus a 1-MeV shell correction at magic numbers, and repeated the calculations. The three-parameter technique gave quite reasonable results, but the pairing method was considerably poorer. Because it would be tedious to go through the elaborate fitting procedure of establishing the parameter δ for every one of the targets, it was hoped that the latter technique mentioned above could be improved. The principal difficulty in that technique was the inhibition of proton evaporation. The p/n evaporation ratio is controlled by the value of δ, whereas the shape and position of the excitation function are determined by the level-density parameter $\underline{a}$. It was felt that inadequate accounting of shell effects might have caused the trouble. Cameron has published a set of empirical shell corrections in connection with his semiempirical mass formula.[64] This set of values δ_s was introduced into the level-density equation

$$W(E) = C \exp \{2[\underline{a}\,(E - \delta_p - \delta_s)]^{1/2}\} , \qquad (9)$$

where δ_p is the pairing correction. Figures 16 and 17 show the predicted excitation functions for Ge^{68} compound nucleus with and without δ_s, respectively. The predicted σ_R has been normalized to the experimental value for α's on Zn. The improvement is quite marked. Parameter values of $r_o = 1.7 \times 10^{-13}$ cm and $\underline{a} = A/20$ were used in both figures. Porile's[65] experimental excitation functions for alphas on Zn^{64} are used for comparison. The fits throughout the periodic table with the use of Cameron's δ_s were as good as those obtained by Dostrovsky et al., who used a variable parameter δ for each proton and neutron number.

Statistical-model calculations were carried out for each target used in the experiment, and the (α,p) correction

$$\int_{\theta_5}^{0} \int_{6.5\ \mathrm{MeV}}^{E_{max}} \left(\frac{d\sigma}{d\Omega}\right)_{\alpha,xp} d\Omega dE$$

could be computed by assuming a

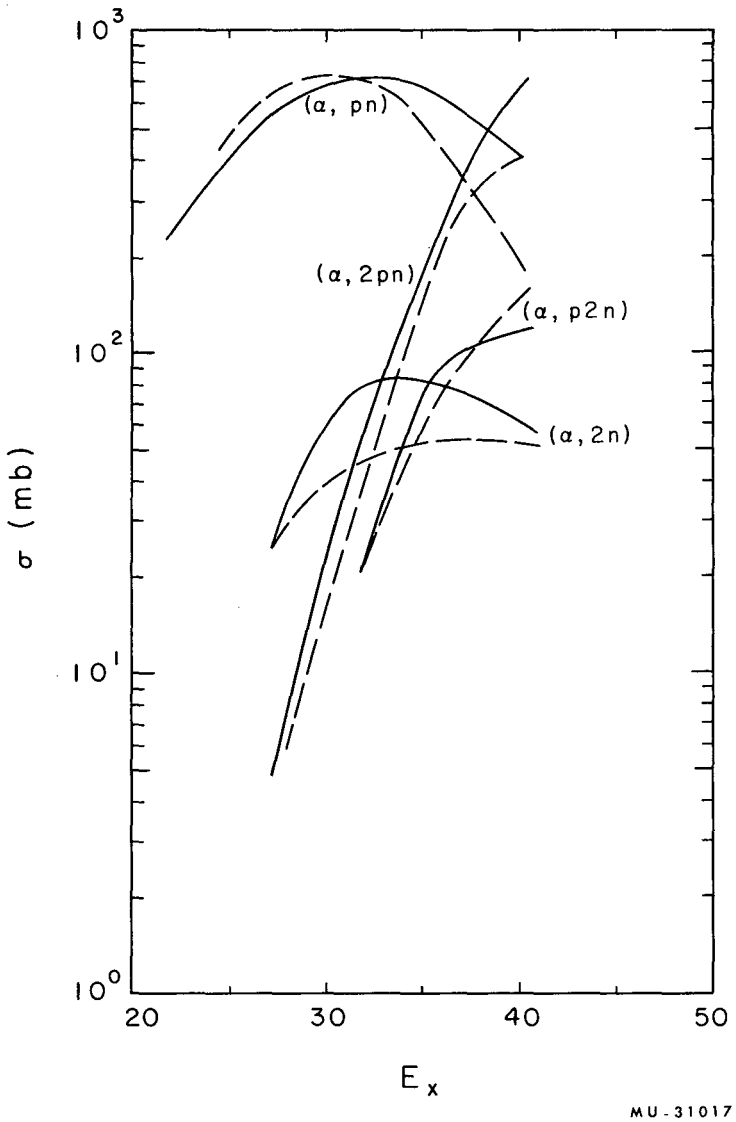

Fig. 16. The results of the statistical-model calculation with the shell correction included for alpha particles on Zn.[64] The dashed line represents the predicted values, and the solid line represents the experimental results of Porile.[65] The predicted values have been normalized to the experimental value σ_R reported in the work for 40-MeV alphas on Zn.

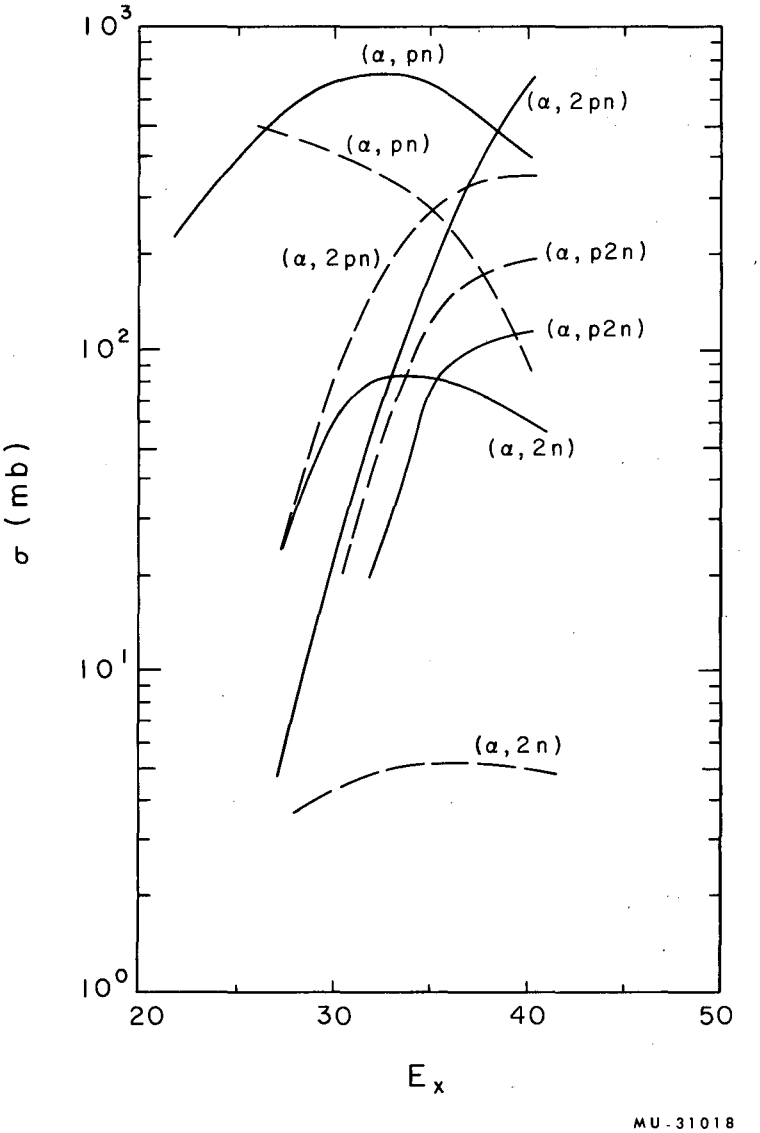

Fig. 17. The results of the statistical-model calculation with no shell correction for alpha particles on Zn.[64] The dashed line represents the predicted values, and the solid line represents the experimental results of Porile.[65] The predicted values have been normalized to the experimental value of σ_R reported in this work for 40-MeV alphas on Zn.

slight forward peaking of the predicted (α,xp) events. Direct-interaction events, not accounted for by this model, contribute to the forward peaking. If the assumed peaking of the angular distribution were underestimated because of direct interaction, the correction could be too small. The correction varies from 0 to 50 mb, depending upon the target material.

D. Errors

Principal causes of error in this beam-attenuation experiment are the uncertainties in the elastic and inelastic corrections, the statistics, and the η_3 correction. These effects have been discussed in detail earlier. The error arising from these effects is usually between 3% and 6%, depending on the target. Other sources of error, which were considered and estimated to be about 1% or less, can be neglected. These were target nonuniformities, uncertainties in the determination of target thickness, impurities in the target, dead-time corrections of the fast scalers and 10-Mc discriminators, multiple beam particles in the same rf cycle, beam bunching that caused the instantaneous counting rate to be too high, accidental coincidences caused by neutrons and gamma rays that triggered the coincidence circuit, and very-large-angle scattering from the target, which cancelled the event because of an anticoincidence in counter 4.

A major source of accidental coincidences could be due to knock-on protons from plastic scintillator 3 caused by collisions with neutrons, which would give an accidental coincidence with a beam particle that passed through counter 1 and was then scattered out of line from the other counters. A rough determination of this process was obtained by preventing all charged particles from reaching counter 3 (a thick stopping foil was placed between counters 2 and 3) and by assuming that the neutron flux in counter 3 was unchanged. The number of coincidences between counters 1 and 3 was recorded and found to be very small.

Another possible problem is the deuteron contamination of the proton beam, and conversely, the proton contamination of the deuteron beam. The cyclotron frequencies necessary for accelerating these two different ions are very close to each other. Special effort was made to stay on the far side of the resonance, away from the resonance of the unwanted ion. From observation of the stopping-counter pulse-height spectrum, this contamination was estimated to be less than 1%.

Many of these sources of error, although small in their own right, are even less important because they tend to be averaged out in the target-in—target-out measurement.

VI. DISCUSSION AND ANALYSIS

A. General

It was necessary to make an optical-model analysis in order to determine if the total reaction cross-section results were helpful in clarifying the optical-model description of the nucleus.

Before a discussion of this analysis is given, it will be useful to define several terms used in optical-model work. The total cross section is defined as the sum of the cross sections for elastic scattering, σ_{el}, and the inelastic scattering, σ_{in}. Thus,

$$\sigma_T = \sigma_{el} + \sigma_{inel} .$$

The quantity σ_{el} is the sum of all processes that lead to a reemission of the incident particle without loss of energy in the center-of-mass system. Hence, σ_{inel} refers to all those processes in which the incident particle disappears or is reemitted with a loss of energy in the same system of reference. The elastic cross section σ_{el} is composed of two parts:

$$\sigma_{el} = \sigma_{SE} + \sigma_{CE} .$$

The shape elastic scattering (SE) is due to a reflection of the incident particle by the potential that it experiences. "Compound elastic scattering" (CE) refers to a process in which the incident particle forms a compound state with the nucleus, and then at a later time deexcites and emits a like particle via the entrance channel. The total reaction cross section σ_R is defined by the equation.

$$\sigma_R = \sigma_{inel} + \sigma_{CE} .$$

With the optical model one can predict the quantities σ_{SE} and σ_R. Experimentally one cannot distinguish between σ_{SE} and σ_{CE}, and thus one measures σ_{el} and σ_{inel}. Fortunately, at excitation energies for which there are many levels open to de-excitation, the probability of de-excitation via the entrance channel becomes negligible. In this case, $\sigma_{el} \approx \sigma_{SE}$ and $\sigma_{inel} \approx \sigma_R$.

B. Optical-Model Program

I would like to thank Dr. Norman K. Glendenning for the use of his optical-model program written for the IBM 7090 computer. An accurate mathematical description and detail approach to the optical-model computer program appears in the literature.[73] It should suffice here to give a few of the principal equations, and to say that the general approach of the program involves numerical integration of radial Schroedinger equations for effective partial waves by the three-point Runge-Kutta method. The differential elastic-scattering cross section is computed from the scattering amplitude $f(\theta)$:

$$\left(\frac{d\sigma}{d\Omega}\right)_{el} = |f(\theta)|^2 \quad . \tag{10}$$

For charged particles, $f(\theta)$ is given by

$$f(\theta) = f_c(\theta) + \frac{1}{k} \sum_{\ell=0}^{\infty} e^{2i\delta_\ell} (2\ell+1)\, C_\ell P_\ell (\cos\theta), \tag{11}$$

for which the different terms are defined as follows:

the wave number

$$k = \frac{\mu}{\hbar M_{inc}} \sqrt{2\, M_{inc}\, E_{lab}} \quad ,$$

where μ is the reduced mass of the system, M_{inc} is the mass of th incident particle, the $P_\ell (\cos\theta)$ are the Legendre polynomials, and the amplitudes

$\frac{C_\ell = e^{2i\delta_\ell} - 1}{2i}$, where δ_ℓ is the nuclear phase shift. The term $f_c(\theta)$ is the Coulomb amplitude, and σ is the pure Coulomb phase shift. Thus

$$f_c(\theta) = \frac{-\eta}{2k\mathrm{Sin}^2(\theta/2)} \exp\left\{- i\eta\ell n\,[\mathrm{Sin}^2(\theta/2)] + 2i\sigma_\ell\right\}, \qquad (12)$$

$$\sigma_\ell = \arg\Gamma\,(\ell+1 + i\eta), \text{ where} \qquad (13)$$

$$\eta = \frac{\mu Z_1 Z_2 e^2}{\hbar^2 k} \qquad (14)$$

The total reaction cross section is given by

$$\sigma_R = \frac{4\pi}{k^2}\sum_{\ell=0}^{\infty}(2\ell+1)\,[CI_\ell - (CI_\ell)^2 - (CR_\ell)^2]\,, \qquad (15)$$

where CR_ℓ and CI_ℓ are the real and imaginary parts of C_ℓ.

The optical potential used in this analysis was of the form

$$V = V_c - \left\{\frac{V_R}{1+\exp\left(\frac{r-R}{a}\right)} + \frac{iW(1-\alpha)}{1+\exp\left(\frac{r-R_W}{b}\right)} + iW\alpha \exp\left[-\left(\frac{r-R_W}{1.45b}\right)^2\right]\right\}$$

$$\text{where } R = r_o A^{1/3} + r_1 \text{ and } R_W = r_W A^{1/3} + r_1\,. \qquad (16)$$

Here V_c is the Coulomb potential for which one assumes an incident point charge and an extended constant-charge density nucleus:

$$V_c = (Z_1 Z_2 e^2/2r_o A^{1/3})\,(3 - r^2/r_o A^{1/3}) \quad \text{for } r \le r_o A^{1/3}\,,$$

$$= Z_1 Z_2 e^2/2r_o A^{1/3} \quad \text{for } r > r_o A^{1/3}\,. \qquad (17)$$

The quantity α, by ranging from 0 to 1, allows the imaginary potential to assume any proportion of volume to surface absorption. The parameters r_W and b of the imaginary potential are analogous to r_o and a of the real potential. With the inclusion of r_W and b one can check those situations for which $r_W \neq r_o$ and $a \neq b$. Most of the calculations, however, were made with $r_W = r_o$. The parameters r_o, a, V_R, and W have been defined earlier in the text. The number 1.45 in the denominator of the Gaussian form factor of Eq. (16) is a normalizing factor; this number 1.45, in the special case with $0 < \alpha < 1$, insures sufficient width of the Gaussian form factor to encompass the surface region of the volume form factor.

No spin-orbit force was included in the optical potential; thus, comparison with polarization data could not be made. The spin-orbit force in general affects only slightly, however, the prediction of elastic scattering and σ_R.[92]

The spin-orbit force has been used occasionally as a means to increase the back-angle elastic scattering. In all cases we were able to get sufficient back-angle elastic scattering with the central potential without the need for two additional parameters, V_{so} and W_{so}.

C. Search Routine

The general approach used by many groups that carry out an optical-model analysis has been to search for a single set of parameters that gave a reasonable fit for nuclei throughout the periodic table. With this approach one has very little chance for fitting any unusual features that might appear in the $\sigma_{el}(\theta)$ or σ_R data. The philosophy behind this analysis has been to study each nucleus individually by varying the potential-well shape to get the optimum fit to the experimental data. It was hoped that these optical parameters would show only a systematic variation from nucleus to nucleus.

It became apparent, however, that such an extensive program as this required an automatic parameter-search routine to allow the computer program to converge to a best fit with the experimental data. First, before a search routine could be written it was necessary to investigate the effect of variations in individual parameters on the predicted quantities. This study was started on proton analysis because more information was available for protons than for other particles.

Figure 18 through 22 show th effect of the variation of individual parameters on the predicted quantity $\left(\frac{d\sigma}{d\Omega}\right)_{el} / \left(\frac{d\sigma}{d\Omega}\right)_{Ruth}$, called σ/σ_{Ruth} henceforth, where $\left(\frac{d\sigma}{d\Omega}\right)_{Ruth}$ is the differential elastic-scattering cross section predicted by the Rutherford scattering formula. It is seen from these figures that the various parameters affect σ/σ_{Ruth} differently. These curves of σ/σ_{Ruth} can be divided into four general categories, i.e., (i) the positions of maxima and minima; (ii) the extent of oscillation; (iii) the average magnitude of th diffraction pattern; and (iv) the slope of the average magnitude with respect to the coordinates σ/σ_{Ruth} and $\theta_{c.m.}$. One of the greatest problems encountered in optical-model analysis has been the tendency to find several sets of parameters that give an equally good fit to σ/σ_{Ruth}, e.g., the well-known VR^2 ambiguity. Empirically, it is easy to see why this would arise because changing V or r_o has the same effect on the curve σ/σ_{Ruth}, i.e., to move the position of the maxima and minima. The parameter W affects features (ii) and (iii), and parameter a affects features (i) and (iv). The behavior of the parameter b is unusual because it affects all four of the features. It would therefore be expected to show many interdependencies with the other parameters.

In a many-parameter problem such as this, a directional-derivative approach for a search routine usually converges quickly to a good fit. It is important, however, that the search routine not be misled by the parameter interdependencies. For this reason the parameters b and r_o, which show strong parameter interdependencies, were chosen as grid parameters. Directional derivatives are used on the

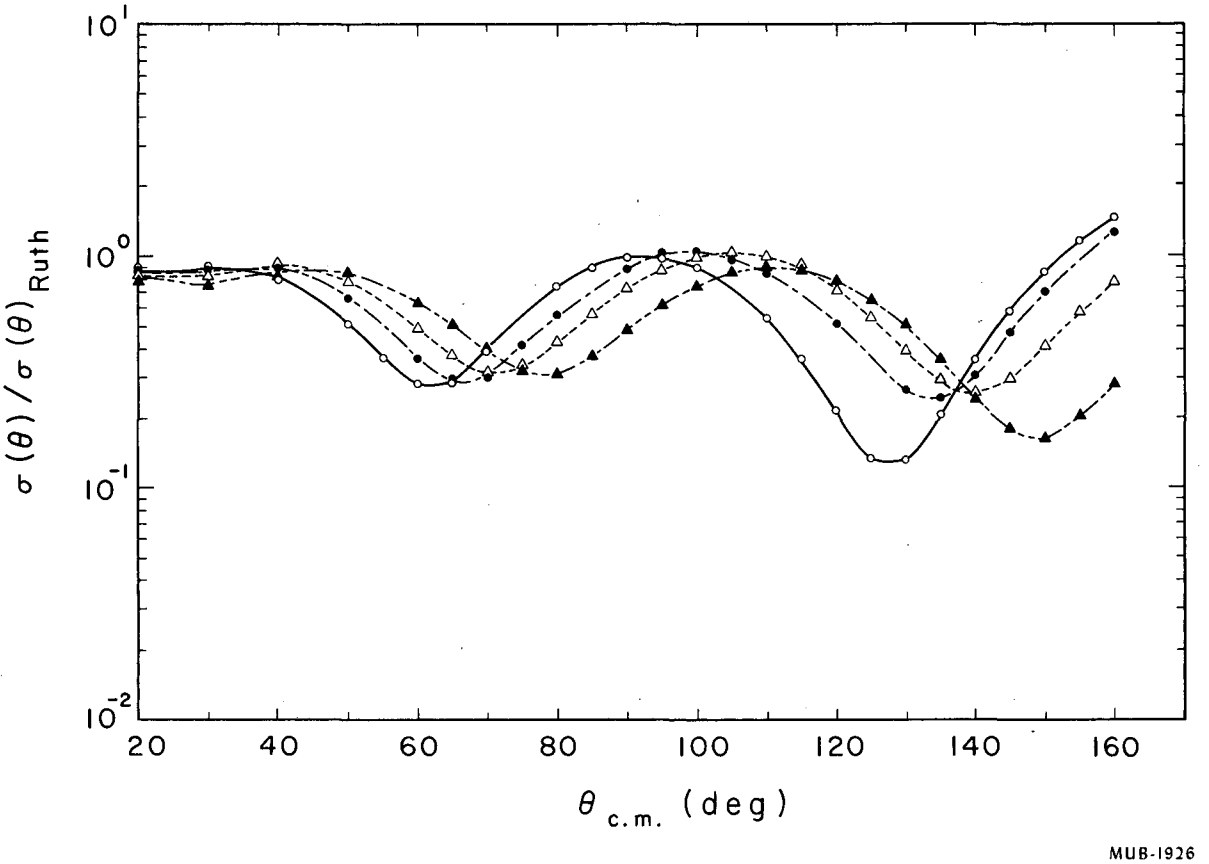

Fig. 18. Variation of the quantity σ/σ_{Ruth} for 10-MeV protons on Cu for different values of the optical-model parameter V obtained by keeping all other parameters constant:

W = 8.0 MeV; a = 0.50 F; b = 0.50 F; r_o = 1.27 F; ○: V = 60.0 MeV; ●: V = 56.0; △: V = 52.0 MeV; ▲: V = 48.0 MeV.

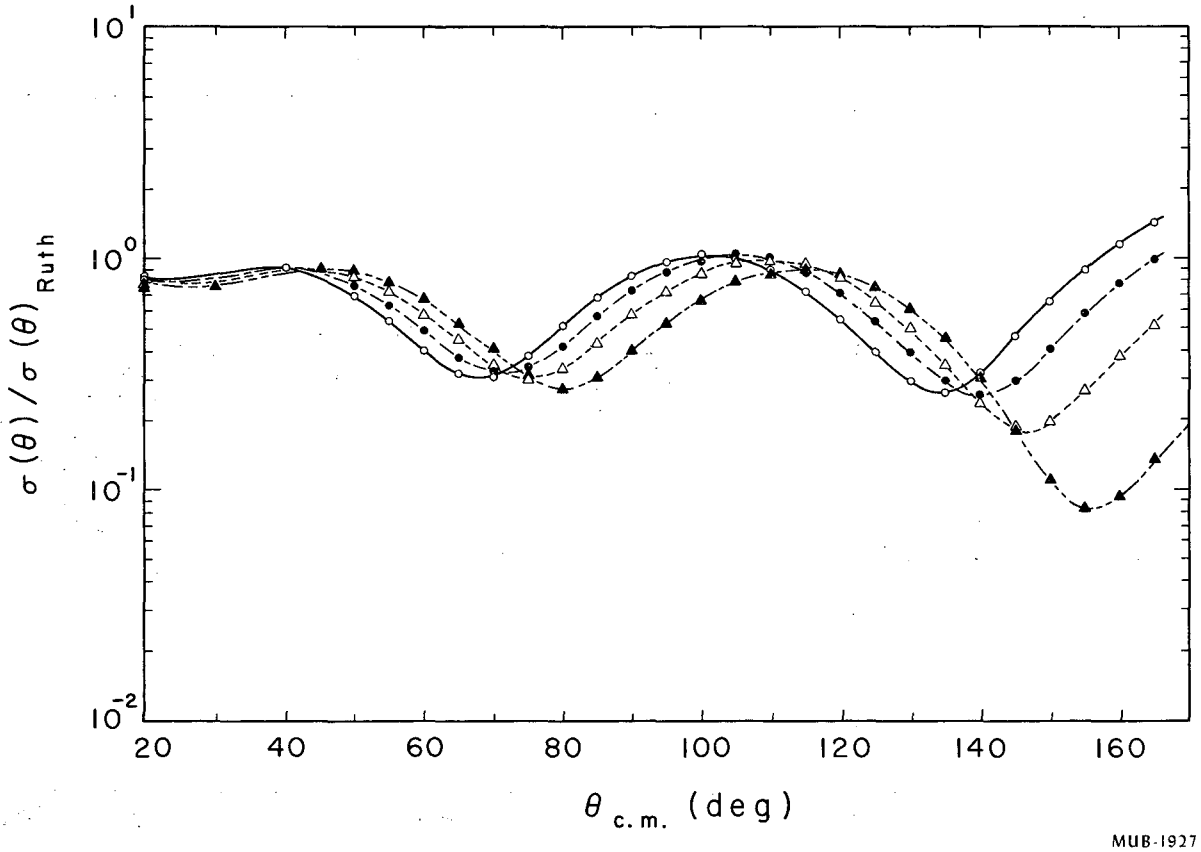

Fig. 19. Variation of the quantity of σ/σ_{Ruth} for 10-MeV protons on Cu for different values of the optical-model parameter r_o obtained by keeping all other parameters constant:

V = 52.0 MeV; W = 8.0 MeV; a = 0.50 F; b = 0.50 F;
○: r_o = 1.21 F; ●: r_o = 1.30 F; △: r_o = 1.24 F; ▲: r_o = 1.27 F.

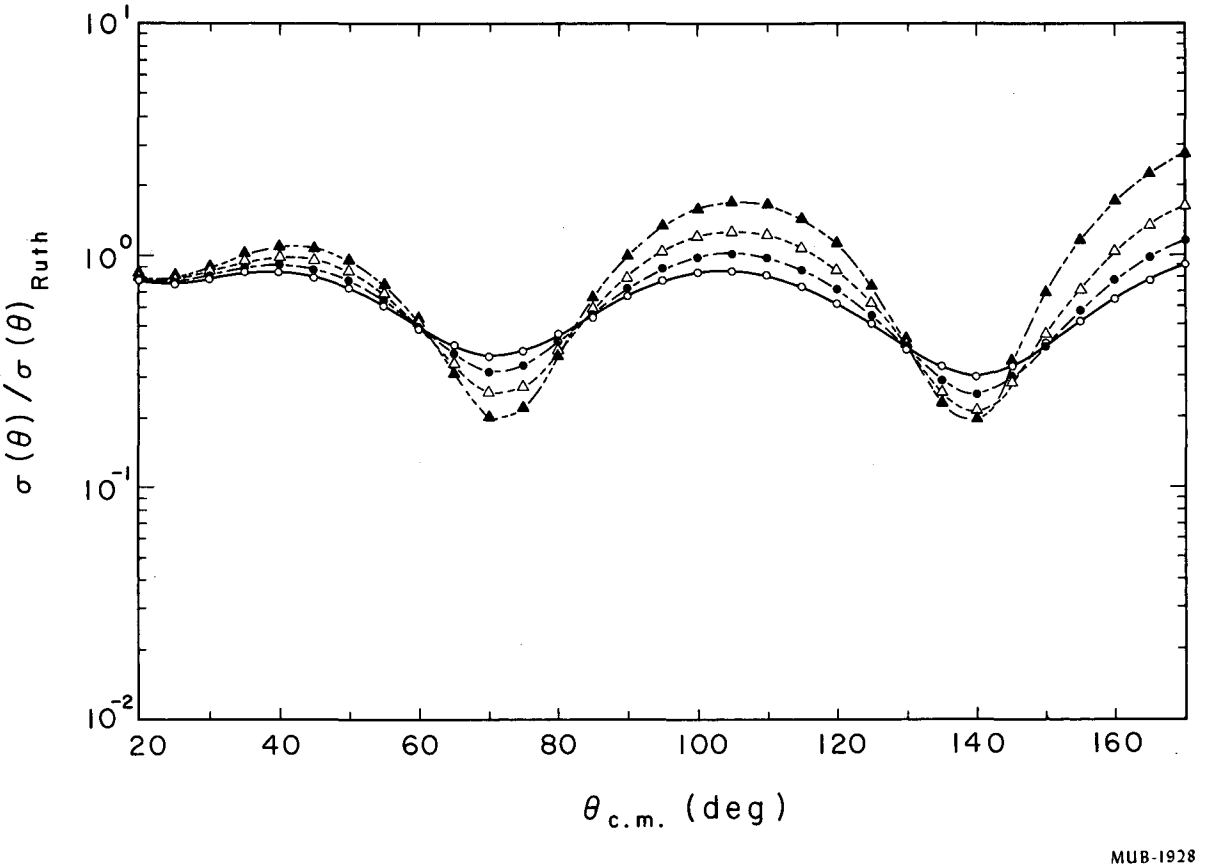

Fig. 20. Variation of the quantity σ/σ_{Ruth} for 10-MeV protons on Cu for different values of the optical-model parameter W obtained by keeping all other parameters constant:

V = 52.0 MeV; a = 0.50 F; b = 0.50 F; r_0 = 1.27 F; ○: W = 4.0 MeV ; ● : W = 6.0 MeV; △: W = 8.0 MeV; ▲: W = 10.0 MeV.

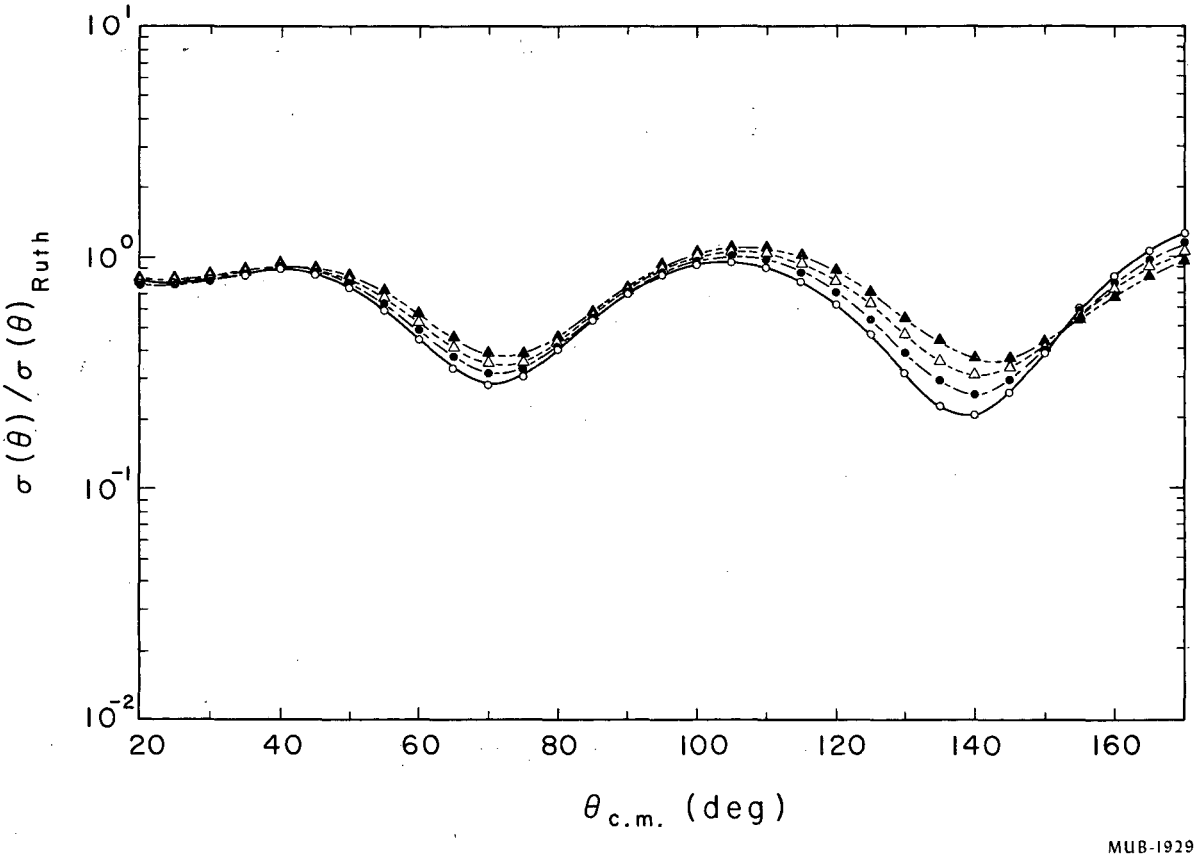

Fig. 21. Variation of the quantity σ/σ_{Ruth} for 10-MeV protons on Cu for different values of the optical-model parameter a obtained by keeping all other parameters constant:

V = 52.0 MeV; W = 8.0 MeV; b = 0.50 F; r_o = 1.27 F;
○: a = 0.44 F; ●: a = 0.47 F; △: a = 0.50 F; ▲: a = 0.53 F.

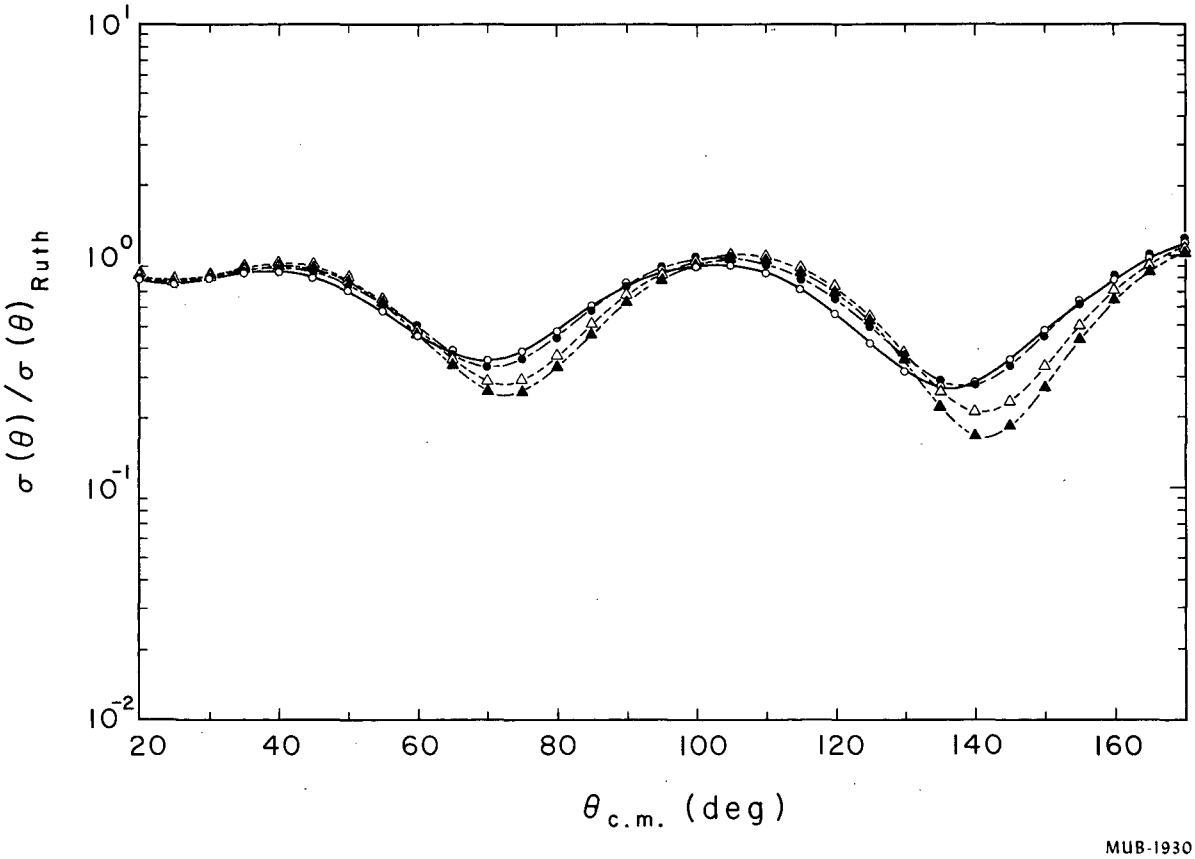

Fig. 22. Variation of the quantity σ/σ_{Ruth} for 10-MeV protons on Cu for different values of the optical-model parameter b obtained by keeping all other parameters constant:

V = 52.0 MeV; W = 8.0 MeV; a = 0.50 F; r_o = 1.27 F;
○: b = 0.10 F; ●: b = 0.30 F; △: b = 0.78 F; ▲: b = 0.90 F.

remaining parameters. For a search routine it is necessary to establish a goodness-of-fit criterion. A least-squared fit χ^2 of the following standard form was chosen:

$$\chi^2 = \sum_{i=M}^{N} \left(\frac{\sigma_i(\theta)_{pred} - \sigma_i(\theta)exp}{\left[\%\text{ error}\right]\sigma_i(\theta)exp} \right)^2, \qquad (18)$$

where M to N represents the range of experimental data.

The search routine called GULLEY uses what shall be called a "b valley" approach. It takes as its starting point a set of parameters that must be near a minimum in χ^2 space for a specified value of b and r_o. A short grid routine called ELASTIC 6 determines the value of the parameters for this starting point. From the starting point GULLEY increments the parameter b and arrives at some point A. It then determines the derivative of χ^2 with respect to the parameters V, W, and a. With this knwledge it guesses a new point B, in parameter space and reevaluates the derivatives. From the two sets of derivatives and the χ^2 values at points A and B, a new guess C is made. The program then takes the lowest two points in χ^2 space from the guesses A, B, and C, assumes χ^2 space to be parabolic in shape between these points in each of the three dimensions V, W, and A, and calculates a point D which lies somewhare between the values of the parameters at these two points. If the value of χ^2 at D is not the lowest value of the set A, B, C, and D, a new guess C' is made. A point D' is reached in a manner anlogous to point D. This procedure continues until the D point has the lowest value of χ^2. In practice this is almost always the first D guess. The program then increments b and from its knowledge of how the parameters V, W, and a changed from the starting point to point D, a new A point is chosen, and the whole A, B, C, and D procedure is repeated for this new value of b. In this manner, GULLEY works its way along the "b valley," adjusting the parameters V, W, and a to keep χ^2 at a minimum. The grid parameter r_o is then incremented and a new GULLEY run. Attempts to incorporate r_o into the dynamic set of parameters V, W, and a were unsuccessful because of the strong V-R ambiguity.

The power of this method over a standard minimum-seeking χ^2 approach is obvious. All the local minima in χ^2 corresponding to the different sets of best-fit parameters found with a minimum-seeking approach are now smoothly related to each other by their different positions along the "gulley." In other words, all the best fits can be found with a minimum of searching in the vast five-dimensional χ^2 space by searching only along a line that relates all the parameter interdependencies. Another convenient aspect of the b valley approach relates to the simple dependence of σ_R on the position along the b valley. The intersection of the experimental value of σ_R with the b valley gives directly the best parameters for a given shape potential. In many cases there is no intersection of these two quantities, and this provides a meaningful criterion for discarding a particular shape potential.

There is always the worry that besides the "gully" investigated there is another independent gully far removed in parameter space that has been missed. Careful analysis of Fig. 18 through 22 shows that only V and r_o could be raised or lowered to such an extent that the predictions of σ/σ_{Ruth} would again be in phase with the experimental data. Raising and lowering V or r_o could displace the diffraction pattern by an entire oscillation and produce another gully. Changes in r_o of this magnitude can be disregarded because of their drastic effect on σ_R. Investigation of the region of V = 100 to 120 MeV indicates that an independent gully does exist, but the χ^2 value was not as low as in the principal gully for which V has a value near 50 MeV.

FORTRAN listings of the search routine GULLEY and subroutines DIFFER and ELAS are included in the Appendix.

D. Discussion of Proton Results

Figure 23 shows a plot of the experimental $\sigma_R - \sigma_{CE}$ vs A for 10-MeV protons. The solid line in this figure stems from the optical-model predictions of σ_R by using surface absorption carried out by Bjorklund and Fernbach.[77] These results were obtained by using a standard set of parameters for all nuclei.

The experimental data show several interesting features. The appearance of a strong minimum in the region of Ni is the most intriguing. The optical model will not predict any sharp minima if one assumes that the parameters should show little, if any, variation from nucleus to nucleus (see Bjorklund's curve, Fig. 23). One might speculate that this minimum is due to a resonance in σ_{CE} that is not measured in the experimental data of $\sigma_R - \sigma_{CE}$. At 10 MeV, an excitation energy of approx 13 to 18 MeV, nuclei in this region exhibit many energy levels, and the probability that σ_{CE} would exhibit a resonance that contributes over 100mb seems remote. Even more clinching is the appearance of the same minimum in the experimental $\sigma_R - \sigma_{CE}$ for 40-MeV alphas (see Fig. 44). At this energy region σ_{CE} should certainly be negligible. The appearance of the proton magic number 28 at Ni may cause a dramatic change in the nuclear potential. If this is the case the optical parameters must show a considerable change in going from Ni (28 protons) to Cu (29 protons), which does not show a reduction of $\sigma_R - \sigma_{CE}$. An optical-model analysis of the Ni-Cu situation would seem to be a favorable case to determine whether the optical model yields any information on the structure of the nucleus. This analysis is discussed in detail later.

Another unusual feature in Fig. 23 is the extremely low value of $\sigma_R - \sigma_{CE}$ for carbon. In this energy region the N^{13} compound state has only two important modes open to it for deexcitation, the 4.43-MeV level and the ground state of C^{12}.[74] The (p,n) threshold on C^{12} is 18 MeV, and this prohibits all neutron evaporations; therefore, the experimental value of $\sigma_R - \sigma_{CE}$ is composed principally of deexcitation via the 4.43 MeV level of C^{12}. This value agrees quite well with the total integrated

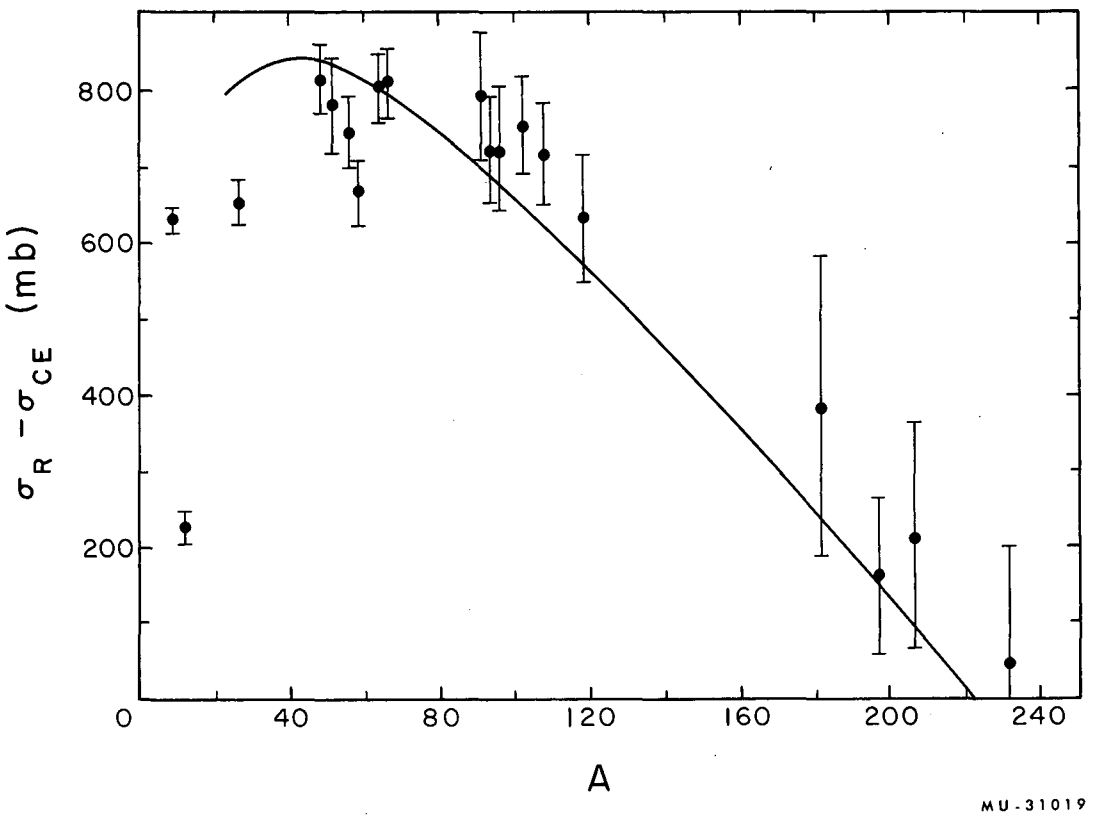

Fig. 23. The experimental results of σ_R-σ_{CE} obtained in this work for 9.9 to 10.0-MeV protons plotted as a function of A. The solid line shows the theoretical predictions of Bjorklund and Fernbach,[77] obtained by using an optical-model potential with surface absorption.

cross section for the inelastic scattering of 10-MeV protons on C^{12} (4.43-MeV level) measured by Nagahara.[45] In this particular case, σ_{CE} is expected to be quite large because it has only the one major level to compete against, and conversely, $\sigma_R - \sigma_{CE}$ should be considerably smaller than predicted values of σ_R. It should also be noted that carbon exhibits a strong energy dependence for $\sigma_R - \sigma_{CE}$ (see Tables II and III). This is also in agreement with Nagahara, who showed the existence of a sharp resonance at 10.42 MeV for both elastic and inelastic scattering. This resonance is included in the 10.16 ± 0.46-MeV measurement but not the 9.94 ± 0.46-MeV measurement, when one averages over the proper energy spread of the target. This anomaly at 10.42 MeV, which made itself felt throughout the experiment (see η_3 correction), is probably related to a resonance in the entrance channel because the $E_{c.m.}$ of this system is 9.62 MeV, the exact energy of the next level of C^{12} that is expected to be strongly excited. An extensive optical-model analysis has been carried out by Nodvik, et al. for protons on C^{12} at a variety of energies down to 12 MeV.[75]

A third feature of Fig. 23 is the general deviation of the experimental $\sigma_R - \sigma_{CE}$ from the predicted values of Bjorklund and Fernbach in the region of A=100. To clarify the discrepancy in this region, an optical analysis was made on silver. As one goes to higher-Z targets the value of $\sigma_R - \sigma_{CE}$ for 10-MeV protons drops rapidly to zero because of the Coulomb barrier.

Figure 24 listes all the total-reaction cross-section measurements in the vicinity of 10-MeV protons that have been made by different groups. Some groups, such as Carlson et al. for 9-MeV protons,[43] and Greenlees and Jarvis for 9.3-MeV protons,[42] have used beam-attenuation techniques to measure σ_R for Cu. Others, such as Meyer and Hintz, measured the partial cross section for (p,q) for several elements for which q is any charged particle, and added to it those values of (p,n) that were in the literature.[76] Remeasurement of the (p,n) cross sections (see Albert and Hansen[77] and Wing and Huizenga[78]) give different values for σ_R when added to the (p,q) cross sections from Meyer and Hintz. Benveniste et al. also measured the (p,q) cross section for Cu at 10 MeV.[79]

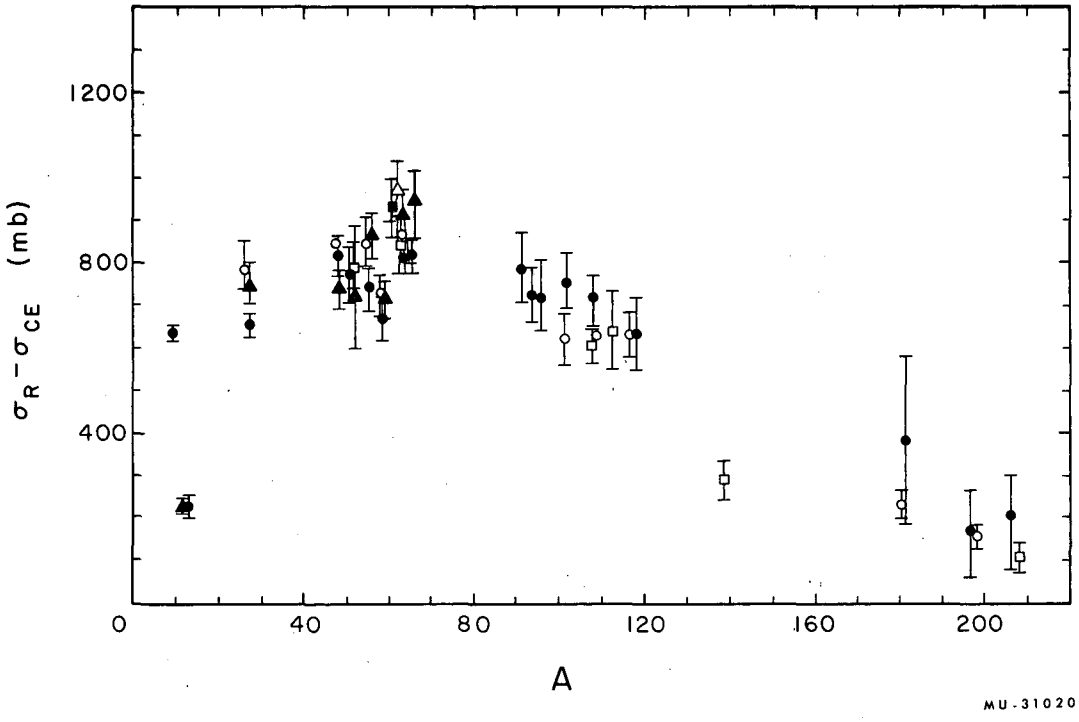

Fig. 24. All experimental data for protons on $\sigma_R - \sigma_{CE}$ in the region of 10 MeV plotted as a function of A:

Results of this experiment;

from Albert and Hansen (p,n),[77] and Meyer and Hintz (p,q);[76]

from Wing and Huizenga (p,n),[78] and Meyer and Hintz (p,q);[76]

from Meyer and Hintz;[76] from Carlson et al;[43]

and from Greenlees and Jarvis.[42]

The agreement between the trend of the data of Albert and Hansen, and of Wing and Huizenga, and the data of this experiment is satisfactory (see Fig. 24). The beam-attenuation values for Cu at about 9 MeV are larger than the results of this experiment and those from the summation technique. Since they are measured at 9 MeV, they would be expected to be smaller because the effects of the Coulomb barrier are more strongly felt at lower energies.

E. Optical-Model Analyses of Proton Results

1. Copper

Figure 25 shows the results of the GULLEY search-routine analysis on Cu^{63} with the use of a Woods-Saxon (volume absorption) form factor for the imaginary part of the optical potential. This figure is a plot of b vs r_o, the two grid parameters of GULLEY. The contour lines are the values of χ^2 obtained in fitting Benveniste's results[79] for the elastic scattering of 10.2-MeV protons by Cu^{63}. At each point in the contour, the parameters V, a, and W have been adjusted to give a minimum in χ^2. The dashed lines give the predicted values of σ_R. This analysis was carried out with $r_o = r_W$ (see p.69 for analysis with $r_o \neq r_W$). It is quite apparent that the valley of best fit is a function of both b and r_o.

Another manner in which the results of the analysis may be plotted is shown in Figs. 26, 27, and 28. This plot along the "b valley", with r_o held constant is analogous to taking a vertical slice out of Fig. 25. Figures 26, 27, and 28 display the behavior of V, a, and W vs b at the value $r_o = 1.30$ F. The variation of V, a, and W with respect to changes in r_o can be shown by taking a horizontal slice out of Fig. 25. Figures 29, 30, and 31 show this variation of V, a, and W for b = 0.38 F. Figures 25 through 31 illustrate some of the interdependencies of the parameters,

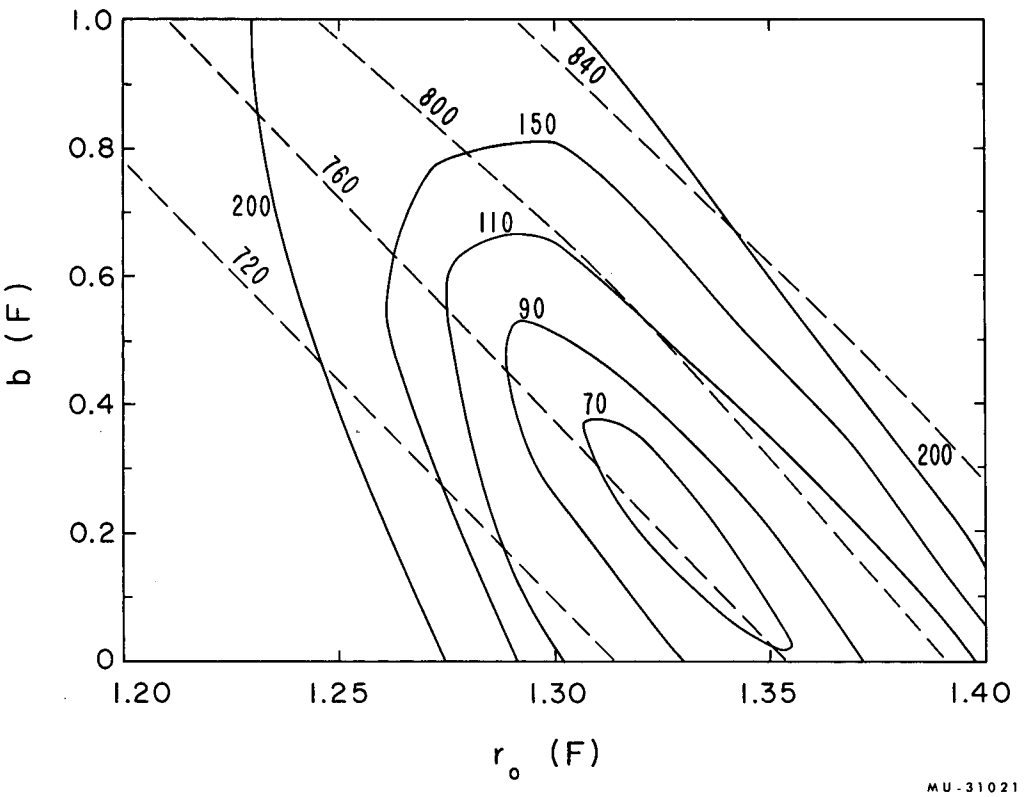

Fig. 25. A contour map of b vs r_o for 10.20-MeV protons on Cu^{63} obtained by using volume absorption. The contours give the value of χ^2 obtained in fitting $\sigma_{el}(\theta)$. The dashed lines show the predicted values of σ_R. For each point in the b-r_o grid the other parameters have been adjusted to minimize χ^2; $r_o = r_w$.

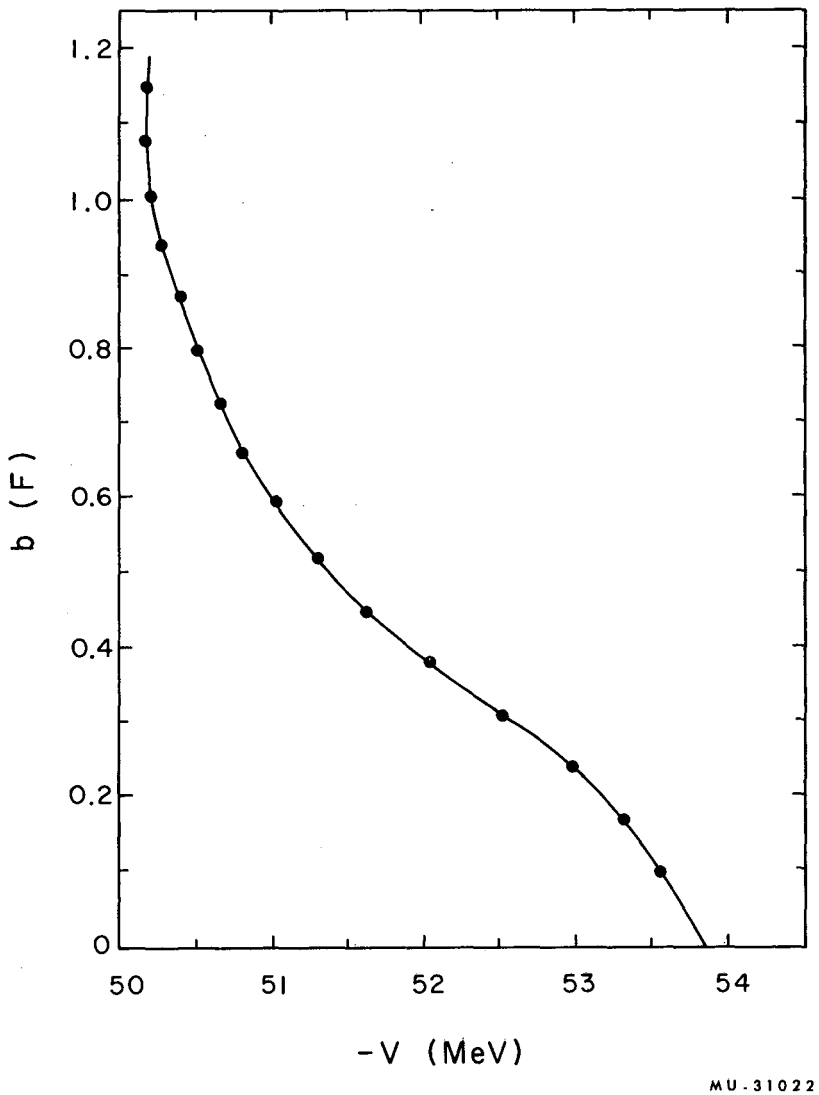

Fig. 26. A plot of b vs V for a constant r_o, equivalent to a vertical slice out of Fig. 25 in the V dimension. The parameter r_o = 1.30 F.

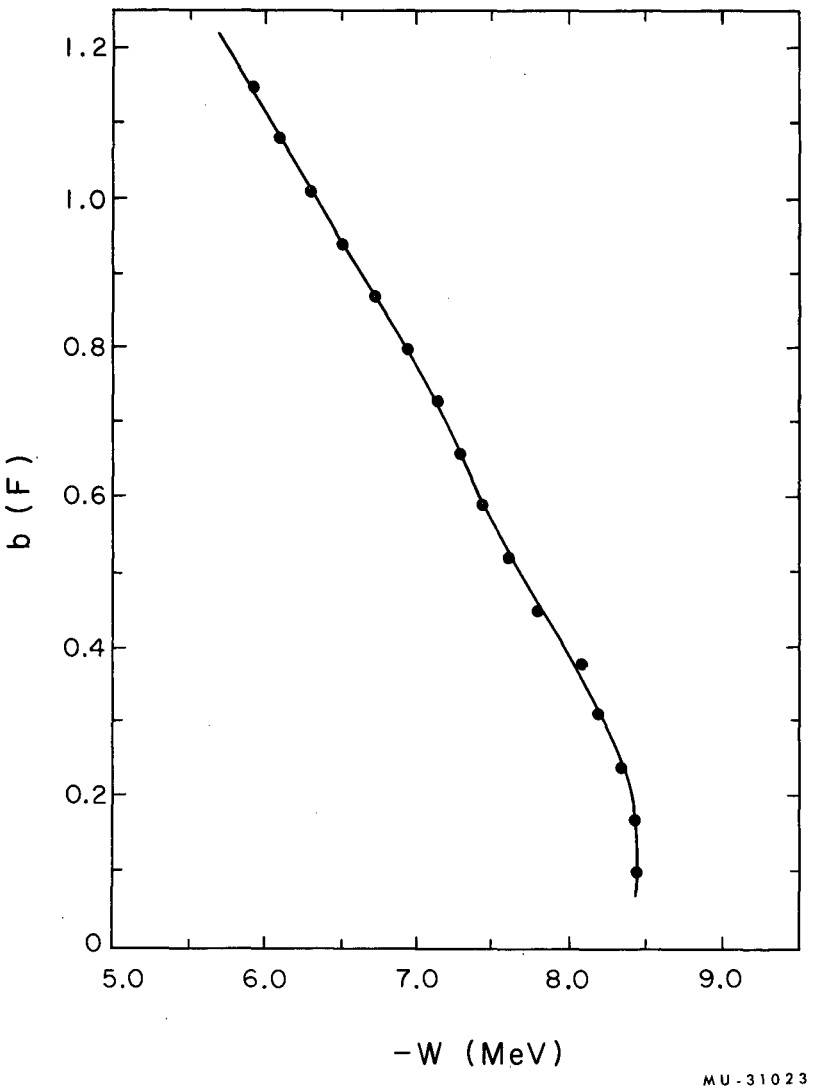

Fig. 27. A plot of b vs W for a constant r_o, equivalent to a vertical slice out of Fig. 25 in the W dimension; r_o = 1.30 F.

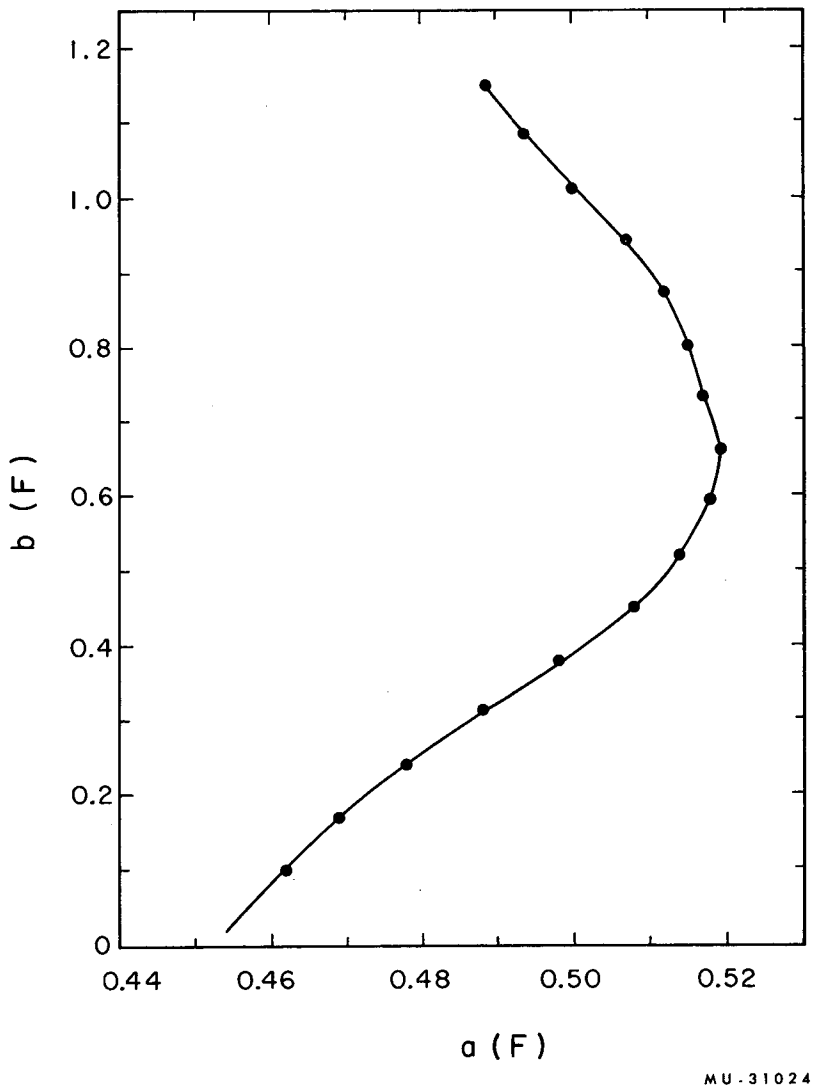

Fig. 28. A plot of b vs a for a constant r_o, equivalent to a vertical slice out of Fig. 25 in the a dimension; r_o = 1.30 F.

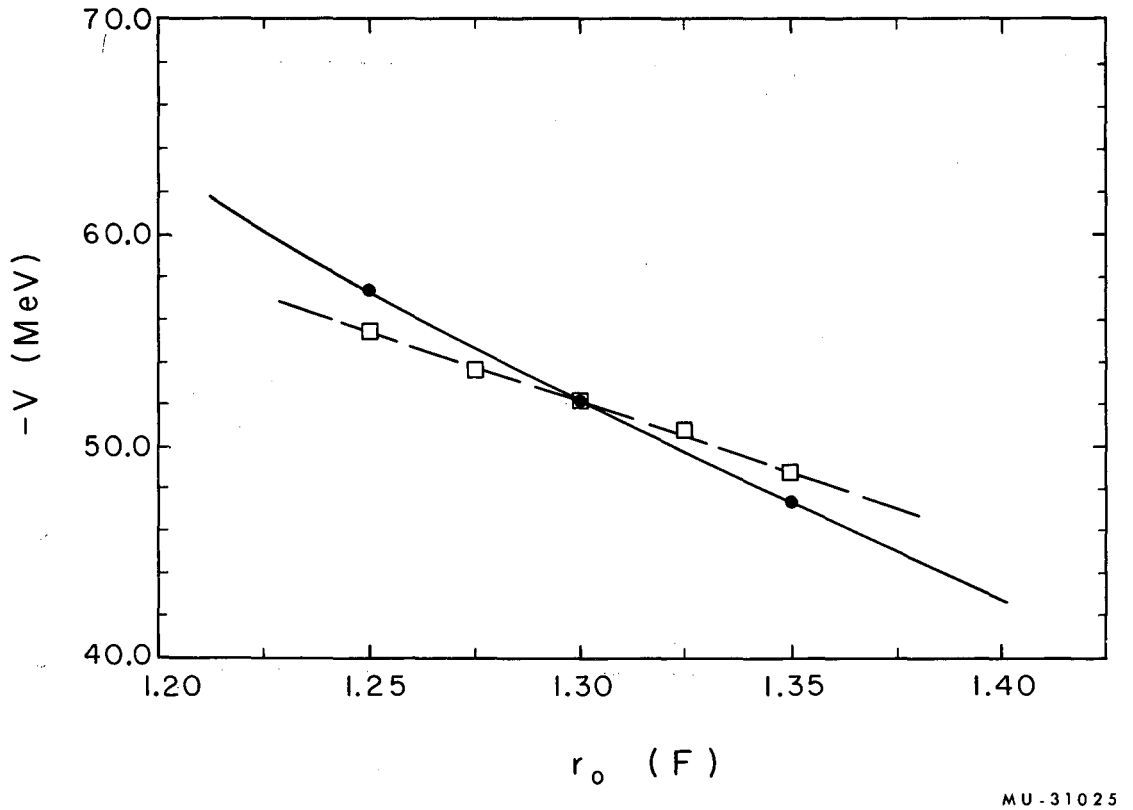

Fig. 29. The solid line is a plot of V vs r_o at a constant b, equivalent to a horizontal slice from Fig. 25. In the V dimension b = 0.38 F. The dashed line shows the variation of V vs r_o along the "b valley," i.e., points of lowest χ^2.

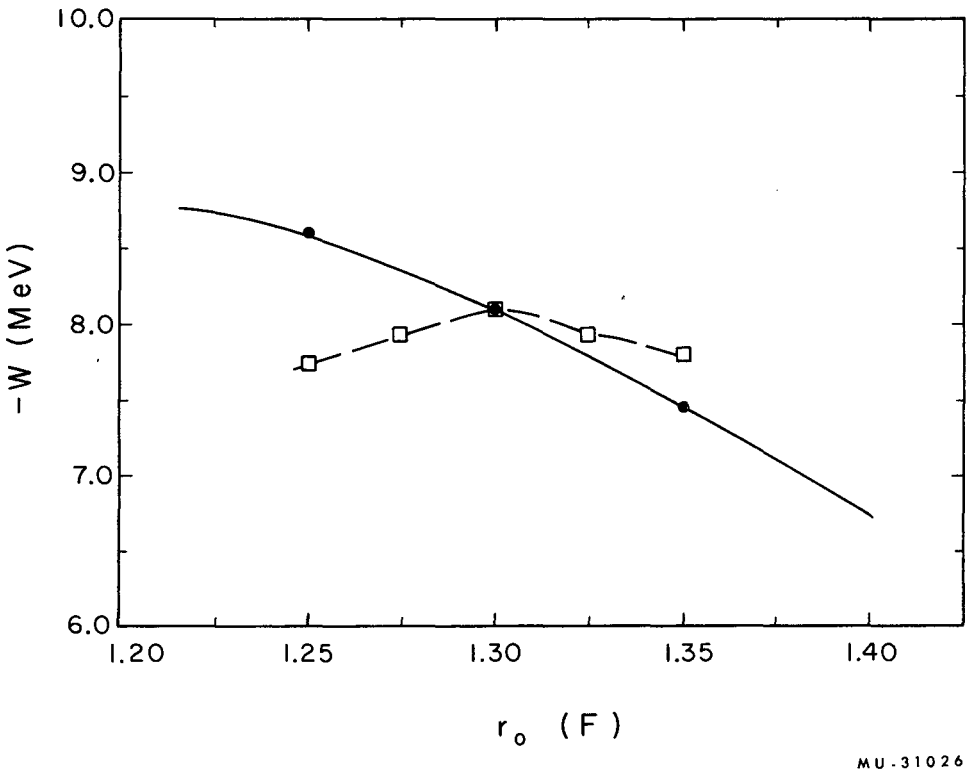

Fig. 30. The solid line is a plot of W vs r_o at a constant b, equivalent to a horizontal slice from Fig. 25 in the W dimension at b = 0.38 F. The dashed line shows the variation of W vs r_o along the "b valley," i.e., points of lowest χ^2.

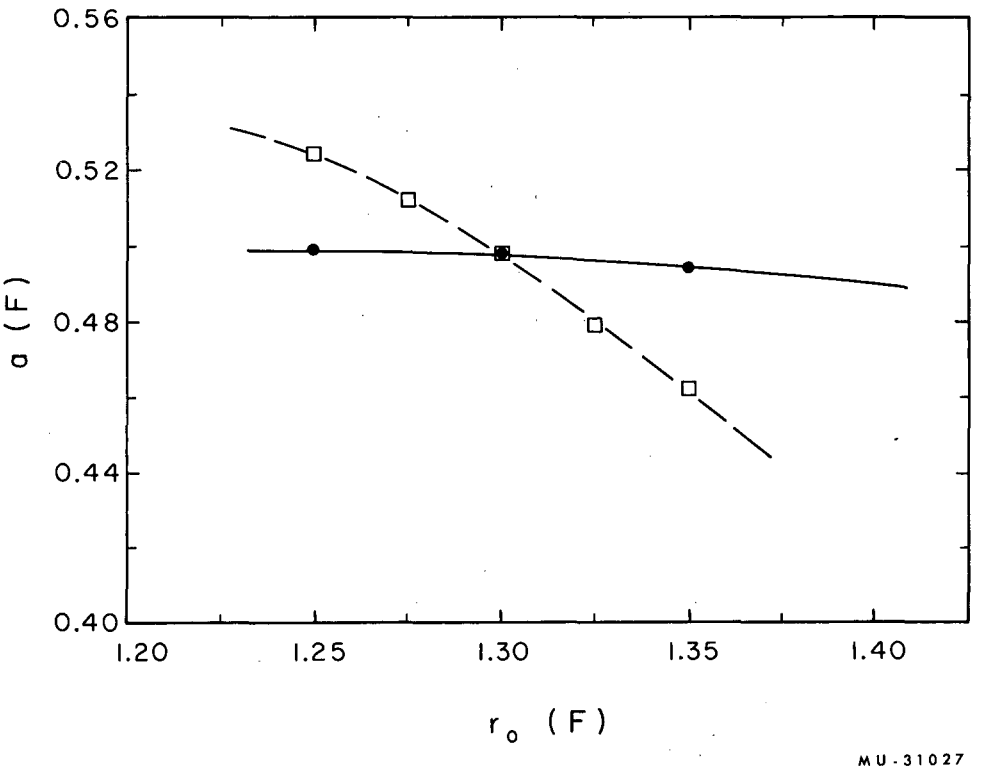

Fig. 31. The solid line is a plot of a vs r_o at a constant b, equivalent to a horizontal slice from Fig. 25 in the a dimension at b = 0.38 F. The dashed line shows the variation of a vs r_o along the "b valley," i.e., points of lowest χ^2.

particularly V-R and b-w. The V-R relationship fits quite accurately the equation VR^n = CONSTANT, where n = 2(1 + E/V). This equation, derived from a square-well potential, keeps constant the number of waves within the nucleus.

Table VI lists the best fits obtained at different values of r_o. The outstanding feature of this table (see also Fig. 25) is the constancy of σ_R at 760mb. Contrary to what had been suggested,[50] accurate measurement of σ_R will not necessarily remove the VR^n ambiguity if one stays in the valley of minimum χ^2. Figure 32 shows a plot of σ/σ_{Ruth} vs $\theta_{c.m.}$. The solid line is an optical-model prediction made by using volume absorption with the parameters chosen from the area of minimum χ^2.

An experimental value of 840 ± 30mb for 10-MeV protons on natural Cu has been arrived at by averaging the results of Albert and Hansen,[77] of Wing and Huizenga,[78] and of this work. The average σ_R from these experiments was adjusted slightly in order to coincide with the proton energy of 10.2 MeV, the energy of the elastic-scattering data on Cu^{63}. There is expected to be little difference in σ_R between Cu^{63} and Cu^{65}. It should, therefore, be safe to use the σ_R for natural Cu when one makes comparisons with the elastic-scattering data of Cu^{63}. A predicted σ_R of 840mb (see Fig. 25) at no time comes close to intersecting the valley of minimum χ^2.

It had been suggested by Hodgson that, if need be, one could always increase the value of σ_R by increasing the radius of the imaginary potential beyond that of the real potential.[80] In hopes of raising the predicted σ_R to 840mb while using a volume absorption potential, a search was carried out in which r_W the radius constant of the imaginary potential was varied; Figure 33 gives the results of this analysis. Again, the outstanding feature was the constancy of σ_R at 760mb, if one stays in the valley of minimum χ^2. Any change in σ_R caused by varying r_W was always compensated for by changing W in order to retain a good fit to the elastic-scattering data. Table VII lists the best fits obtained at different r_W for r_o = 1.30 F. From the results of this analysis it seems safe to say that volume absorption cannot fit simultaneously the elastic-scattering and σ_R data for 10-MeV protons on Cu^{63}.

Table VI. Sets of "best fit" parameters for 10.20-MeV protons on Cu^{63} obtained at different values of r_o by using volume absorption; $r_o = r_W$.

r_o (F)	b (F)	a (F)	-V (MeV)	-W (MeV)	χ^2	σ_R (mb)
1.250	0.70	0.523	55.6	7.80	160	760
1.275	0.54	0.512	53.8	7.95	110	761
1.300	0.38	0.498	52.1	8.10	75	760
1.325	0.22	0.478	50.4	7.95	60	763
1.350	0.08	0.460	48.8	7.80	70	765

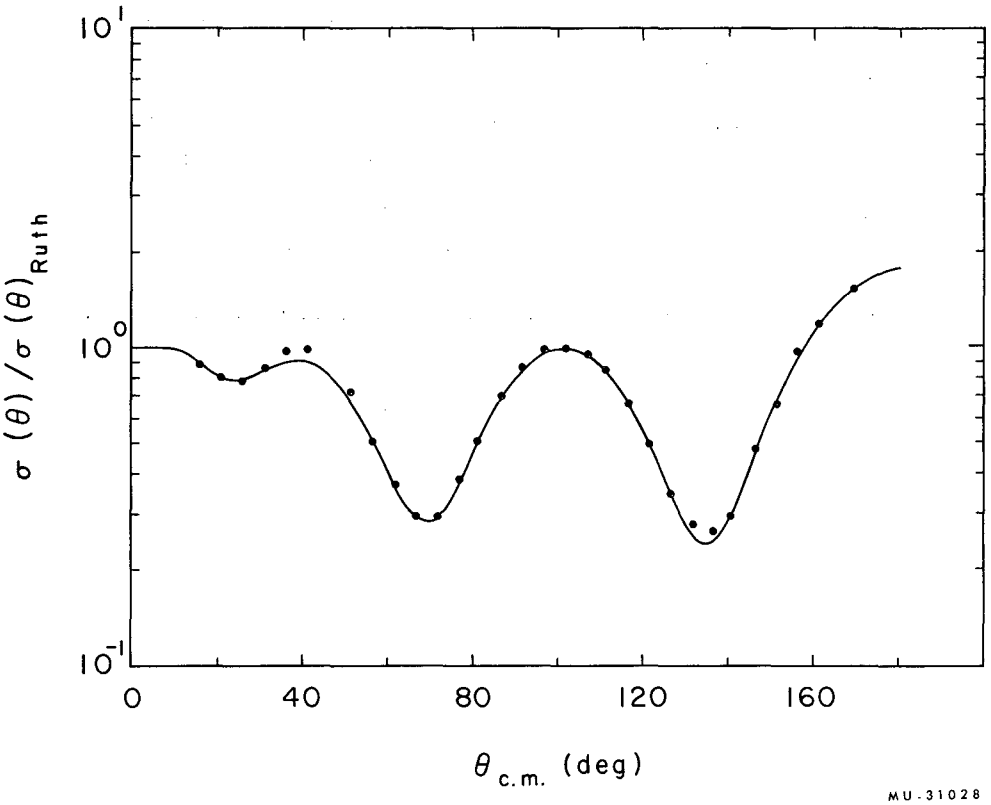

Fig. 32. A plot of σ/σ_{Ruth} is shown for 10.20-MeV protons on Cu^{63}. The solid line is the predicted value of σ/σ_{Ruth} by using volume absorption. The optical-model parameters for this figure are chosen from the area of minimum χ^2 (see Fig. 25) and are listed in Table VI at r_o = 1.325 F. The dots are the experimental points of Benveniste.[79]

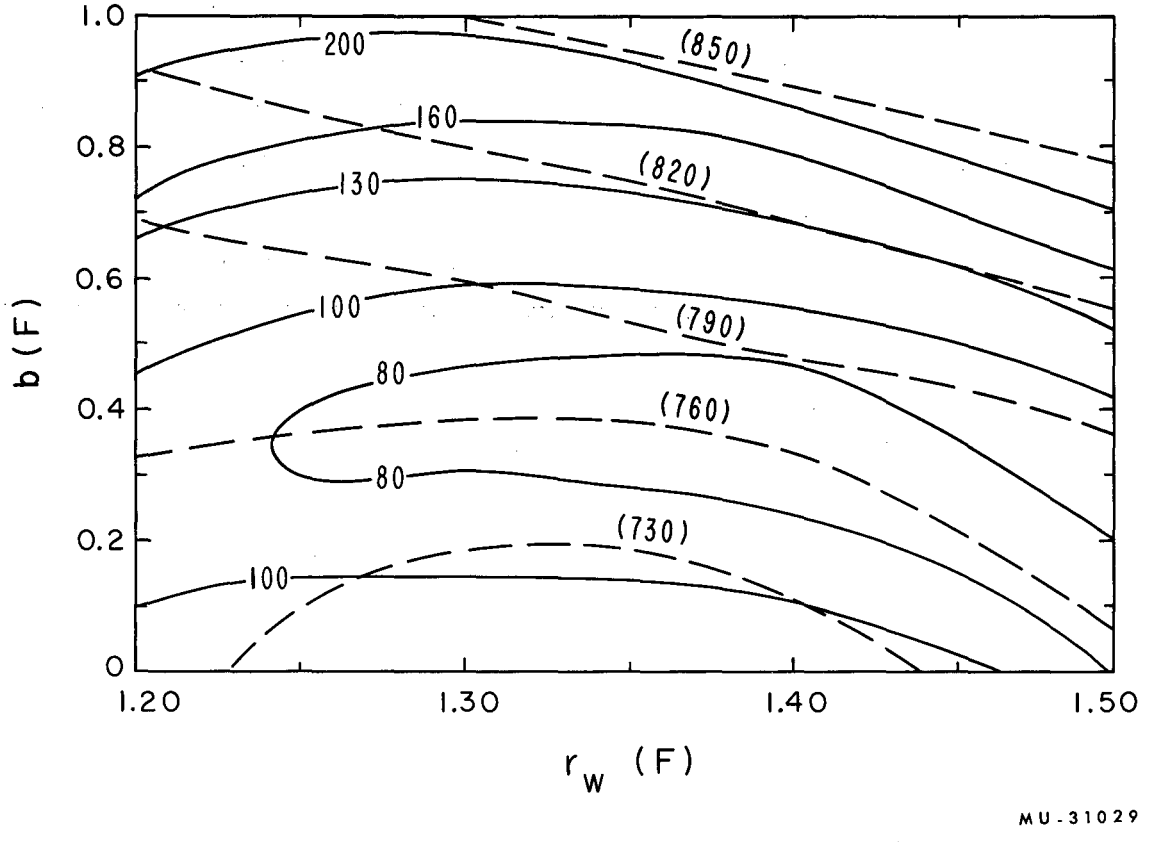

Fig. 33. A contour map of b vs r_W for 10.20-MeV protons on Cu^{63} obtained by using volume absorption. The contours give the value of χ^2 obtained in fitting $\sigma_{el}(\theta)$. The dashed lines show the predicted values of σ_R. For each point in the b-r_W grid the parameters V, a, and W have been adjusted to minimize χ^2; r_o = 1.30 F.

Table VII. Sets of "best fit" parameters for 10.20-MeV protons on Cu^{63} obtained at different values of r_W by using volume absorption; r_o = 1.30 F.

r_W (F)	b (F)	a (F)	-V (MeV)	-W (MeV)	χ^2	σ_R (mb)
1.20	0.10	0.46	52.5	9.6	90	750
1.30	0.38	0.50	52.1	8.1	76	760
1.40	0.38	0.52	51.5	6.9	72	770
1.50	0.16	0.54	51.5	6.3	75	770

Figure 34 displays the results of the GULLEY search routine on Cu^{63} with the use of a Gaussian (surface absorption) shape for the imaginary potential with $r_o = r_W$. The experimental value of 840 ± 30mb for σ_R is seen to intersect the area of minimum χ^2. Table VIII lists the best fits obtained for different values of r_o. Attempts at making $r_W > r_o$ materially worsened the fit to the elastic scattering. Figure 35 shows a plot of σ/σ_{Ruth} vs $\theta_{c.m.}$, for which the solid line is an optical-model prediction with surface absorption corresponding to the area of minimum χ^2 and the dots are the experimental points of Benveniste.[79]

Table IX gives the results obtained for two different r_o's with the use of a potential that contained both a volume and a surface term in the imaginary potential [$\alpha = 0.5$; see Eq. (16) for the optical potential used in this analysis]. Although an extensive search was not carried out, the results seem to fall between the volume and the surface fits in their ability to fit both σ_R and the elastic scattering.

For the case of 10-MeV protons interacting with Cu, surface absorption for the imaginary potential is clearly superior to volume absorption. With the surface term it is possible to obtain excellent fits to both the elastic scattering and σ_R data, whereas with the volume absorption it is impossible to fit the σ_R measurement.

2. Nickel

The GULLEY search-routine analysis on Ni using volume absorption for the imaginary potential, was not able to give any adequate fit to the elastic-scattering data of Hintz for 9.85-MeV protons.[50] With volume absorption, the optical-model calculations were unable to predict enough scattering in the backward angles. In a previous attempt to analyze this same system Glassgold et al.[17] suggested that this difficulty was due to large amounts of σ_{CE}, which the optical model does not include in its prediction of $\sigma_{SE}(\theta)$. It was thought that Ni^{58} might have a relatively high σ_{CE} because a high (p,n) threshold (≈10 MeV) prohibits deexcitation via neutrons, and thus increases the probability of de-excitation of the compound state through the entrance channel.

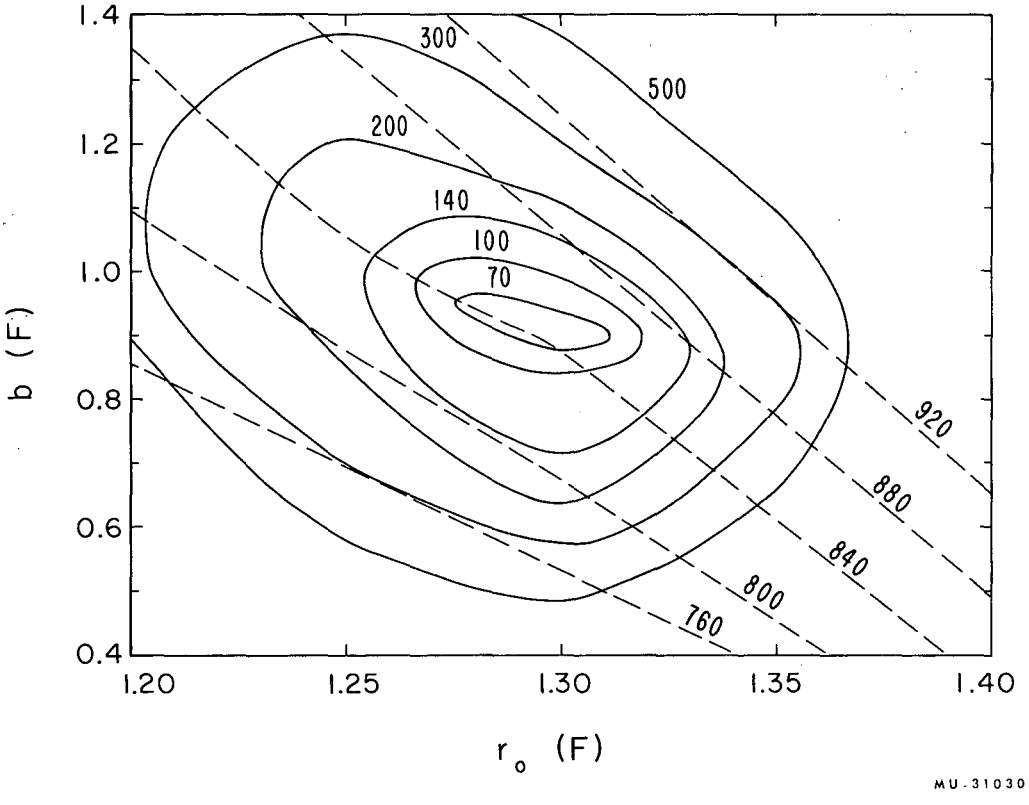

Fig. 34. A contour map of b vs r_o for 10.20-MeV protons on Cu^{63} obtained by using surface absorption. The contour gives values of χ^2 obtained in fitting $\sigma_{el}(\theta)$. The dashed lines show the predicted values of σ_R. For each point in the b-r_o grid the other parameters have been adjusted to minimize χ^2; $r_o = r_W$.

Table VIII. Sets of "best fit" parameters for 10.20-MeV protons on Cu^{63} at different values of r_o by using surface absorption; $r_o = r_W$.

r_o (F)	b (F)	a (F)	-V (MeV)	-W (MeV)	χ^2	σ_R (mb)
1.250	1.00	0.624	52.7	9.2	140	835
1.275	0.96	0.623	50.6	9.6	69	846
1.300	0.92	0.623	48.5	10.0	50	855
1.325	0.89	0.629	46.5	10.4	128	882
1.350	0.86	0.631	44.5	10.8	240	900

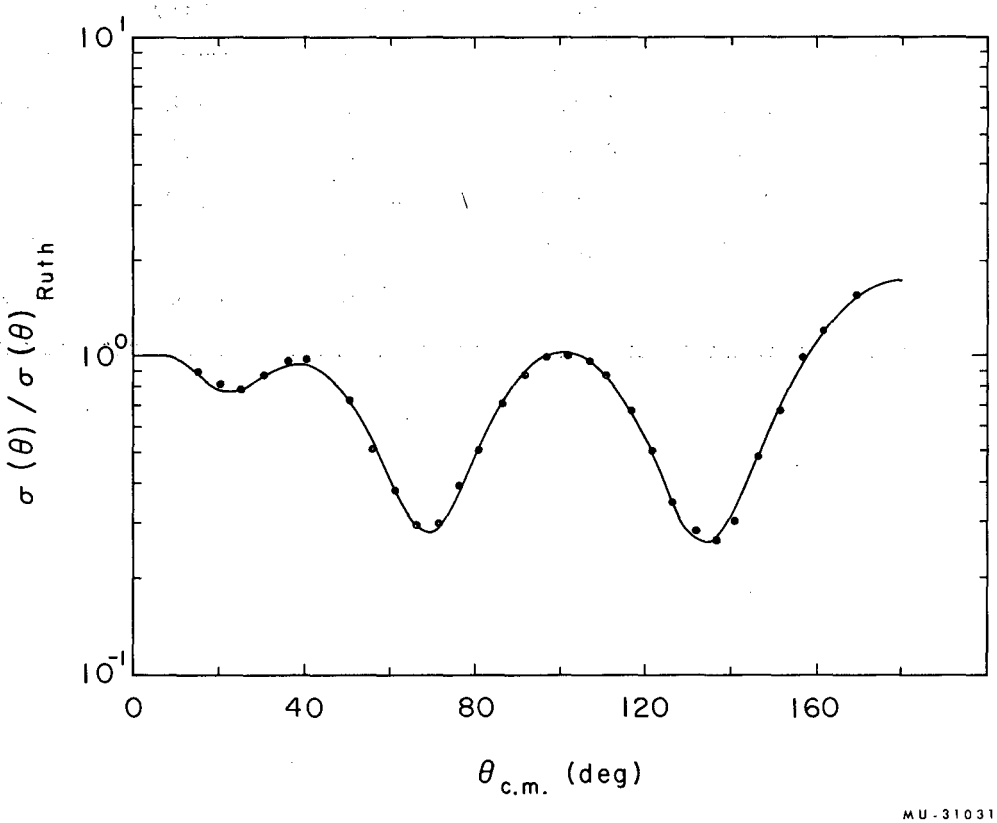

Fig. 35. A plot of σ/σ_{Ruth} is shown for 10.20-MeV protons on Cu^{63}. The solid line is the predicted value of σ/σ_{Ruth} obtained by using surfacing absorption. The optical-model parameters for this fit are chosen from the area of minimum χ^2 (see Fig. 34), and are listed in Table VIII at $r_o = 1.300$ F. The dots are the experimental points of Benveniste.[79]

Table IX. Sets of "best fit" parameters for 10.20-MeV protons on Cu^{63} at different values of r_o by using a combination of surface and volume absorption; $\alpha = 0.5$ and $r_o = r_W$.

r_o (F)	b (F)	a (F)	-V (MeV)	-W (MeV)	χ^2	σ_R (mb)
1.25	0.87	0.565	54.4	8.5	155	793
1.30	0.59	0.550	51.0	10.3	73	783

The GULLEY search routine using surface absorption, however, was able to give excellent fits to the experimental data of Hintz (see Figs. 36 and 37 and Table X). The experimental value of $\sigma_R - \sigma_{CE}$ of 680 ± 30mb, obtained by averaging the data of Meyer and Hintz[76] and results of this paper, is seen to intersect the area of minimum χ^2 (see Fig. 36). One can conclude from this that σ_{CE} is probably quite small, for otherwise optical-model predictions of σ_{SE} and σ_R would not agree so well with the experimental values of $(\sigma_{SE} + \sigma_{CE})$ and $(\sigma_R - \sigma_{CE})$. If this is the case the large minimum in the experimental value of $\sigma_R - \sigma_{CE}$ at Ni (see Fig. 23) must be due to a decrease in σ_R.

Comparison of the optical-model parameters listed in Table XI for Cu and Ni should give some hint as to the reason for the dramatic change in σ_R. Figures 38 and 39 show a plot of the real and imaginary potentials for Cu and Ni, respectively. It is probably unwise to attach very much physical meaning to the parameters because the local optical-model parameters are just an approximation to a more realistic nonlocal potential. The nonlocal parameters are not so readily understood in terms of physical meaning. It should suffice to say that the real potentials for the two nuclei are quite similar. The differences lie in the imaginary potential, where Ni exhibits a much narrower region on the surface for absorption. Whether this should be ascribed to Ni's being a proton magic number or some other structural feature remains unanswered. In view of the excellent fits obtained with Ni and Cu for both σ_R and $\sigma_{SE}(\theta)$, one suspects that optical-model parameters fluctuate rather than remain constant as one goes from nucleus to nucleus. To check this critical point, an isotropic distribution for σ_{CE} was subtracted from the Ni $\sigma_{el}(\theta)$ data to see if optical-model fits could be obtained by using the "Cu parameters." Fair agreement with the resulting angular distribution was reached only if $\sigma_{CE} \leq 40$mb, a value not large enough to remove the $\sigma_R - \sigma_{CE}$ difference between Ni and Cu. Also the σ_R prediction for Ni (825mb) with the use of the "Cu parameters" was in poor agreement with the experimental value. Some improvement in this fit to $\sigma_{SE}(\theta)$ and

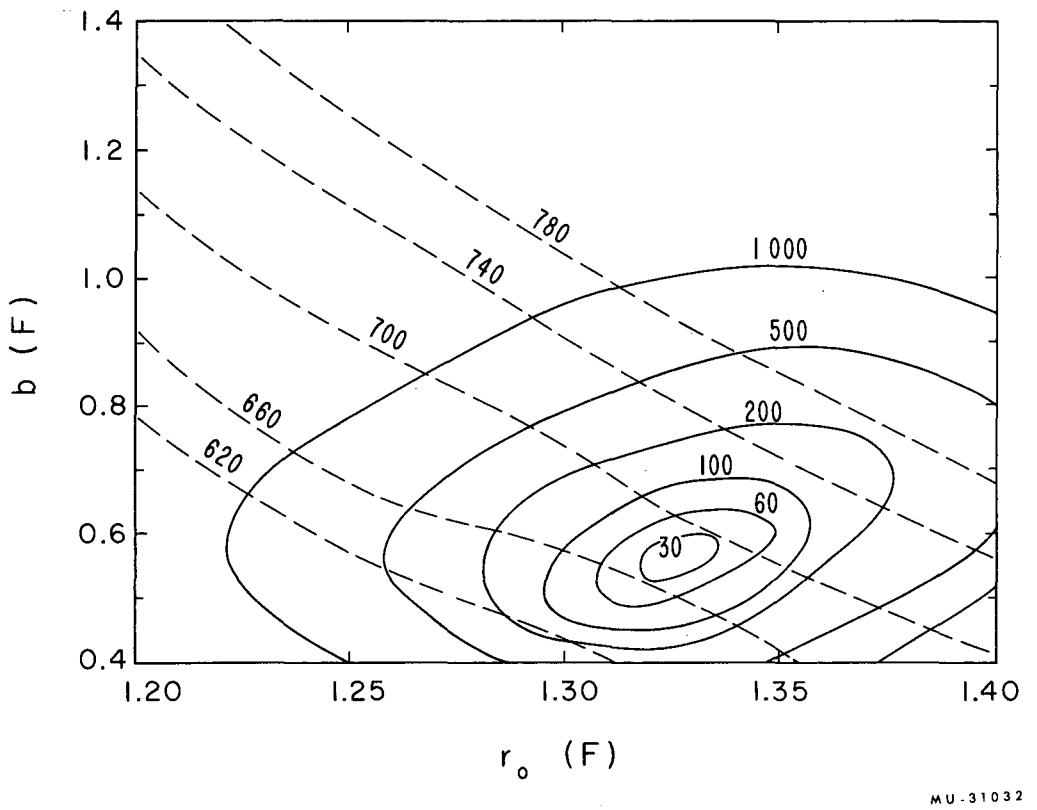

Fig. 36. A contour map of b vs r_o for 9.85-MeV protons on Ni obtained by using surface absorption. The contours give values of χ^2 obtained in fitting $\sigma_{el}(\theta)$. The dashed lines show the predicted values of σ_R. For each point in the b-r grid the other parameters have been adjusted to minimize χ^2; $r_o = r_w$.

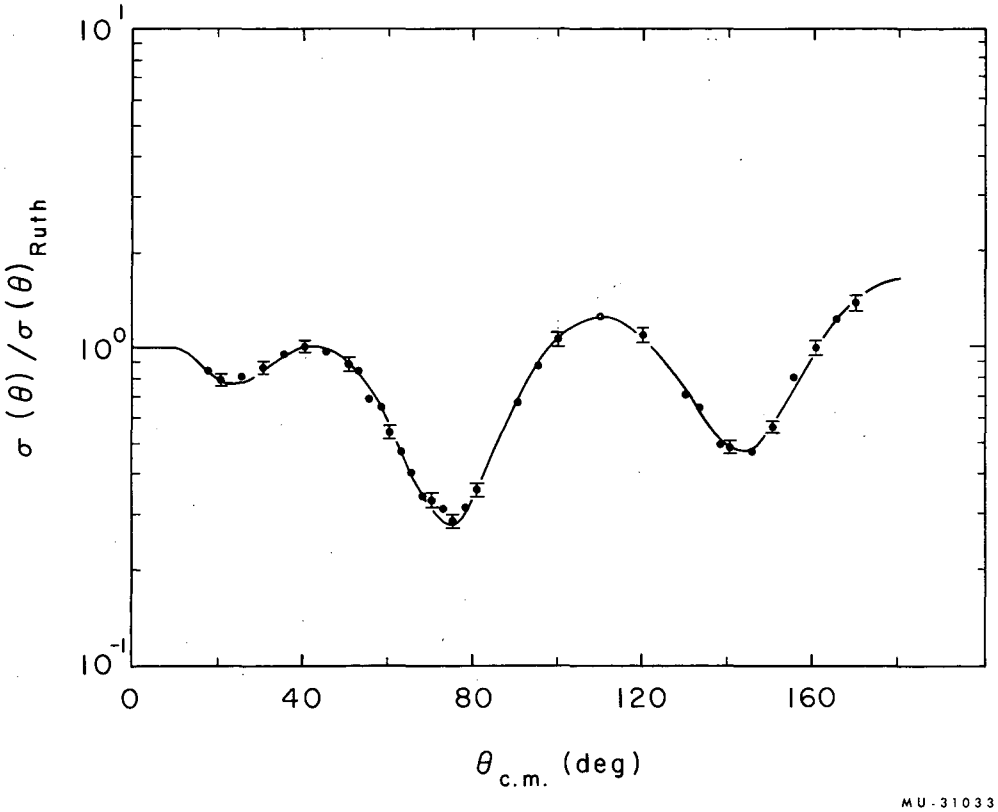

Fig. 37. A plot of σ/σ_{Ruth} is shown for 9.85-MeV protons on Ni. The solid line is the predicted value σ/σ_{Ruth} obtained by surfacing absorption. The optical-model parameters for this fit are chosen from the area of minimum χ^2 (see Fig. 36) and are listed in Table X, at $r_o = 1.300$ F. The dots are the experimental points of Hintz.[50]

Table X. Sets of "best fit" parameters for 9.85-MeV protons on Ni at different values of r_o by using surface absorption; $r_o = r_W$.

r_o (F)	b (F)	a (F)	-V (MeV)	-W (MeV)	χ^2	σ_R (mb)
1.250	0.62	0.572	53.5	15.5	37	642
1.275	0.59	0.575	51.5	15.9	21	653
1.300	0.57	0.578	49.6	16.1	15	667
1.325	0.55	0.580	47.7	16.2	19	679
1.350	0.55	0.580	45.8	15.6	37	697
1.375	0.53	0.588	44.1	15.8	68	715

Table XI. Comparison of the "best fit" set of parameters for 10.20-MeV protons on Cu^{63} and 9.85-MeV protons on Ni; both sets use surface absorption; $r_o = r_W$.

Element	r_o (F)	b (F)	a (F)	-V (MeV)	-W (MeV)	σ_R (predicted) (mb)	$(\sigma_R - \sigma_{CE})_{exp}$ (mb)
Ni	1.30	0.57	0.578	49.6	16.1	667	680 ± 30
Cu	1.29	0.93	0.623	49.3	9.9	853	840 ± 30

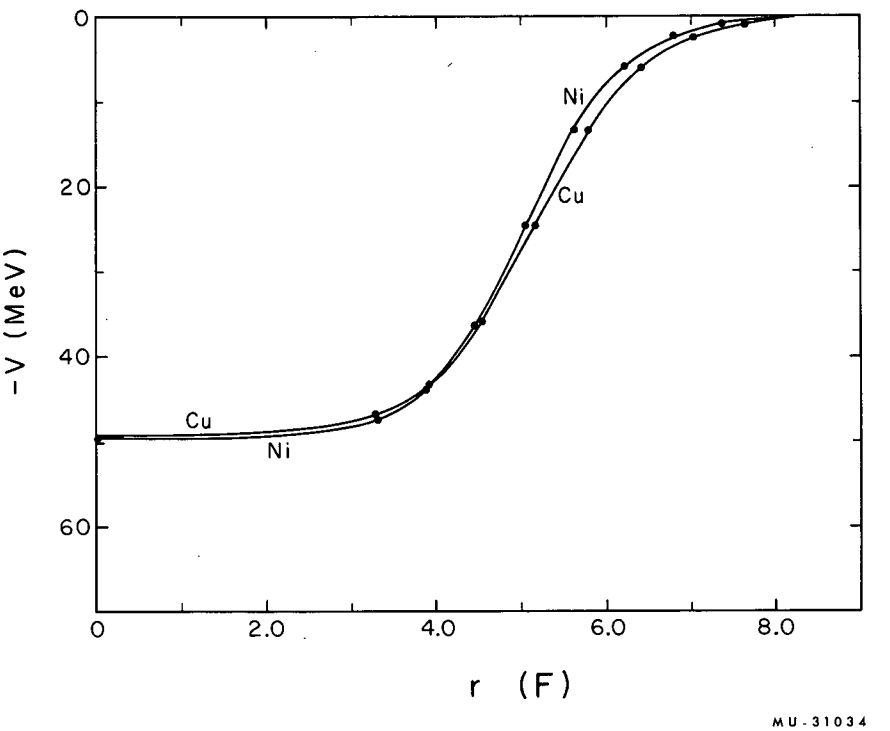

Fig. 38. Comparison of the "best fit" real optical-model potentials obtained for 9.85-MeV protons on Ni and 10.20-MeV protons on Cu^{63}. The parameters are listed in Table XI.

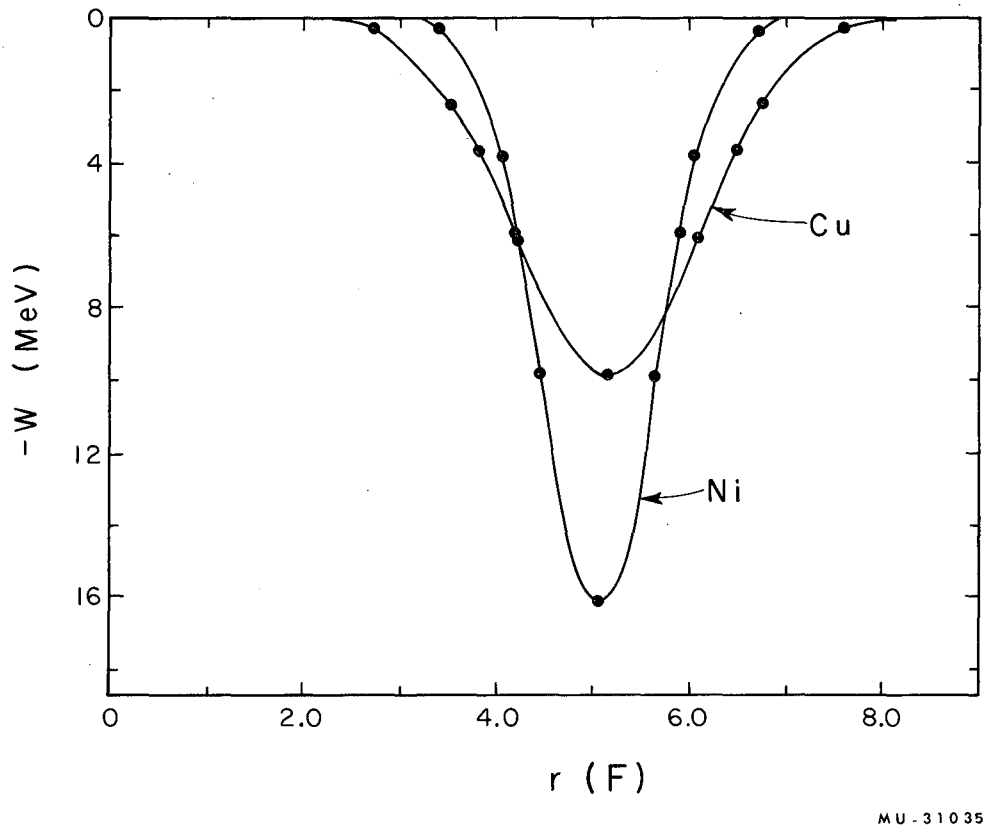

Fig. 39. Comparison of the best-fit imaginary optical-model potential obtained for 9.85-MeV protons on Ni and 10.20-MeV protons on Cu^{63}. The parameters are listed in Table XI.

σ_R for Ni could probably be realized if one assumed a distribution other than isotropic for σ_{CE}, but the arbitrary nature of this precluded further investigation. Further work may help one to correlate given parameter fluctuations with known structural features.

3. Silver

Figure 40 shows the results obtained from GULLEY by using both volume and surface absorption for the imaginary potential. This figure shows a plot of χ^2 vs b for given values of r_o where the numbers in parenthesis are the predictions of σ_R. The experimental value of $\sigma_R - \sigma_{CE}$ is 700 ± 60mb. Hintz's data were used for $\sigma_{el}(\theta)$.[50] The results are not quite as clear-cut as in the previous cases. Surface absorption gives a considerably better fit to $\sigma_{el}(\theta)$ than does volume absorption. If one looks at the minima in the χ^2 cuves in Fig. 40, volume absorption is seen to give a somewhat better prediction of σ_R. However, the χ^2 curve is very flat for surface absorption when $r_o = 1.25$ F, and one can reach the proper value of σ_R with very little increase in χ^2. The fit at this point is still appreciably better for $\sigma_{el}(\theta)$ than for any fit using volume absorption. Table XII lists some fits with different values of r_o. Figure 41 shows a plot of σ/σ_{Ruth} vs $\theta_{c.m.}$, where the solid line is a typical fit using surface absorption.

4. Aluminum

Aluminum presents a situation similar to that of Ni. Analysis for 9.85-MeV protons on Al with the use of volume absorption is completely unable to give an adequate amount of $\sigma_{SE}(\theta)$ in the backward angles. Surface absorption, on the other hand, is able to fit the backward angles very well albeit the forward angles are not fitted so well (see Fig. 42). Some improvement can be gained with the fit to the forward angles only by ingnoring the backward angles altogether. Table XIII presents the best fits for different r_o values. The optical-model predictions were fitted to Hintz's data for 9.85-MeV protons on Al.[50] The experimental value of $\sigma_R - \sigma_{CE}$ reported in this work is 660 ± 30mb.

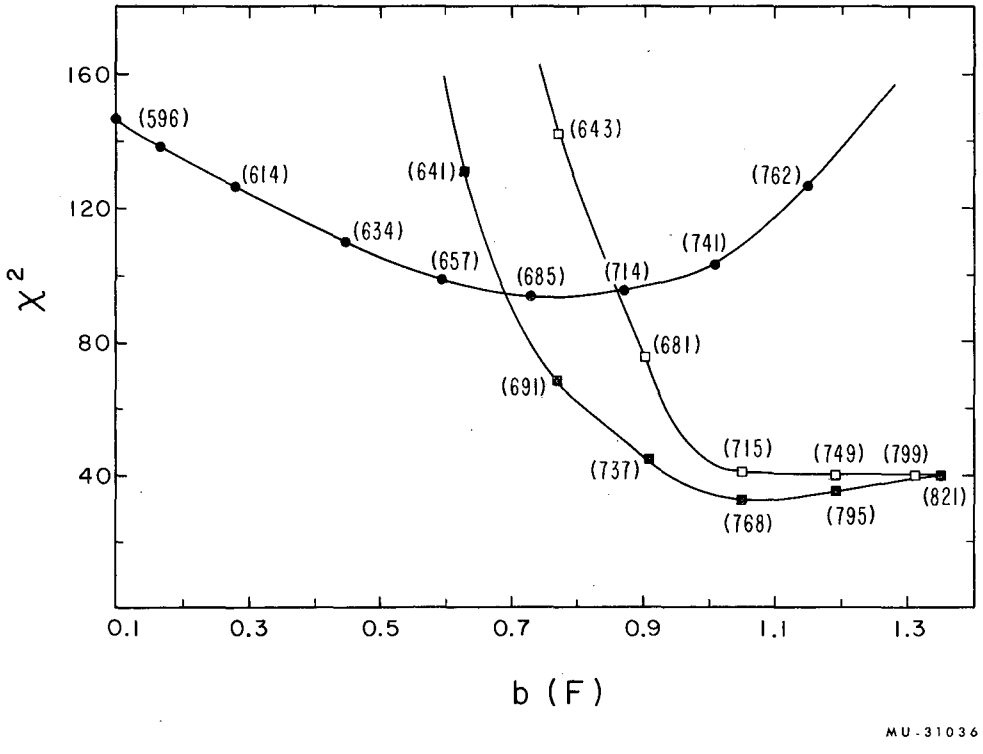

Fig. 40. A plot of χ^2 vs b for 9.79-MeV protons on Ag. The symbol ● represents volume absorption, and r_o = 1.30 F; the symbol ■ represents surface absorption, and r_o = 1.30 F; and the symbol □ represents surface absorption, and r_o = 1.25 F. The parameters V, a, and W were adjusted to minimize χ^2 at each point. The number in the parenthesis refers to the predicted σ_R in mb.

Table XII. Sets of "best fit" parameters for 9.79-MeV protons on Ag at different values of r_o; $r_o = r_W$.

Form Factor	r_o (F)	b (F)	a (F)	-V (MeV)	-W (MeV)	χ^2	σ_R (mb)
Volume	1.25	0.87	0.579	55.5	8.5	102	666
Volume	1.30	0.77	0.567	50.9	8.4	90	690
Volume	1.35	0.66	0.553	46.8	8.3	88	715
Surface	1.25	1.05	0.736	52.7	12.7	41	715
Surface	1.30	0.84	0.745	48.6	18.5	55	717

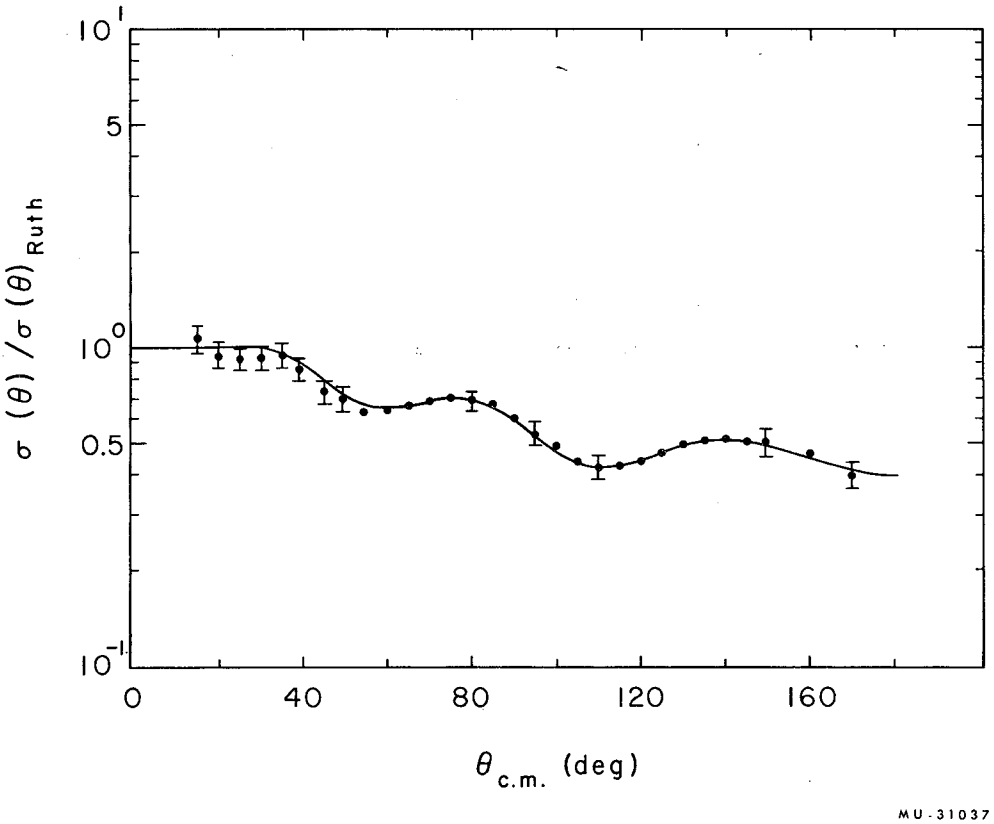

Fig. 41. A plot of σ/σ_{Ruth} is shown for 9.79-MeV protons on Ag. The solid line is the predicted value of σ/σ_{Ruth} obtained by using surface absorption. The optical-model parameters for this fit are listed in Table XII at surface r_o = 1.25 F. The dots are the experimental points of Hintz.[50]

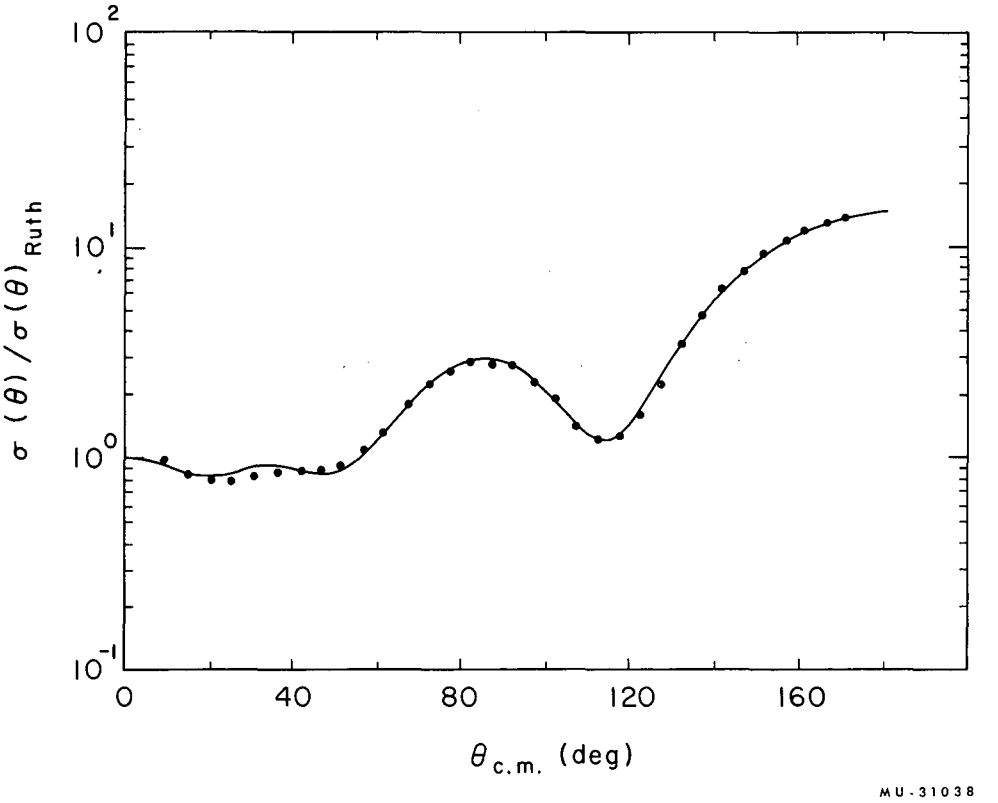

Fig. 42. A plot of σ/σ_{Ruth} is shown for 9.85-MeV protons on Al. The solid line is the predicted value of σ/σ_{Ruth} by using surface absorption. The optical-model parameters for this fit are listed in Table XIII at $r_0 = 1.50$ F. The dots are the experimental points of Hintz.[50]

Table XIII. Sets of "best fit" parameters for 9.85-MeV proton on Al at different values of r_o by using surface absorption; $r_o = r_W$.

r_o (F)	b (F)	a (F)	-V (MeV)	-W (MeV)	χ^2	σ_R (mb)
1.30	0.37	0.512	46.9	33.4	65	557
1.35	0.37	0.503	43.8	34.3	45	572
1.40	0.30	0.550	40.5	41.6	50	595
1.45	0.30	0.564	37.8	42.0	40	627
1.50	0.30	0.590	35.4	46.1	29	663

5. Overall picture

The four cases analyzed--i.e., 10-MeV protons on Cu, Ni, Ag, and Al--present a strong point in favor of the Gaussian shape (surface absorption) for the imaginary potential. Not only does the surface absorption fit the experimental $\sigma_{el}(\theta)$ better than volume absorption, but it also predicts the correct values of σ_R. Volume absorption was never able to fit both σ_R and $\sigma_{SE}(\theta)$. Table XIV lists the "best fit" set of parameters for each nucleus studied. The parameters are seen to show some systematic variation as a function of A, especially for the real part of the potential.

Figure 43 shows a plot of the experimental $\sigma_R - \sigma_{CE}$ vs A together with the range of σ_R predicted by the optical model with the use of both surface and volume absorption. The range was determined arbitrarily by accepting any value of σ_R provided the corresponding value of χ^2 was within a factor of 2 of its minimum. For those cases in which volume absorption was unable to give any good fit to $\sigma_{el}(\theta)$ data, a value of σ_R is used that corresponds to the best fit obtained.

F. Discussion of Alpha-Particle Results

The experimental values of $\sigma_R - \sigma_{CE}$ for 40.0 ± 2-MeV alpha particles are plotted in Fig. 44. The outstanding feature of the results is the appearance of a minimum in $\sigma_R - \sigma_{CE}$ in the region of Ni. This minimum, which also appears in the proton $(\sigma_R - \sigma_{CE})$ results (see preceding section), is certainly due to σ_R, because σ_{CE} for 40-MeV alphas should be negligibly small. Interpretation of this minimum will, of course, be similar to that for the proton measurement. It would be interesting to carry out an optical-model analysis for 40-MeV alphas on Cu and Ni to see if the experimental results could be fitted and if any conclusions drawn in the proton case would be applicable for this system.

Table XIV. Comparison of the "best fit" set of parameters obtained for approx 10-MeV protons on Cu, Ni, Ag, and Al. Surface absorption is used for all sets; $r_o = \bar{r}_W$.

Element	r_o (F)	b (F)	a (F)	-V (MeV)	-W (MeV)	σ_R (predicted) (mb)	$(\sigma_R - \sigma_{CE})_{exp.}$ (mb)
Al	1.50	0.30	0.590	35.4	46.1	663	656 ± 28
Ni	1.30	0.57	0.578	49.6	16.1	667	680 ± 30
Cu	1.29	0.93	0.623	49.3	9.9	853	840 ± 30
Ag	1.25	1.05	0.736	52.7	12.7	715	700 ± 60

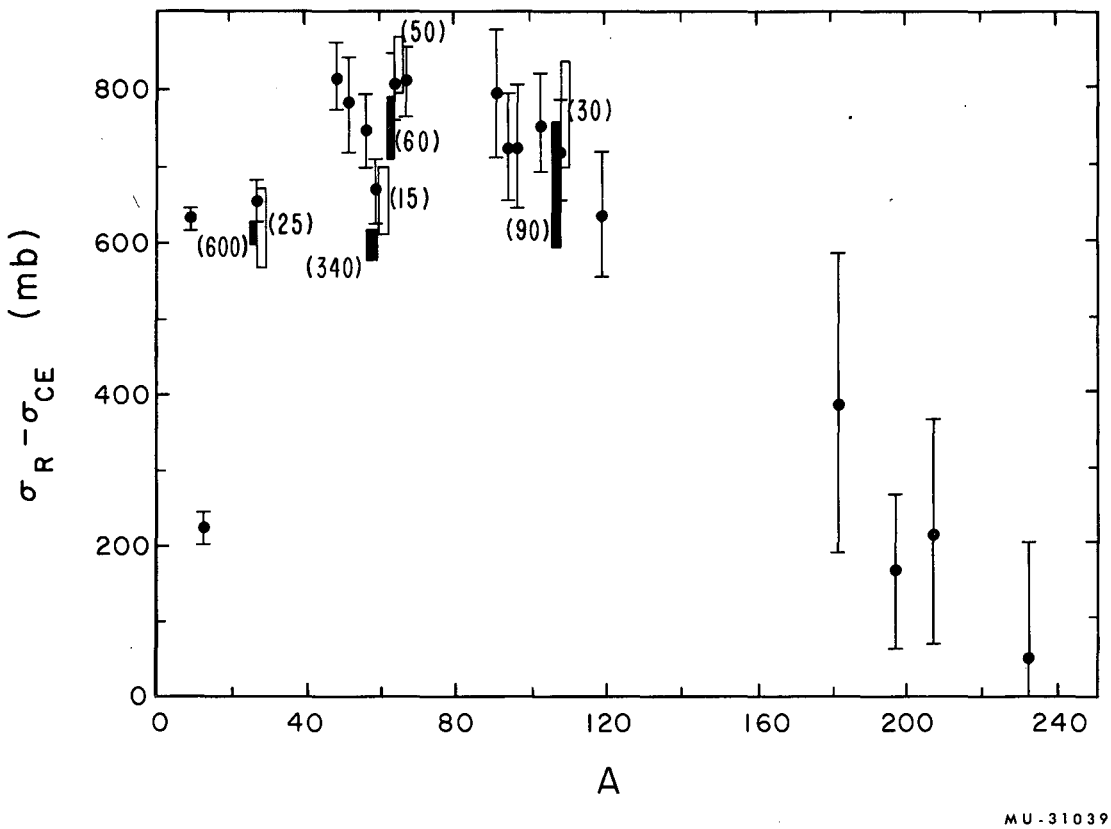

Fig. 43. Comparison between the experimental value of $\sigma_R - \sigma_{CE}$ for 10-MeV protons and the optical-model prediction of σ_R. The bar shows the range in σ_R one gets with surface absorption. The bar gives a similar range obtained by using volume absorption. The numbers in parentheses refer to the best χ^2 obtained with a particular potential shape. Different χ^2's should be related only when predictions on the same nucleus are being compared.

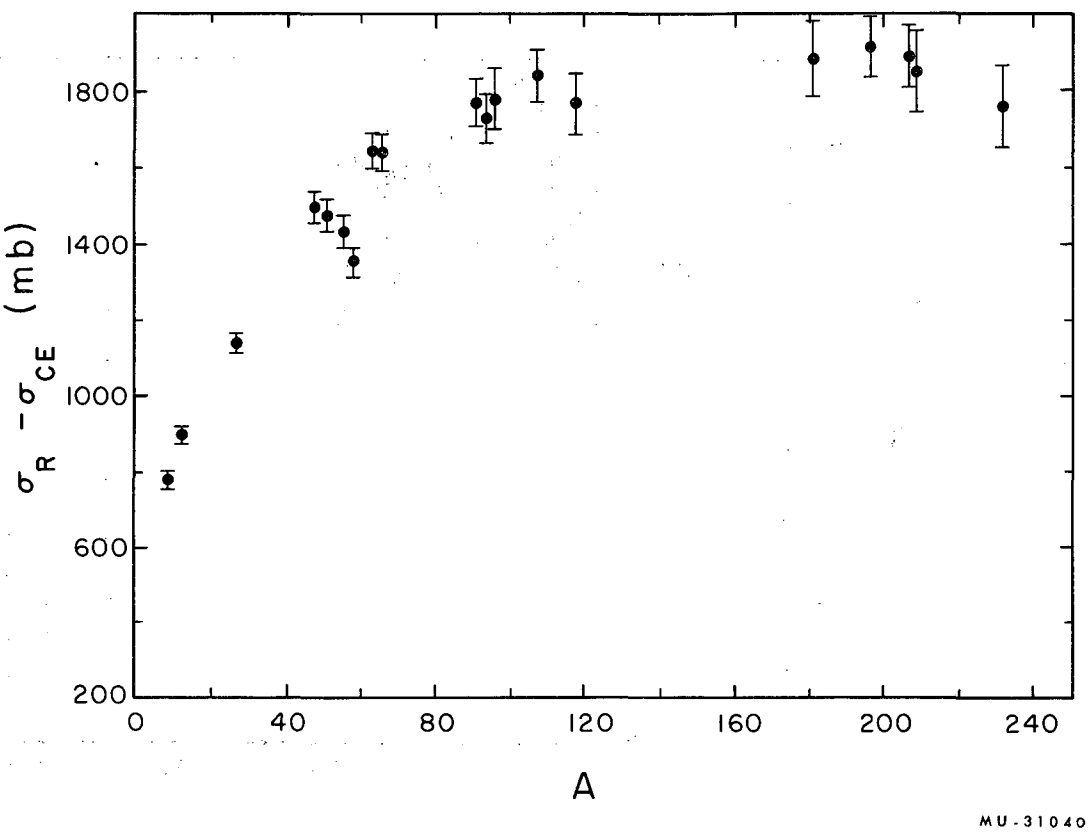

Fig. 44. The experimental results of σ_R-σ_{CE} obtained in this work for 40-MeV alpha particles plotted as a function of A.

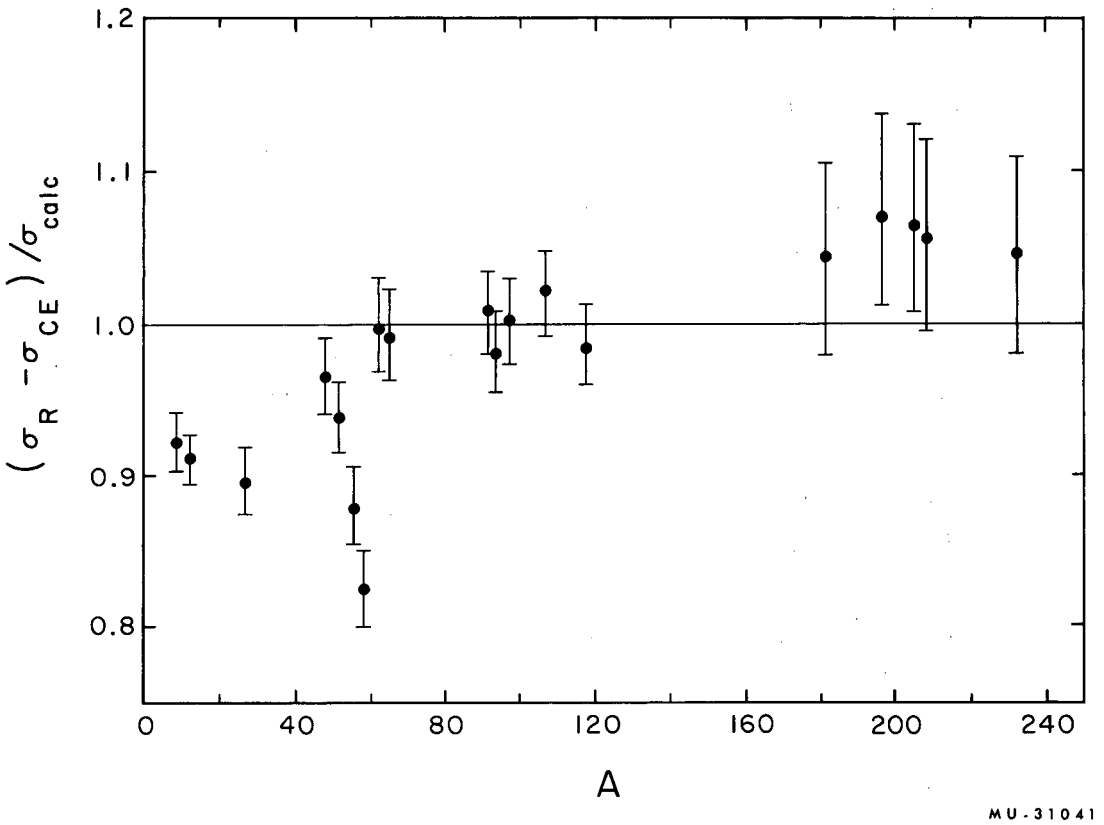

Fig. 45. Comparison between the experimental value of σ_R-σ_{CE} for 40-MeV alpha particles and σ_{calc}; the theoretical predictions of σ_R for 40-MeV alpha particles made by Huizenga and Igo,[81] as a function of A.

Total reaction cross sections have been predicted by Huizenga and Igo using a standard potential for all the nuclei.[81] The quantity $(\sigma_R - \sigma_{CE})_{exp}/\sigma_R$calc is plotted in Fig. 45. The minimum in the measured σ_R at Ni is very apparent in this plot. The remaining data vary systematically when they are compared with Huizenga and Igo's standard-potential calculation of σ_R. A slight correction to this potential can probably be made so that all the experimental values of σ_R can be fitted, with the exception of those nuclei that lie in the minimum near Ni.

There have been very few total reaction cross sections for alpha particles reported in the literature. No other beam-attenuation measurements for alphas have been made in this energy region. The summation of partial reactions has been carried out for many nuclei, but with 40-MeV alphas there are so many probable reactions that it is generally impossible to measure all the products. Excitation functions for alphas on Zn^{64}_{n}, measured by Porile, is perhpas one case for which most of the principal partial reactions have been measured.[65] His result of 1470 ± 150mb for σ_R at 40 MeV is in fair agreement with the value reported here. For high-Z materials for which almost the entire cross section is accounted for by fission, the results of Foreman et al. for alphas on Th^{232} are again in accord with the results reported here.[82]

G. Optical-Model Analysis of Alpha-Particle Results

Before any analysis could be carried out using GULLEY, a new χ^2 had to be defined. The elastic-scattering diffraction pattern for high-energy alpha particles scattered off nuclei is so complex that the definition of χ^2 used in the proton analysis (Eq. 18) was found inadequate. It was necessary to define an empirical χ^2 that gave priority to those characteristics of the diffraction pattern considered most important, e.g., position of maximum and minimum. The following equation was used:

$$\chi^2 = \sum_i \left(\frac{\left\{ [\sigma_i(\theta) + \sigma_{i+1}(\theta)]_{pred} - [\sigma_i(\theta) + \sigma_{i+1}(\theta)]_{exp} \right\}^2}{(\% \text{ error})\ \sigma_i(\theta)_{pred}\ \sigma_i(\theta)_{exp}} + \left\{ \frac{[\sigma_i(\theta) - \sigma_{i+1}(\theta)]_{pred} - [\sigma_i(\theta) - \sigma_{i+1}(\theta)]_{exp}}{[(\% \text{ error})\ \sigma_i(\theta)_{pred}\ \sigma_i(\theta)_{exp}]^{1/2}} \right\}^n \right), \quad (19)$$

where $n = 1$ when $\dfrac{[\sigma_i(\theta) - \sigma_{i+1}(\theta)]_{pred}}{[\sigma_i(\theta) - \sigma_{i+1}(\theta)]_{exp}} \geq 0$,

and where $n = 2$ when $\dfrac{[\sigma_i(\theta) - \sigma_{i+1}(\theta)]_{pred}}{[\sigma_i(\theta) - \sigma_{i+1}(\theta)]_{exp}} < 0$.

1. Carbon

An optical-model analysis of 48-MeV alpha particles scattered by C^{12} using GULLEY with the new definition of χ^2 was carried out. The analysis was fitted to the experimental $\sigma_{el}(\theta)$ data of Vaughn.[83] This analysis demonstrated that $\sigma_{el}(\theta)$ and σ_R data enable one to determine very accurately the extreme outer surface of both real and imaginary parts of the nuclear potential. This is a consequence of the alpha particle's having a very short mean-free path for absorption in nuclear matter. The alpha particle as such does not exist inside this extreme outer surface. Thus alpha-particle scattering and σ_R data can give no information on the nuclear potential lying inside the extreme outer surface of the nucleus. Igo, analyzing elastic-scattering data for alphas on several heavier nuclei, came to a similar conclusion concerning the shape of the real part of the optical-model potential at the surface of the nucleus.[84] Figures 46 and 47 show plots of the real and imaginary potential for several sets of parameters that gave good fits to the $\sigma_{el}(\theta)$, (see Table XV). Igo's standard potential is also

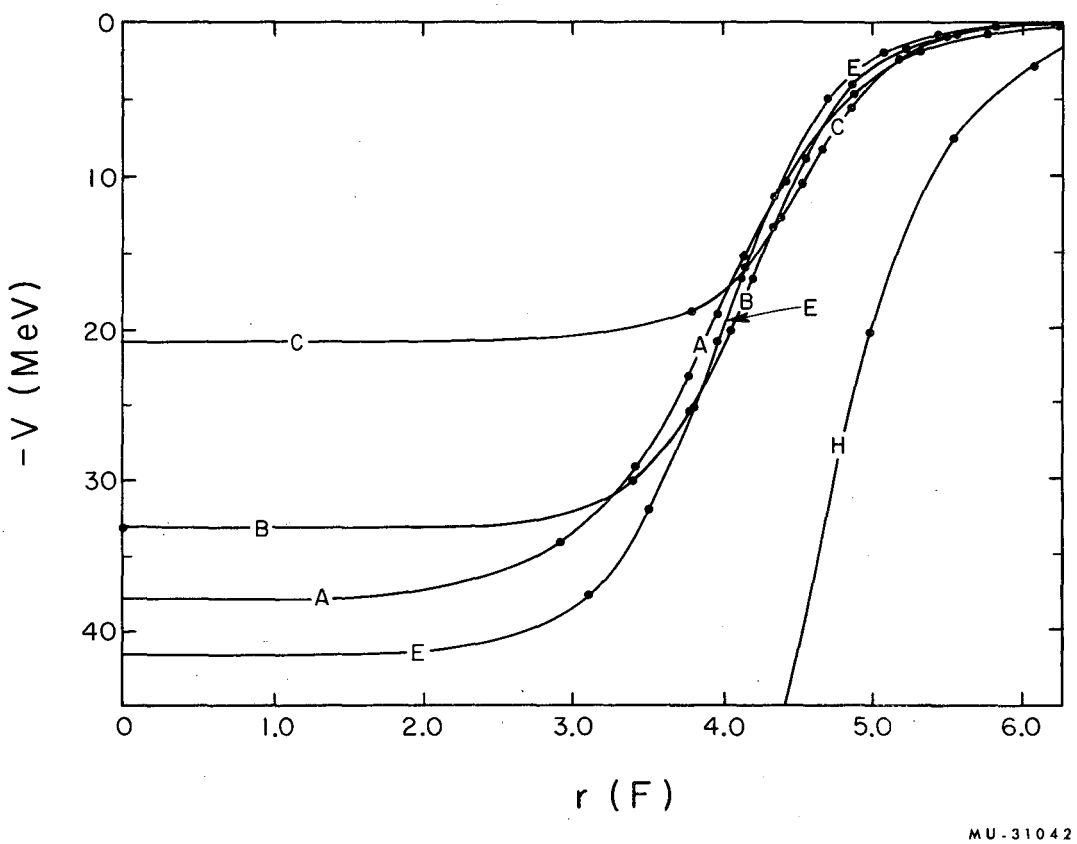

Fig. 46. Comparison of several real potentials that give good fits to $\sigma_{el}(\theta)$ for 48-MeV alpha particles on C^{12}. The letters in the graph refer to parameter sets listed in Table XV.

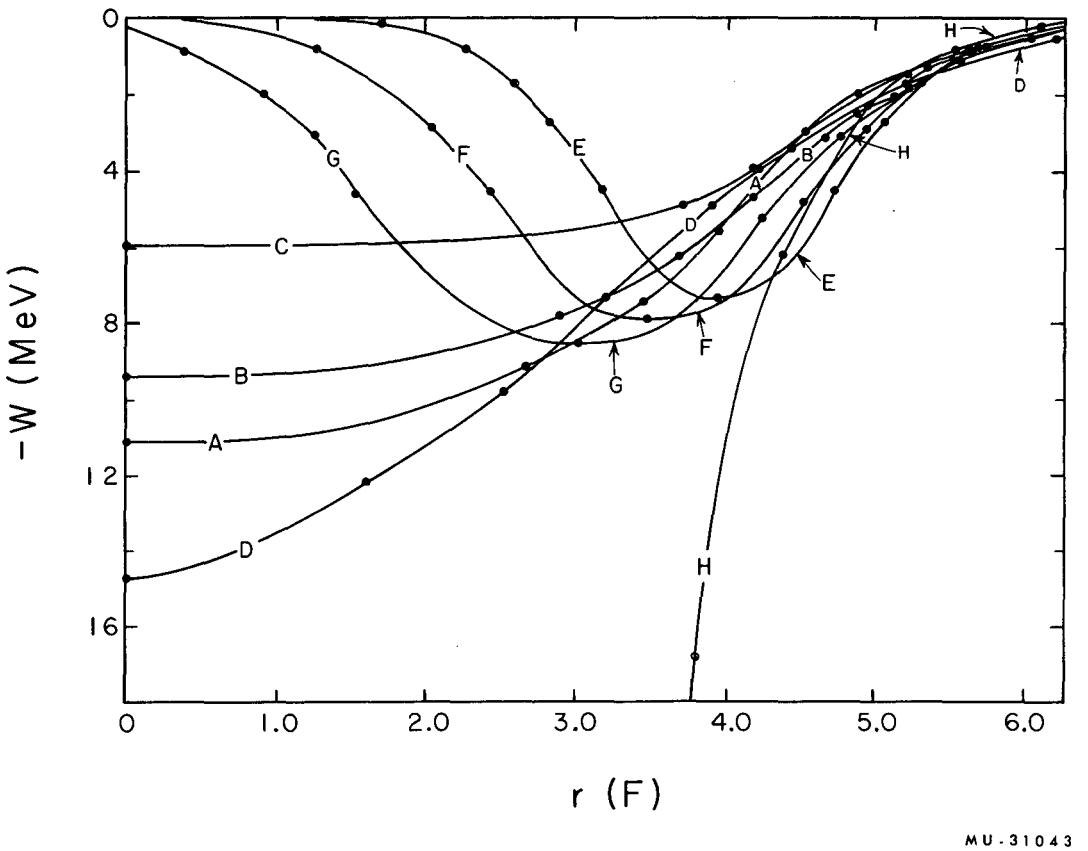

Fig. 47. Comparison of several imaginary potentials that give good fits to $\sigma_{el}(\theta)$ for 48-MeV alpha particles on C^{12}. The letters in the graph refer to parameter sets listed in Table XV.

Table XV. Sets of parameters that give good fits to $\sigma_{SE}(\theta)$ for 48-MeV alpha particles on C^{12}; r_1 = 1.20 F.

Curve	Form Factor	r_o (F)	r_W (F)	b (F)	a (F)	-V (MeV)	-W (MeV)	χ^2	σ_R (mb)
A	Volume	1.20	1.20	0.70	0.45	37.9	11.1	200	887
B	Volume	1.30	1.30	0.70	0.34	33.0	9.4	177	899
C	Volume	1.45	1.45	0.50	0.32	20.7	5.9	470	764
D	Volume	1.30	0.88	1.00	0.36	32.2	14.7	166	1001
E	Surface	1.20	1.20	0.80	0.37	41.5	7.3	274	770
F	Surface	1.20	1.00	1.00	0.385	40.8	7.9	220	795
G	Surface	1.20	0.80	1.20	0.40	40.1	8.5	180	822
H	Igo's standard potential.								

shown on Figs. 46 and 47 for comparative purposes. The large discrepancy between the results of this work and the Igo potential (see Fig. 46) is not unexpected if one considers the deviation from unity of the quantity $(\sigma_R - \sigma_{CE})_{exp}/\sigma_{calc}$ shown in Fig. 45. A comparison of the experimental and predicted values of σ/σ_{Ruth}, using parameter set B of Table XV, appears in Fig. 48. An experimental value of 901 ± 16mb obtained for 40-MeV α's on C^{12} compares favorably with the predicted value of σ_R for set B (see Table XV).

As seen in Fig. 47, it is meaningless to speak of the alpha-particle interaction in terms of a Gaussian shape or Woods-Saxon shape for the imaginary potential. It is necessary only to adjust the parameters of the potential until it matches a certain shape at the very edge of the nucleus. Figure 49 shows the imaginary potential at large values of R ($R = r_o A^{1/3} + r_1$). From this figure and Table XV it is easily seen that an accurate measurement of σ_R is a necessity in determining the shape of the imaginary potential. All the curves in Fig. 49 are about equally good fits to $\sigma_{el}(\theta)$. Figure 49 illustrates that a direct relationship exists between the strength of the imaginary potential and the predicted σ_R in the region of about 5.5 to 7.0. From this it can be implied that the alpha particle does not penetrate with any appreciable probability within about 5.2 F and still have any chance to escape as an elastic event; otherwise, the optical model, using potentials E, F, and G would be expected to predict a large σ_R. To check this result quantitatively,[85] calculations of the flux and divergence of the flux for the alpha particles inside the nucleus should be carried out in a manner similar to that of McCarthy.

Figure 50 shows a plot of the various "best fit" real potentials in this surface region. Proper adjustment of the parameters V, r_o, and a , which lead to the same shape potential beyond 5 F, gives almost equally good fits; this explains how the nonuniqueness of parameters arises from the use of a nuclear potential form factor by which one attempts to describe the interaction in a region that the alpha

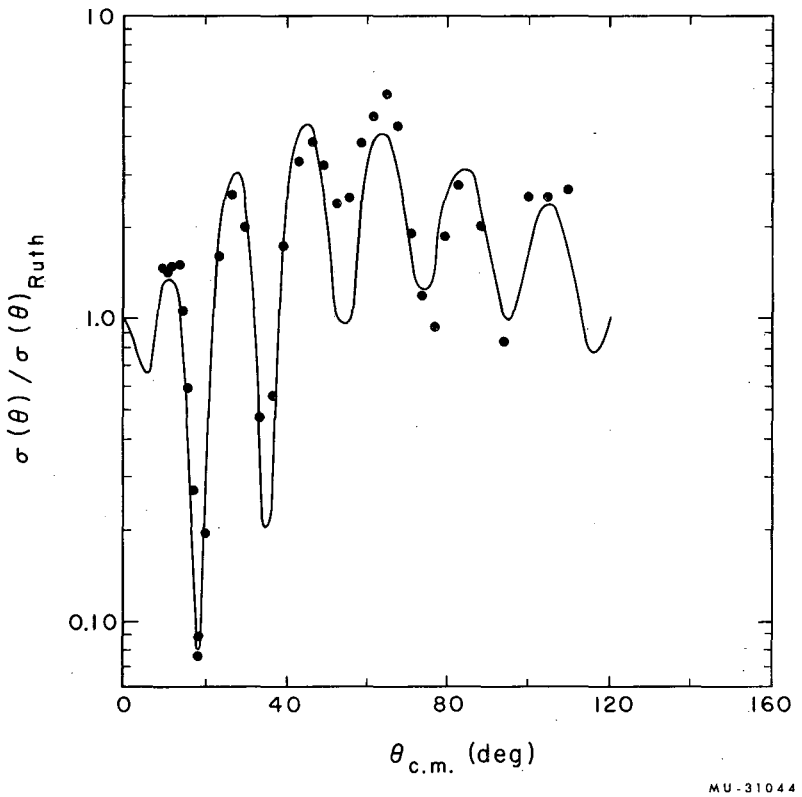

Fig. 48. A plot of σ/σ_{Ruth} is shown for 48-MeV alpha particles on C^{12}. The solid line is the predicted value of σ/σ_{Ruth}. The optical-model parameters for this fit are listed at B in Table XV. The dots are the experimental points of Vaughn.[83]

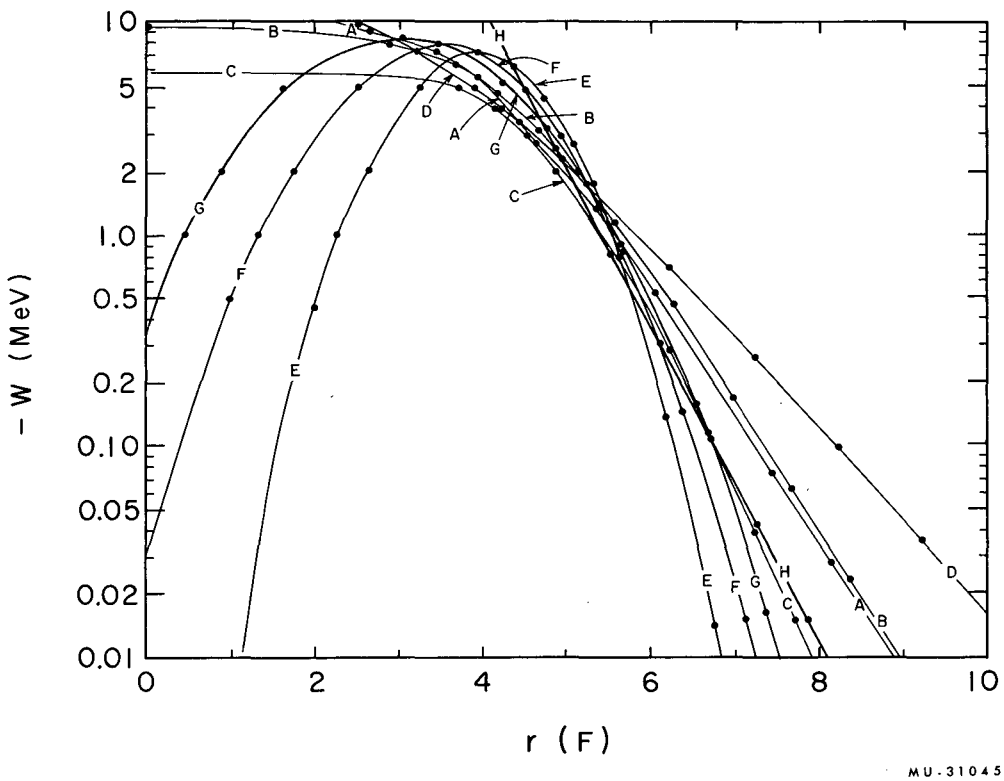

Fig. 49. Comparison of the imaginary potentials listed in Table XV at large values of r. The letters refer to the parameter sets listed in Table XV.

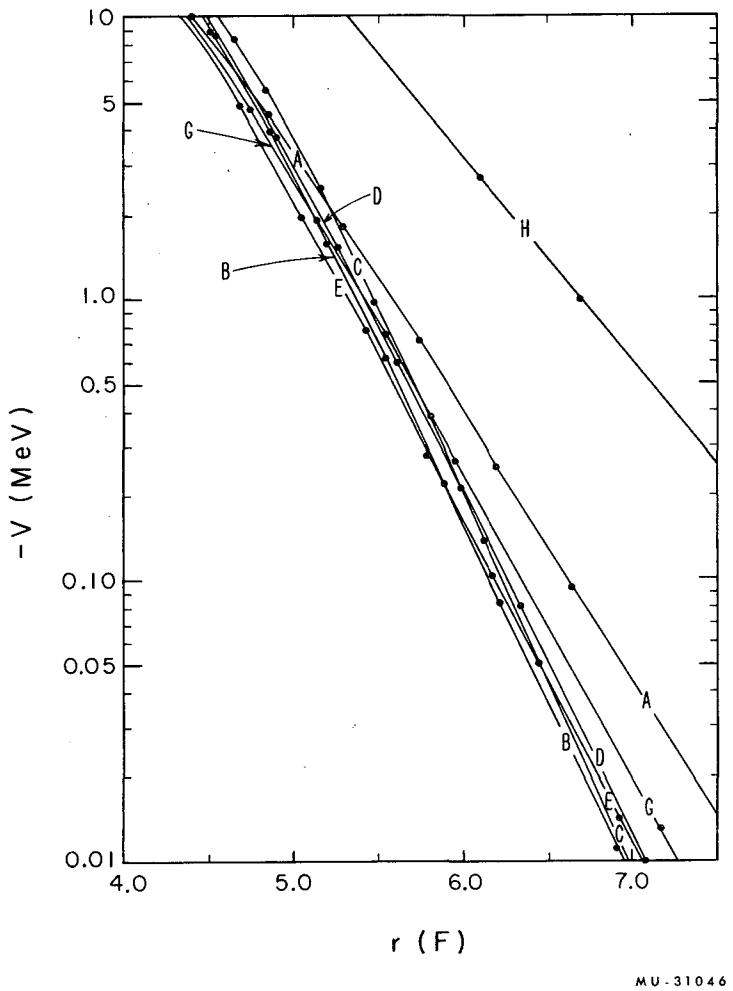

Fig. 50. Comparison of the real potentials listed in Table XV at large values of r. The letters refer to the parameter sets listed in Table XV.

particle does not sample. It should be noted that Igo's standard potential falls in a far different region. However, if any analogy can be drawn from the analysis on the more weakly interacting proton, discussed earlier, one should not expect to find a standard potential that fits all nuclei equally well. Igo's potential was determined from analysis on A, Cu, and Pb.[84]

2. Partial-Wave Cutoff Approximation

One of the principal difficulties involved in an optical-model analysis of alpha particles is the considerable amount of computer time necessary to carry out the parameter search. The time needed for a given calculation is proportional to $(\mathrm{LMAX})^2$, where LMAX is the total number of partial waves used in the calculation. A technique has been developed that saves considerable time in the preliminary searching. It involves the assumption that the amplitude of the lower outgoing partial waves is zero. This is a good assumption for the inner partial waves of a strongly interacting particle such as an alpha particle. Empirically it was found that little or no change occurred in the predicted $\sigma_{el}(\theta)$ if the transmission coefficient, defined as

$$T_\ell = 1 - |\exp[2i\,\delta_\ell]^2 ,$$

was greater than 0.995. Figure 51 shows a plot of $\sigma/\sigma_{\mathrm{Ruth}}$ for 40-MeV alphas on Cu for various values of LMIN, where LMIN is the lowest partial wave that has a nonzero value for the amplitude of the outgoing wave. The corresponding T_ℓ's are plotted in Fig. 52. The time needed for a given calculation becomes proportional to $(\mathrm{LMAX} - \mathrm{LMIN})^2$. This technique should have considerable merit for use in an optical-model analysis on heavy-ion scattering.

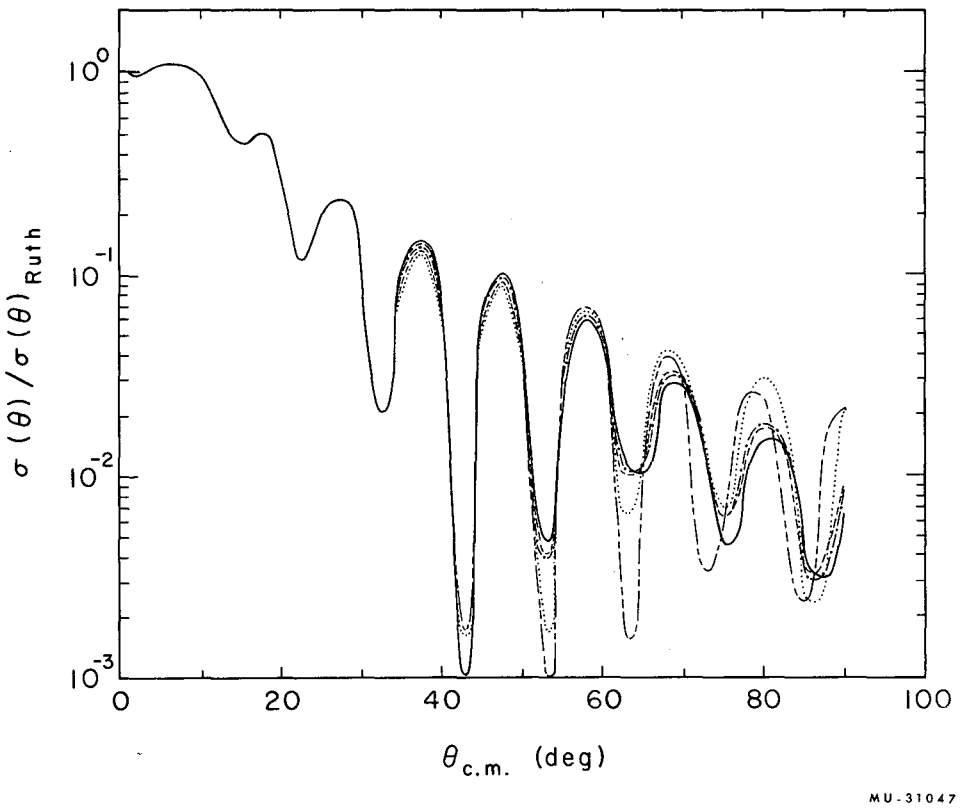

Fig. 51. Comparison of $\sigma(\theta)/\sigma(\theta)_{Ruth}$ for 40 MeV alpha particles on Cu using several values of LMIN; LMIN = 0 ———, LMIN = 13 ----
LMIN = 14 •-•- , LMIN = 15 •••••, LMIN = 16— – – —— – – —— .

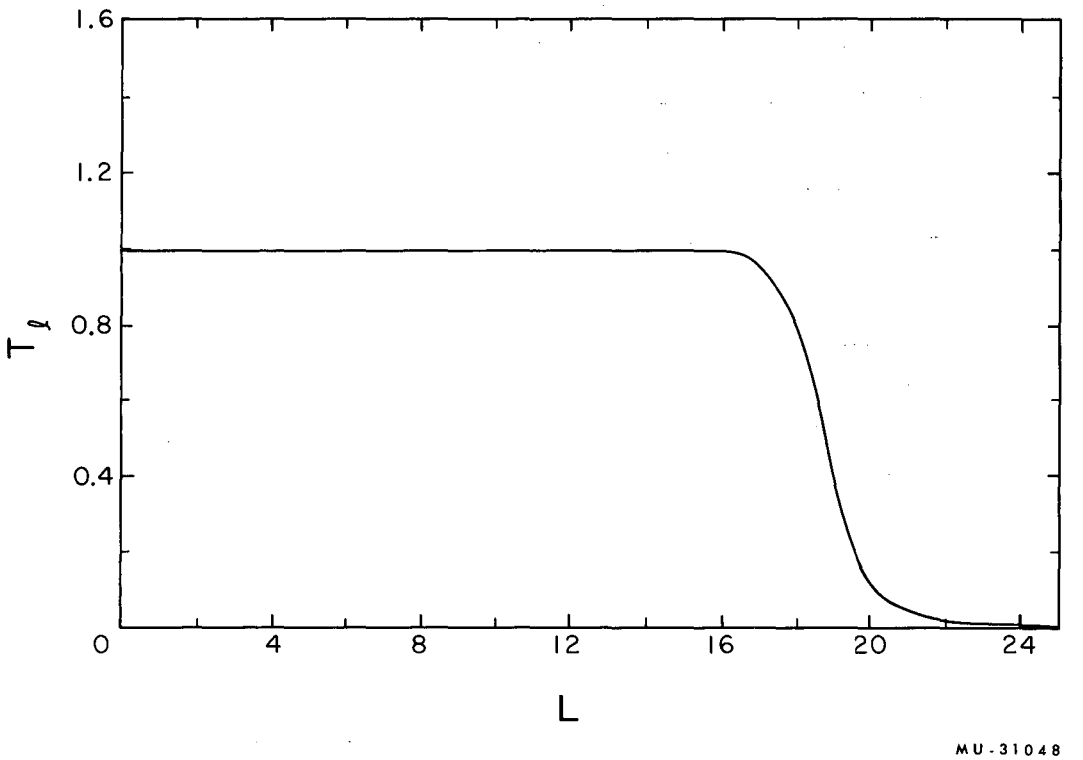

Fig. 52. The transmission coefficient T_ℓ plotted as a functions of the partial wave L for 40-MeV alpha particles scattered from Cu.

The results of this optical-model analysis for 48-MeV alpha particles elastically scattered from C^{12} point out the necessity for accurate measurement of σ_R so that the outer surface of the nuclear potential can be determined. Measurements of $\sigma_{el}(\theta)$ and σ_R as a function of energy, especially near the Coulomb barrier, where σ_R should be more sensitive to the surface shape of the potential, need to be made. Rasmussen has pointed out that accurate knowledge of the nuclear surface can give valuable insight into the problem of nuclear-deformation and alpha-decay systematics.[86] The results of this investigation also suggest that a careful analysis of this surface area should be carried out whereby the shape of the nuclear potential in this narrow, sensitive region can be varied systematically until an optimum fit is obtained. Phase-shift analyses indicate that one can find a given set of phase shifts that fit unambiguously the $\sigma_{el}(\theta)$ and σ_R data. In the case of strongly interacting particles such as an alpha particle, one may be able to go one step further and use the $\sigma_{el}(\theta)$ and σ_R data to determine unambiguously the shape of the nuclear potential in this sensitive surface region.

H. Discussion of Deuteron Results

The deuteron is known to be a relatively large loosely bound system subject to breakup processes at interaction distances larger than the nuclear radius.[55] It has not been shown conclusively whether this breakup process is due to an interaction with the Coulomb field or to an interaction with the nuclear forces at the extreme surface of the nucleus. Theoretical calculations have been made for the total electric-breakup and nuclear-breakup cross sections.[87,88] Hamburger, Cohen, and Price[55] have found that at about 15 MeV the deuteron breakup cross section is greater by about a factor of two than the predicted values for electric or nuclear breakup. If these breakup interactions

are due to processes that occur outside the nuclear-force field, then one would expect to see an enhancement of the deuteron total reaction cross section in comparison with σ_R for alpha particles that do not undergo this breakup process. If, on the other hand, these processes occur at the nuclear surface, where the deuteron interacts with the nuclear-force field, this breakup reaction might be expected to compete with the formation of the compound nucleus. In this case no enhancement of the total reaction cross section would be expected. Figure 53 lists the values of $\sigma_R - \sigma_{CE}$ for 22.4-MeV deuterons. A comparison of 22.4-MeV deuteron reaction cross sections with 40-MeV alpha particle reaction cross sections (see Fig. 44) shows them to be almost identical for all elements investigated. The comparison is valid since the Coulomb-barrier effects are almost identical in these two cases. The deuteron reaction cross sections are apparently not enhanced by the large magnitude of the breakup process (i.e., 400 to 650mb). This suggests that these processes occur by the nuclear-breakup mechanism. Another notable feature in Fig. 53 is the absence of the minimum in $\sigma_R - \sigma_{CE}$ in the region of Ni that was present in the alpha and proton σ_R measurements (see Figs. 44 and 23). A possible explanation can be given by assuming that the breakup process competes with the compound-nucleus formation. The deuteron interaction has two dominant modes that lead to a reaction event: compound-nucleus formation and breakup process. If the σ_{CN} is inhibited by structural factors in the nucleus--i.e., a closed proton shell at Ni--the reaction will proceed via the other channel, and σ_R will remain proportional to the nuclear size. If there is no other dominant mode, as in the case of alpha particles and protons, then a decrease in σ_R may occur.

Very few measurements of σ_R exist for deuterons near 20 MeV. Budzanowski and Grotowski have recently measured σ_R for Ni^{58} and Ni^{60} for 12.8-MeV deuterons.[89] They obtained values of 1523 ± 120mb for Ni^{60}, and 1589 ± 125mb for Ni^{58}. This method consisted of measuring the angular distribution of (d,q), where q is any charged particle, and

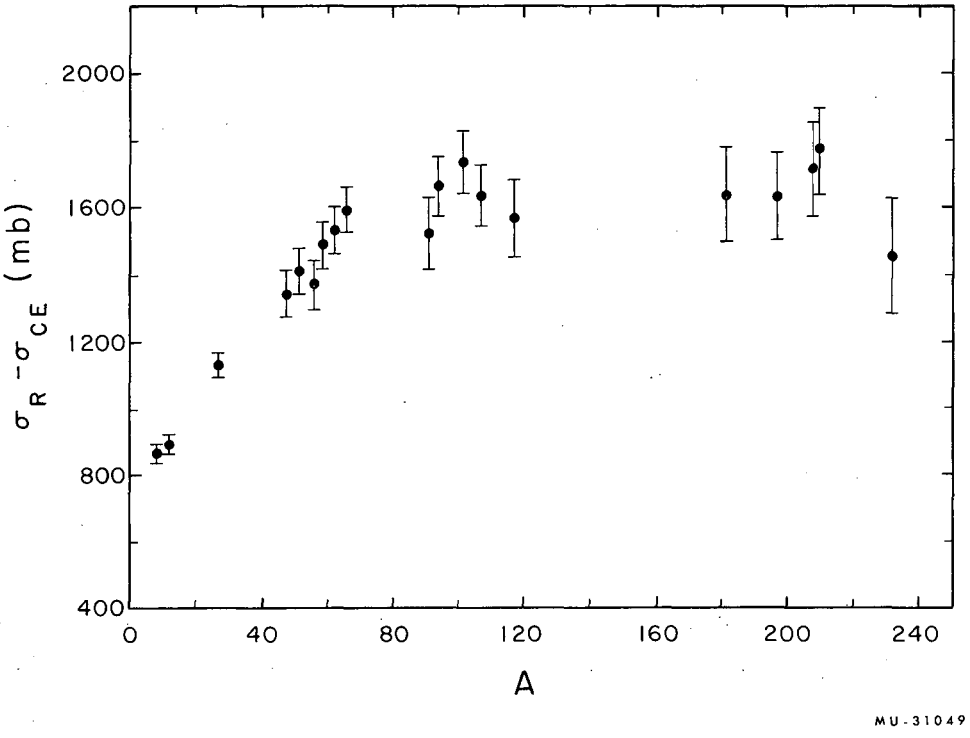

Fig. 53. The experimental results of σ_R-σ_{CE} obtained in this work for 22.4-MeV deuterons plotted as a function of A.

integrating over all the inelastic states. The (d,xn) reactions were measured by chemical separation techniques. It is not clear how (d,2p) events are properly accounted for by this method. Their results are higher than the value of 1491 ± 63mb reported here for 22.4-MeV deuterons when proper account is taken of the Coulomb-barrier effects.

The importance of having reaction cross section measurements for determining the deuteron optical-model parameters is again apparent. Halbert et al.[90] have obtained good fits to the comprehensive deuteron elastic-scattering data at 11.8 MeV. They obtain 2051mb and 2217mb for the predicted σ_R for Sn in two analyses.[91] The measured value at 22.4 MeV for Sn is two analyses.[91] The measured value at 22.4 MeV for Sn is 1563 ± 117mb (see Table IV). In the case of Ni the theoretical values of 1360 and 1396mb at 11.8 MeV, and the measured value of 1491 ± 63mb at 22.4 MeV are in better agreement. It should be noted that σ_R at 11.8 MeV will be lower than σ_R at 22.4 MeV, owing to Coulomb-barrier effects. Elastic-scattering data only are not sufficient to predict the correct value of σ_R. Conversely, the experimental values of σ_R are necessary data for deuteron optical-model analyses.

I. Future

Optical-model analyses indicate that the value of σ_R must be known to 1 to 2% before a specific set of optical-model potential parameters can be accurately determined. The technique used to measure σ_R in this work cannot give a measurement of this accuracy in a reasonable length of time. I wish to suggest an improvement in this technique that should help one to obtain a 1 to 2% measurement of σ_R.

The major source of difficulty in the charged-particle beam-attenuation technique has been the attenuation of the beam in the stopping counter or the energy degrader immediately in front. Construction of a "dual counter" should eliminate this problem. The dual counter

should consist of a central plastic scintillator and a surrounding semiconductor detector (see Fig. 54). The plastic scintillator should subtend an angle large enough to catch all the multiple scattered beam. This angle should be small enough to keep the inelastic correction negligible. The plastic scintillator (counter 5) is used as a yes-no counter and retains the fast rise and decay characteristics necessary for high count rates. The semiconductor detector catches the large-angle scattering and reaction events. This detector will receive a relatively low count rate and thus preserve good energy resolution. It would be gated by a $(1\ \bar{2}\ 3\ \bar{4}\ \bar{5})$ event. It is only necessary that θ_{SS} remain large enough so that the elastic correction be small (see Fig. 54). With this arrangement, the attenuation and its energy dependence in counter 5 can be neglected. Consequently, the "dummy foil" technique need not be used, i.e., η_3 correction is 0. The target-in — target-out ratio will improve by a large factor, so that 1% statistics can be obtained in a short time. The good energy resolution of the semiconductor detector will make σ_{in} correction very small. The major problem will lie in the construction of a reliable detector of this form. Other improvements concerning elimination of the scattering foil and time-of-flight criterion can be realized. In the next few years, many refinements in the general technique should occur.

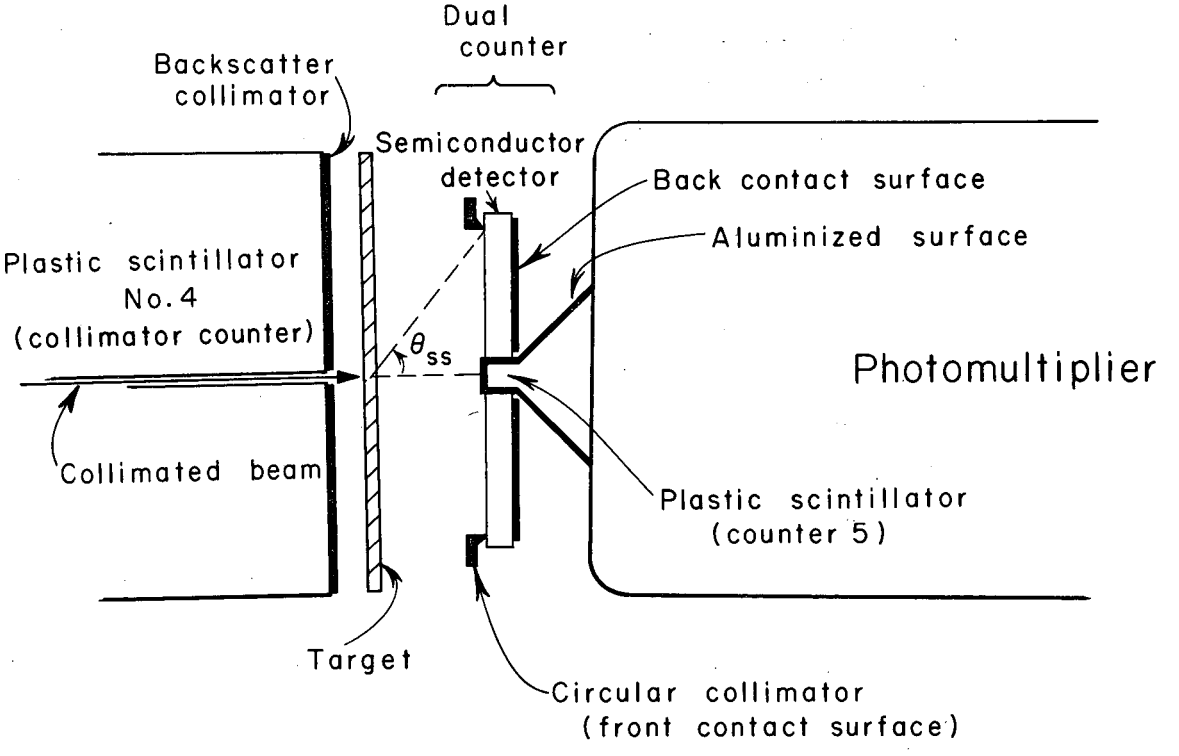

Fig. 54. Schematic diagram of the "dual counter" and the target area.

VII. SUMMARY

The adaptation of charged-particle beam-attenuation methods to millimicrosecond electronic techniques has permitted measurements of σ_R on many different nuclei.

Optical-model analyses carried out here and elsewhere emphasize the fact that knowledge of the quantity σ_R is necessary for any accurate determination of optical-model potential parameters.

The results of the proton total reaction cross section in conjunction with an optical-model analysis have shown that a surface peaking of the imaginary part of the optical potential is necessary to fit the proton experimental data.

The structure found in the quantity σ_R as one proceeds from nucleus to nucleus eliminates any hope that a single set of optical parameters would fit all nuclei. However, more accurate knowledge of this structure in σ_R, especially as a function of energy, should give valuable insight into the structure of nuclei.

The addition of alpha-particle reaction cross sections to the $\sigma_{el}(\theta)$ data puts a powerful constraint on the shape of the extreme surface of the optical potential. Careful analysis may yield information regarding nuclear deformations.

It is hoped that the techniques discussed here will prove useful as a guide for future measurements of σ_R.

ACKNOWLEDGMENTS

I wish to thank Dr. George Igo for his help, his guidance, and for the many stimulating discussions he provided during the course of this work.

It is a pleasure to thank also Dr. T. Darrah Thomas for suggesting this experiment and for his assistance during its early stages.

I am indebted to Dr. Homer E. Conzett for his many helpful discussions concerning the theoretical interpretation of the experimental results.

Special thanks are due to Mr. Richard Pehl for his invaluable assistance in carrying out the optical-model analyses.

For their many stimulating discussions concerning this experiment, I would like to thank Dr. Victor E. Viola, Dr. Joseph Cerny III, and Dr. James F. Mollenauer.

The help of Michiyuki Nakamura was invaluable in setting up the electronic circuitry and providing me with a practical knowledge of counting electronics.

For those many interesting hours spent disucssing science and the philosophy of life in general, I would like to thank Messrs. Richard Chanda, Paul Croft, Ernest Rivet, Richard Kiefer, and Dr. Lee Hyder, Dr. Ralph Korteling, and Dr. Paul Reeder.

The assistance of the 60-inch-cyclotron crew, headed by W. B. Jones, in providing a steady beam, was greatly appreciated.

I am grateful to Mr. Chuck Corum for his design of the experimental apparatus and to Mr. Dan O'Connell for the preparation of thin foils.

This work was performed under the auspices of the U. S. Atomic Energy Commission.

APPENDIX

A. FORTRAN listing of the optical-model search-routine GULLEY

```
C       GULLEY 3 MAIN ROUTINE TO MINIMIZE A FUNCTION                    A.1
C       WRITTEN BY B. WILKINS AND R. PEHL
        DIMENSION X(10),WT(10),G(10),EXVEC(10),XC(10),GB(10),       XB(10)
        DIMENSION DINC(10),S(10),            XMIN(10),       XD(10),V(10)
       X   ,BB(10),D0(10),D1(10),D2(10),XBS(10)
      1 READ INPUT TAPE 2,120,NPAR,NSTEP,LMAX,LMIN,IPLOT,DEL,STEP
    120 FORMAT (5I10,2F10.5)
        READ INPUT TAPE 2,520,(X(I),I=1,10)
    520 FORMAT (4F10.6,F8.5,2F6.4,2F5.3,I2)
        READ INPUT TAPE 2,130,(WT(I),I=1,NPAR)
    130 FORMAT (7F10.5)
        WRITE OUTPUT TAPE 3,130,(WT(I),I=1,NPAR)
        NFCN = 0
        NRAT = -1
        MSTEP = -1
        WTS = WT(2)
        DMAX = LMAX
        NPARS = NPAR
        NPART = NPAR + 1
        DO 15 I = NPART,10
        XB(I) = X(I)
        XC(I) = X(I)
        XD(I) = X(I)
     15 BB(I) = X(I)
        IF (STEP) 500,20,20
     20 NPAR = NPAR - 1
        DO 200 I = 1,NPAR
        D0(I) = X(I)
        D1(I) = X(I)
    200 D2(I) = X(I)
        IF (NSTEP - 1)210,210,205
    205 CALL DIFFER (NPARS,G,F,X,DINC,NPAR,IPLOT,NSTEP,LMAX,LMIN)
    210 JPLOT = IPLOT - 1
        KPLOT = IPLOT - 2
        X(NPARS) = X(NPARS) + WT(NPARS)
    212 WT(2) = WTS*X(2)
        DO 214 I=1,NPAR
    214 DINC(I) = 0.01*ABSF(WT(I))
        CALL DIFFER (NPARS,G,F,X,DINC,NPAR,KPLOT,MSTEP,LMAX,LMIN)
        GNORM = 0.0
        DO 209 I =1,NPAR
    209 GNORM = GNORM + ABSF(G(I)/WT(I))
        GNORM = GNORM + .2
    215 WRITE OUTPUT TAPE 3,435,F,(X(I),I=1,NPARS ),(G(I), I=1,NPAR )
    219 DO 220 I = 1,NPAR
    220 EXVEC(I) = -G(I)/(GNORM*WT(I))
        DO 228 I =1,NPAR
        IF (EXVEC(I)) 223,223,224
    223 S(I) = -1.
        GO TO 225
    224 S(I) = 1.
    225 EXVEC(I) = ABSF(EXVEC(I))
    226 EXVEC(I) = SQRTF(EXVEC(I))
    228 EXVEC(I) = S(I)*EXVEC(I)
        WRITE OUTPUT TAPE 3,435,(EXVEC(I),I=1,NPAR),GNORM
        GO TO 320
    315 DO 316 I = 1,NPAR
        V(I) = 1. + ABSF(GB(I)/G(I))
    318 IF(V(I) - 10.)321,321,319
```

A.2

```
  319 V(I) = 10.
  321 IF(GB(I)/G(I))317,317,322
  317 XC(I) = (XB(I) - X(I))*(2. - V(I)) + X(I)
      GO TO 316
  322 XC(I) = (XB(I) - X(I))*V(I)*1.4 + X(I)
  316 CONTINUE
      XC(NPARS) = XB(NPARS)
      GO TO 334
  320 DO 330 I =1,NPAR
  330 XB(I) = X(I) +       EXVEC(I)*NT(I)
      XB(NPARS) = X(NPARS)
  331 CALL DIFFER (NPARS,GB,FB,XB,DINC,NPAR,KPLOT,NSTEP,LMAX,LMIN)
  333 WRITE OUTPUT TAPE 3,435,FB,(XB(I),I=1,NPARS ),(GB(I),I=1,NPAR )
      GO TO 315
  334 CALL DIFFER (NPARS,GC,FC,XC,DINC,NPAR,KPLOT,NSTEP,LMAX,LMIN)
      WRITE OUTPUT TAPE 3,435,FC,(XC(I),I=1,NPARS ),(V (I),I=1,NPAR )
  336 RAT = (FB/FC)**2
      DO 340 I=1,NPAR
  340 XD(I) = XB(I) + (XC(I) - XB(I))*RAT/(1.+RAT)
      XD(NPARS) = XB(NPARS)
  345 CALL DIFFER (NPARS,GD,FD,XD,DINC,NPAR,IPLOT,NSTEP,LMAX,LMIN)
  435 FORMAT (1P10E12.4)
      IF(F -FB)347,349,349
  347 DO 348 I = 1,NPAR
  348 XB(I) = X(I)
      FB = F
  349 IF (FD - FC)350,352,352
  350 IF (FD - FB)355,365,365
  352 IF (FC - FB)360,365,365
  355 DO 356 I = 1,NPAR
  356 XMIN(I) =  XD(I)
      GO TO 369
  360 IF(FD/FC - 1.02)358,358,359
  358 NRAT = 1
  359 IF(NRAT) 362,362,363
  363 DO 364 I = 1,NPAR
  364 XMIN(I) = XC(I)
      GO TO 369
  365 IF(FD/FB-1.02)383,383,384
  383 NRAT = 1
  384 IF(NRAT) 372,381,381
  381 DO 382 I = 1,NPAR
  382 XMIN(I) = XB(I)
      GO TO 369
  372 DO 373 I = 1,NPAR
  373 XC(I) = 2.*XB(I) - XC(I)
      GO TO 374
  362 DO 361 I = 1,NPAR
      XBS(I) = XB(I)
  361 XB(I) = XC(I)
      FB = FC
  371 DO 366 I = 1,NPAR
  366 XC(I) = 2.*XB(I) - XBS(I)
  374 WRITE OUTPUT TAPE 3,367
  367 FORMAT (12H   RAT RERUN)
  368 NRAT = NRAT + 1
      GO TO 334
  369 IF (NSTEP - 1)1,1,370
```

```
      370 DO 380 I = 1,NPAR                                          A.3
          D0(I) = D1(I)
          D1(I) = D2(I)
          D2(I) = XMIN(I)
          BB(I) = (D2(I) + D1(I))/2. + ((D1(I) - D0(I))-(D2(I)-D1(I)))/6.
      380 X(I) = 2.*D2(I) -D1(I)+ ((D2(I)-D1(I)) - (D1(I)-D0(I)))/1.5
          BB(NPARS) = X(NPARS) - WT(NPARS)
          CALL DIFFER (NPARS,GD,FD,BB,DINC,NPAR,JPLOT,NSTEP,LMAX,LMIN)
          X(NPARS) = X(NPARS) + 2.*WT(NPARS)
          NRAT = -1
          NFCN = NFCN + 1
          DMAX = DMAX + DEL
          LMAX = DMAX + .5
          IF (NSTEP-NFCN)1,1,212
      500 STEP = 1.0
          NCYN = 1
          WT(2) = WTS*X(2)
      530 DO 532 I = 1,NPAR
      532 DINC(I) = 0.01*ABSF(WT(I))
          CALL DIFFER (NPARS,G,F,X,DINC,NPAR,IPLOT,MSTEP,LMAX,LMIN)
      534 GNORM = 0.0
          DO 521 I = 1,NPAR
      521 GNORM = GNORM + ABSF(G(I)/WT(I))
          GNORM = GNORM + .2
      535 WRITE OUTPUT TAPE 3,435,F,(X(I),I=1,NPARS ),(G(I), I=1,NPAR)
      540 DO 541 I = 1,NPAR
      541 EXVEC(I) = -G(I)/(GNORM*WT(I))
          DO 548 I =1,NPAR
          IF (EXVEC(I)) 543,543,544
      543 S(I) = -1.
          GO TO 545
      544 S(I) = 1.
      545 EXVEC(I) = ABSF(EXVEC(I))
      546 EXVEC(I) = SQRTF(EXVEC(I))
      548 EXVEC(I) = S(I)*EXVEC(I)
          WRITE OUTPUT TAPE 3,435,(EXVEC(I),I=1,NPAR),GNORM
      569 DO 570 I = 1,NPAR
          XB(I)= X(I) +       EXVEC(I) * WT(I)
      570 GB(I) = G(I)
          IF(NSTEP- NCYN)572,572,571
      572 CALL DIFFER (NPARS,GB,FB,XB,DINC,NPAR,IPLOT,NSTEP,LMAX,LMIN)
          GO TO 999
      571 CALL DIFFER (NPARS,GB,FB,XB,DINC,NPAR,IPLOT,MSTEP,LMAX,LMIN)
      573 WRITE OUTPUT TAPE 3,435,FB,(XB(I),I=1,NPARS ),(GB(I),I=1,NPAR)
      580 DO 590 I = 1,NPAR
          IF(GB(I)/G(I))585,585,590
      585 WT(I) = WT(I)/2.
      590 CONTINUE
      605 DO 610 I = 1,NPAR
          X(I) = XB(I)
      610 G(I) = GB(I)
      620 NCYN = NCYN + 1
          GO TO 534
      999 CALL EXIT
          END
```

```
      SUBROUTINE DIFFER (NPARS,G,F,X,DINC,NPAR,IPLOT,NOW,MAX,MIN)  A.4
      DIMENSION G(10),X(10),DINC(10),GF(10),XT(10),WT(10)
C     THIS SUBROUTINE COMPUTES THE DERIVATIVE VECTOR G(I) BY TAKING
C     FINITE DIFFERANCES - - POINTS ARE CALCULATED TO THE ALGEBRAICLY
C     LARGER SIDE OF THE CENTRAL VALUE , SO THAT THE DERIVATIVE IS NOT
C     CALCULATED SYMMETRICALLY
      DO 20 I = 1,10
   20 XT(I)=X(I)
      CALL ELAS(IPLOT,MAX,MIN,X,CHIT)
      F= CHIT
      IF(NOW)25,25,110
   25 JPLOT = 0
      DO 100 I = 1,NPAR
      XT(I)=X(I) + DINC(I)
      CALL ELAS(JPLOT,MAX,MIN,XT,CHIT)
      FD = CHIT
      XT(I)=X(I)
  100 G(I)=(FD-F )/F
  110 RETURN
      END
```

B. FORTRAN listings of subroutines DIFFER and ELAS written by Dr. N. K. Glendenning and modified by B. Wilkins and R. Pehl for use in search-routine analyses

```
      SUBROUTINE ELAS(IPLOT,MAX,MIN,X,CHIT)                          B.1
C     ELASTIC SCATTERING        N K GLENDENNING
      DIMENSION  CR(100),CI(100),SIG(100),TH(180),CRSX(183),RUTH(183),
     X  RELA(183)
     X  ,RAD(180),CO(180),SO(180),GO(180),ASL(100,90)
     X  ,PHIR(100),PHII(100)
     X  ,CHI(100),DATA(100),WTS(100),X(10),          CHIS(100)
C
C          NOTATION
C          H1,H2        =    INTEGRATIONSTEPS,H1 FOR FIRST 20 STEPS
C          RMAX         =    MATCHING RADIUS
C          DTHET        =    ANGLE INCREMENT
C          ELAB         =    LAB ENERGY OF PROJECTILE
C          CMP          =    PROJECTILE MASS IN AMU
C          CMT          =    TARGET MASS IN AMU
C          ZZP          =    PRODUCT OF CHARGES
C          MAX          =    MAXIMUM L WAVE COMPUTED
C          VR           =    REAL WELL DEPTH
C          VI           =    IMAGINARY WELL DEPTH
C          R0           =    RADIUS PARAMETER MULTIPLYING A**1/3
C          R1           =    PROJECTILE RADIUS
C                            TOTAL RADIUS = R0 * A**1/3 + R1
C                            COULOMB RADIUS = R0 * A**1/3
C          A0           =    SURFACE THICKNESS OF REAL WELL
C          B0           =    SURFACE THICKNESS OF IMAGINARY WELL
C          ALPHA        =    IF = 0 THEN PURE SAXON IMAGINARY WELL
C                            IF = 1 THEN PURE GAUSSIAN SURFACE WELL
C                            IF = BETWEEN THEN LINEAR MIXTURE
C          BETA         =    IF = 0 THEN RW = R0
C                            IF = 1 THEN RW DIFFERENT FROM R0
C          MODE         =    IF POSITIVE DATA IN FM/STER
C                            IF ZERO OR NEGATIVE THEN DATA/RUTH
C          IPLOT        =    0  NO PLOT
C                            1  PLOTS START,D
C                            2  PLOTS START,D,BB
C                            3  PLOTS START,D,BB,A,B,C,RAT RERUN
C
      IF (NUFF - 37) 111,524,111
  111 NUFF = 37
    1 READ INPUT TAPE 2,490,CHECK,KIN,KEND,MODE,(DATA(JJ), JJ=KIN,KEND)
  490 FORMAT (F5.1,3I5/ (7F10.4))
      WRITE OUTPUT TAPE 3,493,(DATA(JJ), JJ = KIN,KEND)
  493 FORMAT (12F10.4/12F10.4/12F10.4)
    2 READ INPUT TAPE 2,491,J,JEND,(WTS(JK), JK = J,JEND)
  491 FORMAT (2I5/(14F5.3))
      WRITE OUTPUT TAPE 3,494,(WTS(JK), JK = J,JEND)
  494 FORMAT (24F5.3/24F5.3)
   10 READ INPUT TAPE 2,500,H1,H2,RMAX,THETM,DTHET,IPLOT,MINEXP,MAXEXP
      NANGLE = THETM/DTHET + 1.001
      IF(NANGLE-180)15,15,600
   15 DO 16 K=1,NANGLE
      A=K
      TH(K)=(A-1.)*DTHET
      TH(1) = 0.10E-07
      RAD(K)=TH(K)*   0.17453295E-01
      CO(K)=COSF(RAD(K))
      SO(K)=SINF(RAD(K)/2.)**2
   16 GO(K)=LOGF(SO(K))
   20 READ INPUT TAPE 2,510,ELAB,CMP,CMT,ZZP,MAX,LMIN
```

B.2

```
  524 IF(MAX - KMAX)21,523,21
   21 KMAX = MAX
      MMAX =MAX + 1
   22 NMAX = MAX - 1
      DO 70 K = 1,NANGLE
      CO = CO(K)
      ASL(1,K) = 1.0
      ASL(2,K) = CO(K)
      DO 60 L = 1,NMAX
      CL = L
   60 ASL(L+2,K) =          ((2.*CL+1.)*CO*ASL(L+1,K) - CL*ASL(L,K))/
     X    (CL + 1.)
      DO 70 L = 1,MMAX
      CL = L - 1
   70 ASL(L,K) = (2.*CL + 1.)*ASL(L,K)
  500 FORMAT (5F10.4,3I5)
  510 FORMAT (4F10.6,2I10)
  523 VR = X(1)
      VI = X(2)
      AO = X(3)
  525 BO = X(4)
      RO = X(5)
      R1 = X(6)
      RW = X(7)
      ALPHA = X(8)
      BETA = X(9)
      KONT = X(10)
  529 RE=  RO*CMT**0.33333333
      R=  RE + R1
      RWS= RW*CMT**0.33333333      + R1
  530 CALL OPTIC(R,ELAB,CMP,CMT,ZZP,R ,AO,BO, RE,VR,VI,ALPHA,MAX,RMAX,
     X   H1,H2,PHIR,PHII,RINTP,CR,CI,SIG,CK,ETA,RWS,BETA,LMIN)
C     LOOP ON ANGLE
  100 DO  300  K=1,NANGLE
      Y=ETA*GO(K)
      Z= ETA/2./SO(K)
      SUM1 = -Z * COSF(Y)
      SUM2 =  Z * SINF(Y)
      RUTH(K) =   (Z / CK)**2
C     LOOP ON L WAVE
      DO  200   M=1,MMAX
      Y=ASL(M,K)
      Z     =   2.*(SIG(M)-SIG(1))
      SI= SINF(Z)
      CS= COSF(Z)
      SUM1 = SUM1 + ( CS *CR(M) - SI *CI(M) ) * Y
  200 SUM2 = SUM2 + ( CS *CI(M) + SI *CR(M) ) * Y
      CRSX(K) = (SUM1 **2 + SUM2 **2 )/CK**2
  300 RELA(K) = CRSX(K)/RUTH(K)
      IF (MODE)305,305,301
  301 DO 303 K = KIN,KEND
  303 DATA(K) = DATA(K)/RUTH(K)
      WRITE OUTPUT TAPE 3,493,(DATA(JJ), JJ = KIN,KEND)
      MODE = 3
  305 WRITE OUTPUT TAPE 3,700
      WRITE OUTPUT TAPE 3,710,ELAB,CMP,CMT,ZZP,VR,VI,ALPHA,BETA,RO,R1,
     X  RW,AO,BO,ETA,CK
      WRITE OUTPUT TAPE 3,720
```

```
      400 MM=(NANGLE+2)/3                                                    B.3
      420 DO  430 K =1,MM
          I= MM+K
          J= I+MM
      430 WRITE OUTPUT TAPE 3,730,TH(K),CRSX(K),RELA(K),TH(I),CRSX(I),
         X   RELA(I),TH(J),CRSX(J),RELA(J)
          WRITE OUTPUT TAPE 3,750
          REAC=0.
          DO 440 M=1,MMAX
          L=M-1
          TAN= 2.*CR(M)/(1.-2.*CI(M))
          TRANS =4.*(CI(M)-CI(M)**2-CR(M)**2)
          C=L
          REAC=REAC+ (2.*C+1.)*TRANS
      440 WRITE OUTPUT TAPE 3,760,L,CR(M),CI(M),SIG(M),PHIR(M),PHII(M)
         2  ,TAN,TRANS
          REAC=REAC*3.14159/CK**2
          WRITE OUTPUT TAPE 3,770      ,REAC
          WRITE OUTPUT TAPE 3,740,MAX,RMAX,H1,H2   ,RINTP
      800 CHIM = 0.0
          CHIST = 0.0
      810 K = 1
      815 GO TO 820
      817 K = K + 1
      820 AA = K
      830 TH(K) = (AA -1.)*DTHET
      848 IF(TH(K) -CHECK)817,850,850
      850 DIV = (RELA(K) + RELA(K+1))*(DATA(K) + DATA(K+1))
          REL = RELA(K) - RELA(K+1)
          DAT = DATA(K) - DATA(K+1)
          CHI(K) = ((RELA(K) + RELA(K+1) - (DATA(K) + DATA(K+1)))/
         X   WTS(K))**2/DIV/25.
          IF (DAT/REL)860,870,870
      860 CHIS(K) = ((REL-DAT)/WTS(K))**2/DIV/2.
          GO TO 890
      870 CHIS(K) = (REL -DAT)/WTS(K)/SQRTF(DIV)
      890  CHIS(K) = ABSF(CHIS(K))
          IF(CHIS(K) -  50.)900,900,903
      903 CHIS(K) = 50.
      900 IF(CHI(K) -  50.)906,906,907
      907 CHI(K) = 50.
      906 CHIM = CHIM + CHI(K)
          CHIST = CHIST + CHIS(K)
      901 IF(K - KEND)817,902,902
      902 CHIT = CHIM             + CHIST
      905 WRITE OUTPUT TAPE 3,910,CHIT            ,CHIM,      CHIST
      910 FORMAT( 7H  CHIT=F12.4,  7H  CHIM=F12.4,  7H CHIST=F12.4 /1H1)
          IF( IPLOT)590,590,450
      450 DO 470 K=1,NANGLE
          Y = RELA(K)
          CYCLE=MAXEXP-MINEXP
           NPLOT=  100./CYCLE *0.4343 *LOGF(Y/10.**MINEXP)+0.5
          CALL GRAPH(NPLOT,0,0)
          Y = DATA(K)
           NPLOT=  100./CYCLE *0.4343 *LOGF(Y/10.**MINEXP)+0.5
          CALL GRAPH (NPLOT,44,-1)
      470 WRITE OUTPUT TAPE 3,780,TH(K)
      700 FORMAT(      39H1   ELASTIC SCATTERING CROSS SECTION I ///)
```

B.4

```
  710 FORMAT(       9H    ELAB=F10.6,    8H    CM*=F10.6,     8H    CMT=
     XF10.6,        8H    ZZP=F10.6//    7H    VR=F10.6,      7H    VI=
     XF10.6,       10H    ALPHA=F5.3,    8H    BETA=F3.1// 7H    RO=F10.6,
     X  7H    RI=F10.6,        7H    RW=F6.3,
     X  7H    AO=F10.6,        7H    BO=F10.6//
     X  8H    ETA=F10.6,       6H    K=F10.5///)
  720 FORMAT(    113H          THETA        CRSX        CRSX/RUTH          THETA
     X    CRSX        CRSX/RUTH          THETA        CRSX        CRSX/RUTH///)
  730 FORMAT( 3(0PF12.1,1P2E13.4))
  740 FORMAT(9H0    LMAX=I3, 9H    RMAX=F10.4, 7H    H1=F10.4, 7H    H2=
     X  F10.4,  10H    RINTP=F10.4///)
  750 FORMAT(    110H0          L          CR          CI          SIG
     X          PHIR          PHII          TAN          T(L)///)
  760 FORMAT(I10,7E15.5)
  770 FORMAT(    28H0   REACTION CROSS SECTION =1PE15.5)
  780 FORMAT(1H+F8.4)
  590 GO TO (10,20,591),KONT
  591 RETURN
  600 CALL EXIT
      END
```

REFERENCES

1. M. G. Mayer, Phys. Rev. 75, 1969 (1949).
2. O. Haxel, J. H. D. Jensen, and H. E. Suess, Phys. Rev. 75, 1766 (1949).
3. H. Bethe, Phys. Rev. 47, 747 (1934).
4. E. Amaldi, O. D'Agostino, E. Fermi, B. Pontecorvo, F. Rosetti, and E. Segrè, Proc. Roy. Soc. (London) A149, 522 (1935).
5. N. Bohr, Nature 137, 344 (1936).
6. M. G. Mayer, Phys. Rev. 74, 235 (1948).
7. R. Serber, Phys. Rev. 72, 1114 (1947).
8. H. Feshback and V. F. Weisskopf, Phys. Rev. 76, 1550 (1949).
9. H. Barschall, Phys. Rev. 86, 431 (1952).
10. H. Feshbach, C. E. Porter, and V. F. Weisskopf, Phys. Rev. 96, 232 (1954).
11. B. L. Cohen and R. Neidigh, Phys. Rev. 93, 232 (1954)
12. R. W. Woods and D. S. Saxon, Phys. Rev. 95, 577 (1954).
13. D. A. Bromley and N. S. Wall, Phys. Rev. 99, 1029 (1955).
14. W. F. Waldorf and N. S. Wall, Phys. Rev. 107, 1602 (1957).
15. G. W. Greenlees, L. G. Kuo, and M. Petravic, Proc. Roy. Soc. 243, 206 (1957).
16. R. W. Peelle, Phys. Rev. 105, 1311 (1957).
17. A. E. Glassgold, W. B. Cheston, M. L. Stein, S. B. Schuldt, and G. W. Erickson, Phys. Rev. 106, 1207 (1957).
18. M. A. Melkanoff, J. S. Nodvik, D. S. Saxon, and R. W. Woods, Phys. Rev. 106, 793 (1957).
19. C. L. Oxley, W. F. Cartwright, and J. Rouvina, Phys. Rev. 93, 806 (1954).
20. L. Rosen, J. E. Brolley, Jr., and L. Stewart, Phys. Rev. 121, 1423 (1961).
21. E. Heiberg, Phys. Rev. 106, 1271 (1957).
22. F. G. J. Perry and B. Buck, Nucl. Phys. 23, 353 (1962).

23. A. A. Ross, H. Mark, and R. D. Lawson, Phys. Rev. 102, 1613 (1956).

24. F. Bjorklund and S. Fernbach, Phys. Rev. 109, 1295 (1958).

25. F. Bjorklund, Lawrence Radiation Laboratory Report UCRL-5028 (1958).

26. K. Kikucki, Nucl. Phys. 12, 305 (1959).

27. L. C. Gomes, Phys. Rev. 116, 1226 (1959).

28. K. Brueckner and J. L. Gammel, Phys. Rev. 109, 1023 (1958).

29. C. Bloch, Proceedings of the International Conference on the Nuclear Optical Model, Florida State University Studied No. 32 1959, p.178.

30. K. A. Brueckner in Proceedings of the International Conference on Nuclear Structure, Kingston 1960, p.67.

31. M. A. Melkanoff, T. Sawada, and N. Cindro, Phys. Let. 2, 98 (1962).

32. G. Igo, Phys. Rev. 115, 1665 (1959).

33. P. E. Hodgson, Nucl. Phys. 21, 28 (1960).

34. G. E. Porter, Phys. Rev. 112, 1722 (1958).

35. D. H. Stork, in Proceedings of the International Conference on the Nuclear Optical Model, Florida State University Studies No. 32 1959, p.216.

36. R. H. Lemmer and A. E. S. Green, Phys. Rev. 119, 1043 (1960).

37. W. R. Smith and E. V. Ivash, Phys. Rev. 128, 1175 (1962).

38. M. H. MacGregor, W. P. Ball, and R. Booth, Phys. Rev. 108, 726 (1957).

39. T. W. Bonner and J. C. Slattery, Phys. Rev. 113, 1088 (1958).

40. T. J. Gooding, Nucl. Phys. 12, 241 (1959).

41. V. Meyer, R. M. Eisberg and R. F. Carlson, Phys. Rev. 117, 1334 (1960).

42. G. W. Greenlees and O. N. Jarvis in Proceedings of the International Conference on Nuclear Structure, Kingston, 1960, p.217.

43. R. F. Carlson, R. M. Eisberg, R. H. Stokes, and T. H. Shirt in Annual Progress Report, University of Minnesota, 1961.

44. C. Williamson and J. P. Boujot, Tables of Range and Rate-of-Energy Loss of Charged Particles, Centre d'Etudes Nucleaires de Saclay (1962).
45. Y. Nagahara, J. Phys. Soc. Japan, 16, 133 (1961).
46. W. A. Wenzel, Lawrence Radiation Laboratory Report UCRL-8000 (1957).
47. A. E. Bjerke, Q. A. Kerns, and T. A. Nunamaker, Lawrence Radiation Laboratory Report UCRL-9838 (1961).
48. S. C. Baker, H. G. Jackson, and D. A. Mack, IRE Trans. Nucl. Sci. 7, 89 (1960).
49. G. B. Chaplin and A. J. Cole, Nulc. Instr. Methods, 7, 45 (1960).
50. N. M. Hintz, Phys. Rev. 106, 1201 (1957).
51. K. Kikuchi, S. Kobayashi, and K. Matsuda, J. Phys. Soc. Japan, 14, 121 (1959).
52. E. Schwarcz, (Lawrence Radiation Laboratory), private communication.
53. N. M. Hintz, (University of Minnesota), private communication.
54. R. G. Summers-Gill, Phys. Rev. 109, 1591 (1958).
55. E. W. Hamburger, B. L. Cohen, and R. E. Price, Phys. Rev. 121, 1143 (1961).
56. F. A. Aschenbrenner, Phys. Rev. 98, 657 (1955).
57. R. A. Peck and J. Lowe, Phys. Rev. 114, 847 (1959).
58. J. L. Yntema, Phys. Rev. 113, 261 (1959).
59. J. L. Yntema and B. Zeidman, Phys. Rev. 114, 815 (1959).
60. E. W. Hamburger, Phys. Rev. 123, 619 (1961).
61. I. Dostrovsky, Z. Fraenkel, and G. Friedlander, Phys. Rev. 116, 683 (1959).
62. V. F. Weisskopf, Phys. Rev. 52, 295 (1937).
63. A. G. W. Cameron, Can. J. Phys. 36, 1040 (1958).
64. A. G. W. Cameron, A Revised Semiempirical Atomic-Mass Formula, CRP-690 (1957).
65. N. T. Porile, Phys. Rev. 115, 939 (1959).
66. R. Beurtey, R. Catillon, R Chauminades, M. Crut, H. Faraggi, A. Papineau, J. Saudinos, and J. Thirion, Compt. Rend. 252, 1756 (1961)

67. J. Van Heerden and D. J. Prowse, Nucl. Phys. 15, 356 (1960).
68. J. L. Yntema, B. Zeidman, and B. J. Ray, Phys. Rev. 117, 801 (1960).
69. D. K. McDaniels, J. S. Blair, S. W. Chen, and G. W. Farwell, Nucl. Phys. 17, 614 (1960).
70. A. I. Yavin and G. W. Farwell, Nucl. Phys. 12, 1 (1959).
71. G. Igo, H. E. Wegner, and R. M. Eisberg, Phys. Rev. 101, 1508 (1956).
72. H. E. Wegner, R. M. Eisberg, and G. Igo, Phys. Rev. 99, 825 (1955).
73. M. A. Melkanoff, D. S. Saxon, J. S. Nodvik, and D. G. Cantor, "A FORTRAN Program for Elastic-Scattering Analyses with the Nuclear Optical Model", University of California Press (1961).
74. H. E. Conzett, Phys. Rev. 105, 1324 (1957).
75. J. S. Nodvik, C. B. Duke, and M. A. Melkanoff, Phys. Rev. 125, 975 (1962).
76. V. Meyer and N. M. Hintz, Phys. Rev. Letters 5, 207 (1960).
77. R. D. Albert and L. F. Hansen, Phys. Rev. 123, 1749 (1961).
78. J. Wing and J. R. Huizenga, "(p,n) Cross Sections of V^{51}, Cr^{52}, Cu^{63}, Cu^{65}, Ag^{107}, Ag^{109}, Cd^{111}, Cd^{114}, and La^{139} from 5 to 10.5 MeV," submitted to Phys. Rev.
79. J. Benveniste, R. Booth, and A. Mitchell, Phys. Rev. 123, 1818 (1961).
80. P. E. Hodgson, in Proceedings of the Rutherford Jubilee International Conference (Heywood Ltd., London, 1961), p. 357.
81. J. R. Huizenga and G. Igo, Nucl. Phys. 29, 462 (1962).
82. B. R. Foreman, Jr., W. M. Gibson, R. A. Glass, and G. T. Seaborg, Phys. Rev. 116, 382 (1959).
83. F. J. Vaughn, Lawrence Radiation Laboratory Report 3174 (1955).
84. G. Igo, Phys. Rev. 115, 1665 (1959).
85. I. McCarthy in Proceedings of the International Conference on the Nuclear Optical Model, Florida State University Studies No. 32, 1959, p. 24.
86. J. O. Rasmussen, Rev. Mod. Phys. 30, 424 (1958).
87. C. J Mullin and E. Guth, Phys. Rev. 82, 141 (1951).
88. R. G. Glauber, Phys. Rev. 99, 1515 (1955).

89. A. Budzanowski and K. Grotowski, Phys. Letters 2, 280 (1962).

90. E. C. Halbert, R. H. Bassel, and G. R. Satchler, Bull. Am. Phys. Soc. Series II, Vol. 7, No. 4 (1962).

91. E. C. Halbert, (Oak Ridge National Laboratory), private communication.

92. J. S. Nodvik and D. S. Saxon, Phys. Rev. 117, 1539 (1960).